Ecole Polytechnique Fédérale de Lausanne
Laboratoire de Physique des Hautes Energies

# Contribution to the Development of the LHCb acquisition electronics and Study of polarized radiative $\Lambda_b$ Decays

Thèse de Doctorat

présentée à la Section de Physique de la Faculté des Sciences de Base
(Ecole Polytechnique Fédérale de Lausanne)
pour l'obtention du grade de docteur ès sciences

par

**Federica Legger**

Physicienne diplômée de l'Université de Turin

Jury

Prof. Georges Meylan, président du jury
Prof. Aurelio Bay, directeur de thèse
Prof. Thomas Schietinger, directeur de thèse
Dr. Jonathan Lister, expert interne
Dr. Frederic Teubert, expert externe
Dr. Niko Neufeld, expert externe

Lausanne, EPFL 2006

CERN-THESIS-2006-044
08/09/2006

# Abstract

LHCb is one of the four main experiments that will take place at the future Large Hadron Collider at CERN. The data taking is foreseen to start in 2007. The LHCb detector is a forward single-arm spectrometer dedicated to precision measurements of CP violation and rare decays in the $b$-quark sector. The goal is to over-constrain the Standard Model (SM) and — hopefully — to exhibit inconsistencies which will be a signal of new physics beyond.

Building such a large experiment as LHCb is a big challenge, and many contributions are needed. The Lausanne institute is responsible for the development of a common "off-detector" readout board (TELL1), which provides the interface to the copper and optical links used for the detector readout, and outputs them to the data acquisition system, after performing intensive processing. It performs: event synchronization, pedestal calculation and subtraction, common mode subtraction and monitoring, zero suppression. The TELL1 board will be used by the majority of the LHCb subdetectors. We present here a contribution to the R&D necessary for the realization of the final board. In particular the feasibility of a mixed architecture using DSP and FPGA technologies has been studied. We show that the performance of this architecture satisfies LHCb electronics requirements at the time of the study (2002).

Within the rich LHCb physics program, $b \to s\gamma$ transitions represent an interesting sector to look for evidence of physics beyond the SM. Even if the measured decay rate is in good agreement with the SM prediction up to now, new physics may still be hidden in more subtle observables. One of the most promising is the polarization of the emitted photon, which is predicted to be mainly left-handed in the SM. However right-handed components are present in a variety of new physics models. The photon polarization can be tested at LHCb by exploiting decays of polarized $b$ baryons. If the initial baryon is polarized, asymmetries appear in the final states angular distributions, which can be used to probe the chirality of the effective Hamiltonian, and possibly to unveil new sources of CP violation. We present a phenomenological approach to the study of radiative decays of the type $\Lambda_b \to \Lambda(X)\gamma$, where $\Lambda(X)$ can be any $\Lambda$ baryon of mass $X$. Calculations of the angular distributions are carried out employing the helicity formalism, for decays which involve $\Lambda$ baryons of spin 1/2 and 3/2. Finally, detailed simulation studies of these channels in the LHCb environment allow us to assess the LHCb sensitivity to the photon polarization in $b \to s$ transitions.

**Keywords**: high energy physics, accelerator, CERN, LHC, Standard Model, $b$-physics, data acquisition.

# Résumé

L'expérience LHCb sera installée auprès du futur accélérateur LHC (Large Hadron Collider) du CERN et commencera en 2007. Il s'agit d'un spectromètre à un bras consacré aux mesures de précision de la violation CP et de désintégrations rares impliquant le quark $b$. Cela permettra de tester avec précision le Modèle Standard et, peut-être, de mettre en évidence des incohérences qui seraient une trace d'une physique au-delà de ce modèle.

Réaliser une grande expérience telle que LHCb est un grand défi, et beaucoup de contributions sont nécessaires. Le Laboratoire de Physique des Hautes Energies de Lausanne est responsable du développement d'une carte d'acquisition des données hors-détecteur (TELL1), qui fournit l'interface aux signaux optiques et électriques utilisés pour la lecture du détecteur, et les transmet au système d'acquisition de données, après avoir effectué des calculs intensifs. Ceci inclut : synchronisation, filtrage des signaux, calcul et soustraction des piédestaux, soustraction et contrôle du bruit commun, suppression des zéros. La carte TELL1 sera employée par la majorité des sous-détecteurs de LHCb. Nous présentons ici une contribution au R&D nécessaire pour la réalisation du projet final. En particulier la faisabilité d'une architecture qui utilise à la fois des technologies DSP et FPGA a été étudiée. Nous prouvons que les performances de cette architecture répond aux exigences pour l'électronique de LHCb au moment de l'étude (2002).

Dans le riche programme de physique de LHCb, les transitions $b \to s\gamma$ représentent un secteur intéressant pour rechercher des signes de physique au-delà du Modèle Standard. Même si le taux de désintégrations mesuré est en bon accord avec les prévisions théoriques jusqu'ici, de la nouvelle physique peut encore se cacher dans des observables plus subtiles. Une des plus prometteuses est la polarisation du photon émis, que le Modèle Standard prédit être principalement gauche. Des composantes droites sont présentes dans plusieurs nouveaux modèles théoriques. La polarisation du photon peut être measurée à LHCb par l'exploitation des désintégrations des baryons polarisés contenant un quark $b$. Si le baryon initial est polarisé, des asymétries apparaissent dans les distributions angulaires des états finaux, qui peuvent être employées pour sonder la chiralité de l'Hamiltonien effectif, et dévoiler des nouvelles sources de violation de CP. Nous présentons une approche phénoménologique à l'étude de désintégrations radiatives du type $\Lambda_b \to \Lambda(X)\gamma$, où $\Lambda(X)$ peut être n'importe quel baryon $\Lambda$ de masse $X$. Des calculs des distributions angulaires sont effectués en utilisant le formalisme d'hélicité, pour des désintégrations de baryons $\Lambda$ avec spin 1/2 et 3/2. Enfin, des simulations détaillées de ces canaux dans le cadre de l'expérience LHCb nous permettent d'évaluer la sensibilité de LHCb à la polarisation du photon émis dans les transitions $b \to s$.

**Mots-clés**: physique des hautes énergies, accelerateur, CERN, LHC, Modèle Standard, physique du quark $b$, acquisition des données.

# Acknowledgments

I would like to express my gratitude to Prof. Aurelio Bay and Prof. Thomas Schietinger for guiding me through the perilous path that led to the completion of this thesis. Their help has always been valuable and stimulating. I would also like to thank Prof. Olivier Schneider for his always precious comments.

I reserve special thanks to Guido Haefeli, who introduced me to the mysteries of digital signal processing with infinite patience, and to Prof. Maurice Gailloud, who is always willing to help the students who happen to pass by his office with great enthusiasm.

I would like to thank Laurent Locatelli, who has the ability of cheering up the atmosphere in our office with always interesting football discussions. Special thanks also to the members of the BSP football team: Luis Fernandez, Martin Rey, Jean-Baptiste Mosset, Frederic Arod, Japhet Bagilishya, Dario Zurcher, Luc Hinz, Paolo Angelino, and all the others I have forgot to mention. Thanks to Christian Jacoby and Sergio-Jimenez Otero, for always participating to the CERN running race. From the Lausanne electronics group, I would like to especially thank Raymond Frey and Guy Masson. Thanks to all other colleagues for the happy atmosphere at the BSP, and especially to our wonderful secretaries, Erika, Monique and Esther.

Among many of the LHCb colleagues, I would like to thank, in random order, Hans Dijkstra, Thomas Ruf, Paula Collins, Jorgen Christiansen, Ulrik Egede, Eric van Herwijnen, Andrey Golutvin, Patrick Robbe, Patrick Koppenburg, Vanya Belyaev. A special thanks goes to our spoke-person Tatsuya Nakada.

Last but not least I would like to thank the jury of the thesis Prof. Georges Meylan, Jo Lister, Frederic Teubert and Niko Neufeld.

Thanks to all these people for their professional experience and pleasant moments that we shared.

Finally I would like to express my love and gratitude to my husband, Andrea, and all my family and friends for their everlasting support.

# Contents

**Abstract** i

**Résumé** iii

**Acknowledgements** v

**I Overview** 1

**1 Introduction** 3
1.1 The Standard Model and beyond . . . 3
1.2 Symmetries . . . 5
1.2.1 CP violation and the creation of our universe . . . 6
1.2.2 Parity violation in $b \to s$ radiative decays. . . . 7

**2 Theoretical Overview** 9
2.1 The Standard Model . . . 9
2.1.1 Introduction . . . 9
2.1.2 Construction of the Standard Model . . . 10
2.2 Flavor physics . . . 11
2.2.1 Introduction . . . 11
2.2.2 The CKM matrix . . . 11
2.2.2.a The quark mixing parameters . . . 12
2.3 CP violation . . . 12
2.3.1 CP violation in the quark sector . . . 13
2.4 Operator Product Expansion . . . 13
2.5 Rare radiative $b$-hadron decays . . . 15

**3 The LHCb experiment** 17
3.1 The LHC . . . 17
3.1.1 LHC challenges . . . 18
3.1.2 Cross sections at the LHC . . . 19
3.2 The LHCb spectrometer . . . 20
3.2.1 The VErtex LOcator (VELO) . . . 22
3.2.2 The RICH . . . 23
3.2.3 The magnet . . . 23
3.2.4 The trackers . . . 24

3.2.5 The calorimeters . . . 25
3.2.6 The muon detector . . . 25
3.3 LHCb data acquisition and trigger . . . 26
3.3.1 Trigger overview . . . 28
3.3.2 The old strategy . . . 28
3.3.2.a L0 trigger . . . 28
3.3.2.b L1 trigger . . . 29
3.3.2.c High Level trigger . . . 29
3.3.3 Data acquisition overview . . . 31
3.3.4 The 1 MHz readout . . . 32
3.4 The LHCb software . . . 33

**II Contribution to the L1 electronics 35**

**4 R&D for the TELL1 board: choice of the L1 buffer technology 37**
4.1 Introduction . . . 37
4.2 The readout board RB3 . . . 38
4.2.1 The VELO readout . . . 38
4.2.2 RB3 technologies . . . 39
4.3 The L1T and HLT preprocessing . . . 40
4.3.1 L1T and HLT zero suppression . . . 41
4.3.2 The Linear Common Mode Suppression algorithm . . . 42
4.4 A DSP-FPGA shared memory implementation for the L1 Buffer . . . 46
4.4.1 Memory types overview . . . 47
4.4.2 The L1 Buffer . . . 48
4.4.3 Bus arbitration . . . 49
4.4.4 The clusterization . . . 50
4.5 RB3 and DAQ_DSP tests . . . 51
4.5.1 Test results . . . 52
4.5.2 DSP Software development . . . 53
4.5.3 L1 electronics requirements . . . 53
4.5.4 Other tests: Integration with the PVSS system . . . 54
4.6 Conclusions . . . 55
Appendix to Chapter 4 . . . 57
4.A RB3 architecture . . . 57
4.A.1 RB3 dataflow . . . 58
4.B The DAQ_DSP mezzanine board . . . 59
4.B.1 TMS320C6211 Architecture . . . 59
4.C HLT Dataflow . . . 61
4.C.1 The L1 Buffer . . . 61
4.C.2 The handshake protocol . . . 62
4.C.3 Interface with the FSC FPGA . . . 62
4.C.4 Data transfer from the L1 buffer . . . 63
4.C.5 HLT zero suppression . . . 63
4.C.6 Cluster encapsulation . . . 63
4.C.7 Interface to the DAQ_Link FPGA . . . 64
4.C.8 HLT interface . . . 64

**III Search for polarized radiative $\Lambda_b$ decays at LHCb** **67**

**5 Phenomenology of polarized radiative $\Lambda_b$ decays** **69**
5.1 Introduction . . . 69
5.2 Theoretical framework . . . 70
5.2.1 CP violating effects . . . 71
5.2.2 Branching ratios . . . 72
5.3 The photon polarization . . . 73
5.4 Angular observables for $\Lambda_b \to \Lambda(X)\gamma$ . . . 73
5.4.1 Helicity formalism for $\Lambda_b \to \Lambda(X)\gamma$ decays . . . 73
5.4.2 $\Lambda(X)$ spin = 1/2 . . . 75
5.4.3 $\Lambda(X)$ spin = 3/2 . . . 76
5.5 Measuring the photon polarization in $\Lambda_b \to \Lambda(X)\gamma$ decays. . . . 78
Appendix to Chapter 5 . . . 80
5.A Angular distributions for the decay $\Lambda_b \to \Lambda(X)\gamma$ . . . 80
5.A.1 The case $J_\Lambda = \frac{1}{2}$ . . . 80
5.A.2 The case $J_\Lambda = \frac{3}{2}$ . . . 82

**6 The decays $\Lambda_b \to \Lambda(X)\gamma$ at LHCb** **87**
6.1 Introduction . . . 87
6.2 Event generation . . . 88
6.3 Event simulation and reconstruction . . . 90
6.3.1 Charged track reconstruction . . . 90
6.3.2 Photon reconstruction . . . 91
6.4 Detector and reconstruction performances . . . 92
6.4.1 Data samples . . . 93
6.5 Selection of radiative $\Lambda_b$ decays . . . 94
6.5.1 Charged particle identification . . . 94
6.5.2 Charged tracks selection . . . 95
6.5.3 The $\Lambda$ reconstruction . . . 96
6.5.4 Photon selection . . . 97
6.5.5 The $\Lambda_b$ reconstruction . . . 97
6.5.6 Mass resolutions . . . 100
6.5.7 Selection algorithm performances . . . 102
6.5.8 Inclusive $b\bar{b}$ background . . . 104
6.6 BR measurement . . . 105
6.7 Conclusions . . . 106
Appendix to Chapter 6 . . . 108
6.A Distributions . . . 108

**7 Sensitivity to the photon polarization measurement in $\Lambda_b \to \Lambda(X)\gamma$ decays at LHCb** **119**
7.1 Introduction . . . 119
7.2 $\Lambda_b$ production at the LHC . . . 120
7.3 Error sources in the photon polarization measurement . . . 121
7.3.1 Statistical errors . . . 121
7.3.2 Detector resolution . . . 122
7.4 LHCb sensitivity to the measurement of $|r|$ . . . 124
7.4.1 Dependence on the $\Lambda_b$ polarization . . . 127

7.5 Conclusions . . . . . 127

**Conclusion** **129**

**Bibliography** **131**

`Let my twentyfive readers think...`

[A. MANZONI, *"The Betrothed"*]

# Part I

# Overview

# Chapter 1

# Introduction



*This chapter is, as the title says, introductory to the context and subject of this thesis. It is probably the only one that is accessible to non-physicists. I tried to keep it as clear of obscure formulas and symbols as possible.*

What I find most charming in studying particle physics is that it aims to answer to the basics questions that have fascinated mankind from the beginnings: what is the world made of? What holds it together? It is somehow amazing that extraordinary events, such as the Big Bang and the following formation of our universe, can be studied measuring the properties of tiny and short-lived particles. This is what particle physics is all about: studying particles that live for a millionth of a second, trying to extract from their properties the recipe used to build our universe. There exist many good books on the subject, written by much better authors than myself, so here I shall give a short introduction to the basic concepts needed to understand the aim and reasons for this thesis.

## 1.1 The Standard Model and beyond

The best description of known elementary particles and their fundamental interactions at the moment is a theory called the Standard Model (SM). The SM states that the fundamental building blocks of matter consist of six quarks ($u$, $d$, $c$, $s$, $t$, $b$) and three leptons with their associated neutrinos ($e$, $\mu$, $\tau$, $\nu_e$, $\nu_\mu$, $\nu_\tau$). The most common particles, protons and neutrons, which we all know since they make up the nucleus of atoms, are not fundamental, but are in fact composed by three quarks ($uud$ for the proton and $udd$ for the neutron)[1]. Indeed, nobody has ever seen a free quark, they are all bound to one another to make up other particles. Moreover, for each particle there exists a corresponding an-

[1] Particles composed of three quarks, as protons and neutrons, are called *baryons*, while particles composed of a quark and an anti-quark are called *mesons*.




tiparticle, a particle that is in every way similar to the first one, but with opposite charge. The existence of antimatter was first predicted by P. A. M. Dirac, back in 1928.

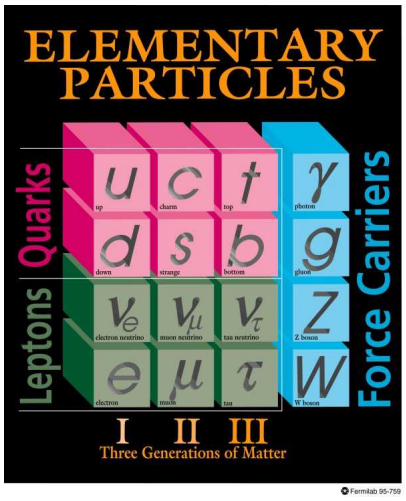



Figure 1.1: *All known particles predicted by the Standard Model. Picture from [1].*

These particles interact through the exchange of other particles, which are 'mediators' of the interactions. Up to now, four interactions are known: the gravitational and electromagnetic interactions, whose effects we see in everyday life; the nuclear force, which holds together the protons and neutrons in nuclei; and the weak force, which is held responsible for radioactivity, or for most of nuclear reactions in stars. The SM describes very well the electromagnetic, strong and weak interactions, but fails to include gravity in the framework. It predicts the following force carriers (the mediators): the photon $\gamma$ for the electromagnetic force, the bosons $Z^0$, $W^\pm$ for the weak one, and 8 gluons $g$ for the strong (see figure 1.1 and table 1.1 for details and some properties of these particles). However, these particles are all predicted to be massless, while we know that for example the weak bosons $Z^0$, $W^\pm$ are massive. There exists a mechanism to explain these masses, but it needs another mysterious particle, the Higgs boson $H^0$, which has not been found yet and is on the top of physicists wish lists for the Christmasses to come.

Even if the Higgs boson is found, a number of theoretical reasons exists to believe that the SM is far from being the final theory to describe nature. First of all, gravity is not included. At present there is no theory that can accommodate gravity in a framework that is compatible with quantum mechanics. Moreover, the SM as it is now has plenty of unknown parameters (19!) such as quark masses[2], couplings, ... that have to be fixed by the experiment.

Physicists believe that the SM is a low-energy approximation of a somehow bigger

[2]Considering massless neutrinos for simplicity. Massive neutrinos account for 10 additional parameters.

Table 1.1: *Summary of elementary particles. Particles in* ***bold*** *are stable. Particles in a grey box are the constituents of the atom (Courtesy of P. Koppenburg [2]).*

| | Charge | Particles | | | |
|---|---|---|---|---|---|
| Matter | $+\frac{2}{3}$ | $\mathbf{u}$ | c | t | Quarks |
| | $-\frac{1}{3}$ | d | s | b | |
| | $-1$ | $\mathbf{e^-}$ | $\mu^-$ | $\tau^-$ | Leptons |
| | $0$ | $\boldsymbol{\nu_e}$ | $\boldsymbol{\nu_\mu}$ | $\boldsymbol{\nu_\tau}$ | |
| Mediators | $0$ | gluons | | | strong force |
| | $0$ | $\boldsymbol{\gamma}$ | | | electromagnetism |
| | $+1, 0, -1$ | $W^+$ | $Z^0$ | $W^-$ | weak force |
| | $0$ | Graviton? | | | gravity |
| Anti-matter | $0$ | $\overline{\boldsymbol{\nu}}_\mathbf{e}$ | $\overline{\boldsymbol{\nu}}_{\boldsymbol{\mu}}$ | $\overline{\boldsymbol{\nu}}_{\boldsymbol{\tau}}$ | Anti-leptons |
| | $+1$ | $\mathbf{e^+}$ | $\mu^+$ | $\tau^+$ | |
| | $+\frac{1}{3}$ | $\bar{d}$ | $\bar{s}$ | $\bar{b}$ | Anti-quarks |
| | $-\frac{2}{3}$ | $\bar{\mathbf{u}}$ | $\bar{c}$ | $\bar{t}$ | |

framework, maybe one of the *Grand Unified Theory* (GUT) that has been proposed through the years to unify gravity with the other three forces. Every attempt (even by Einstein) has failed up to now. There exist, however, several extensions to the SM. The most popular is called *supersymmetry*. It predicts the existence of many new particles (heavier "supersymmetric" partners of ordinary particles), none of which has been found yet.

What is widely believed to be a final test for the SM is the start-up at CERN of a new accelerator, the Large Hadron Collider (LHC), which is foreseen for 2007. Its declared aim is to find the Higgs boson, and possibly give important indications on the goodness of the new theoretical models such as supersymmetry.

The LHC will host four experiments: ATLAS and CMS, specifically designed to find the Higgs boson; LHCb (the experiment in whose context this thesis has been developed), that will study CP violation in $b$-meson decays (see section 1.2.1); and ALICE which will look for the quark-gluon plasma in heavy ion collisions.

## 1.2 Symmetries

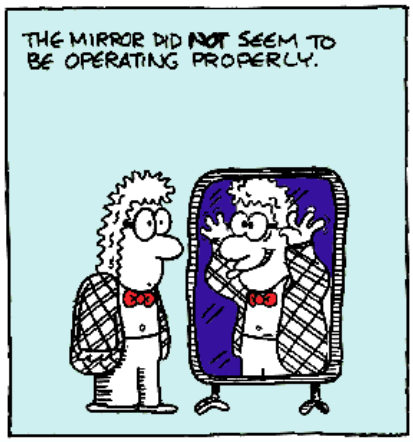
Since symmetric problems are easier to solve, physicists like to look for any possible symmetry[3]. The SM was developed by looking at what symmetries are conserved or violated by the various interactions. In a similar way, symmetries may also contain the key to "new physics" beyond the SM. Supersymmetric models, for example, extend the SM framework by adding more symmetries to the picture.

In particle physics there are three fundamental discrete symmetries: Parity (P), Charge conjugation (C) and Time reversal (T). Parity corresponds to space reflections, i.e. mirror-

[3]When we say that a system is symmetric with respect to a certain transformation, we mean that, if we apply that particular transformation to the system, the transformed system obeys the same laws as the original one. For example, a symmetry in translation gives us freedom in choosing the origin of a reference system. Wherever in space we set the origin, the system will always follow the same physics laws.

like, charge conjugation corresponds to the exchange of particles and antiparticles, while time reversal corresponds to the inversion of time. It is generally believed that these symmetries are respected as a whole (CPT), i.e. if all three of them are applied one after the other. However the application of one or two symmetries may transform the system in such a way that it behaves differently from the original one.

P violation was the first to be discovered, back in the late Fifties, by Madame Wu. This discovery was a shock for the physics community, since in the macroscopic world nobody can tell if the object he is looking at is a real image or a reflection (see section 1.2.2 for further explanations). However this is not true at the microscopic level. Moreover a symmetry can be violated by some interactions and respected by others. For instance parity is conserved in strong but not in weak interactions. This is of course puzzling, and up to now there is no hint of a possible explanation. Part of this thesis work will indeed be focused on testing P violation in the SM.




Also the CP symmetry is found to be violated. However, while parity is always violated in weak interactions, CP violation has only been observed in the weak decays of mesons containing a $b$ or an $s$ quark (respectively called $B$ and $K$ mesons). This fact can be accommodated by the SM, but the exact amount of CP violation still needs to be precisely verified (and explained). Moreover CP violation has deep implications on our understanding of the creation of our universe (see next paragraph).

The violation of one or more symmetries opens up many questions: can some of the answers lead us to find a more complete theory than the SM?

### 1.2.1 CP violation and the creation of our universe

CP violation in the electro-weak sector is a nice example of how particle properties (mainly interest of a small fraction of physicists) can be related to general fundamental questions which may affect everybody.

The most accredited theory to explain the birth of our universe is the so-called Big Bang model, which states that the universe started as pure energy, which later 'condensated' into matter and antimatter. However, our universe is obviously made of matter only: where has the antimatter gone? It has been demonstrated [3] that three conditions are necessary for the Big Bang model to work: non-conservation of baryonic number, departure from thermal equilibrium, and CP violation. All this is somehow taken into account into the SM, but its effects are too small to explain the large matter-antimatter asymmetry we observe nowadays. Therefore a better understanding of CP violation can help us to shed light on what happened in the very first moments of our universe lifetime.

The aim of LHCb, one of the future experiments at the LHC at CERN, is indeed to measure CP violation in the decay of particles containing a $b$ quark. In order to build a challenging experiment such as LHCb, many years of R&D are necessary. Part of this thesis work has been devoted to contribute to the LHCb design and construction. This will be described in part II.

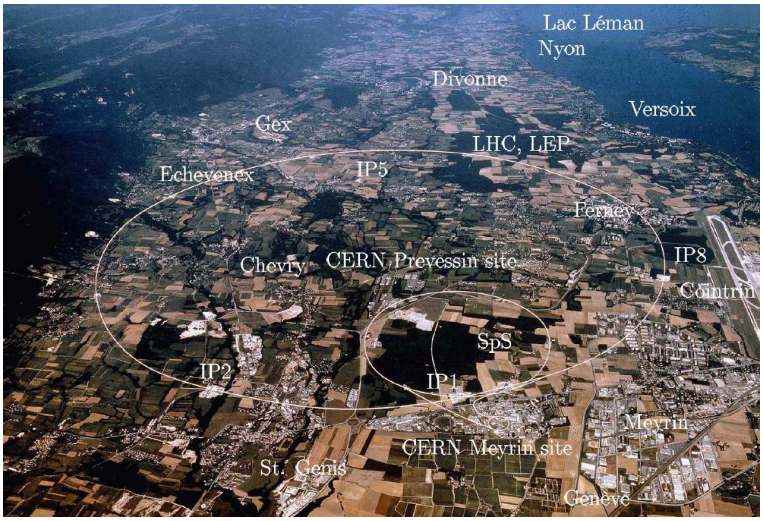
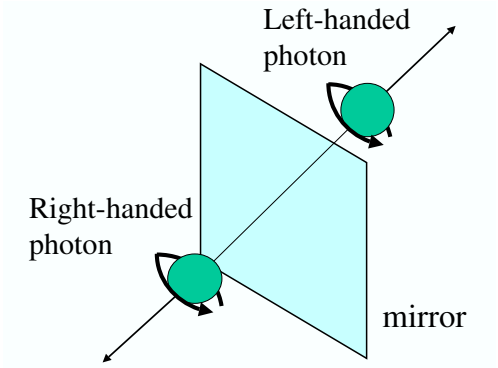



Figure 1.2: *The CERN site near Geneva. LHCb is being installed at IP8. Picture from the CERN document server [4].*

### 1.2.2 Parity violation in $b \to s$ radiative decays.

Not all the particles we know are stable. They decay until only stable particles are left. This explains why we do not usually find them in nature. Obviously, all common particles (the proton, the neutron[4], the electron, the photon) are stable. Among the quarks, only the $u$ and $d$ quarks are stable (and indeed, they are the ingredients of protons and neutrons, which then make up the nucleus).

For instance, the $b$ quark is unstable. It may decay into a lighter quark, for example the $s$ quark, and some other particle. The $s$ quark is not stable, and will decay in its turn into a $u$ quark, and end the chain. Let us focus on the first decay $b \to s$. This transition is allowed in the SM (and a photon is emitted in the decay), but it is quite unlikely to happen. This is a first hint to where a physicist can look for physics beyond the SM. One can measure the probability of such a decay, and compare its finding with the SM prediction. Unfortunately, the measured and theoretical $b \to s\gamma$ rates agree very well.




Still, the SM makes an additional prediction: due to parity violation, the photon is emitted in a 'privileged' direction. This may need further explanation. All elementary particles have an intrinsic property which is called *spin*. Naively the spin can be thought of as an intrinsic rotation of the particle around its own center-of-mass. We call right-handed all particles which rotate clockwise with respect to their direction of motion, whereas left-handed particles rotate counter-clockwise. If we look at a right-handed particle in a mirror, the rotation does not change but its direction of motion is reversed: the mirror turns it into a left-handed particle!

If parity is conserved, we would find an equal amount of right-handed and left-handed

[4]This is true only when it is bound in an atom.

particles. However this is not the case for photons emitted in $b \to s$ transitions. The SM states that these photons are mainly left-handed, however the exact value of the asymmetry has not been measured yet. The aim of part III of this thesis is to study the feasibility of such a measurement at LHCb, and analyze the best possible methods to accomplish it. If a discrepancy between the SM prediction and the measured value is found, it would be an indirect proof that the SM is not complete, and that there are other particles to discover.

# Chapter 2

# Theoretical Overview




*This chapter contains the theoretical framework necessary to understand LHCb motivations and physics goals. It spans from the Standard Model to the search for new physics beyond it, passing through flavor physics and CP violation.*

## 2.1 The Standard Model

### 2.1.1 Introduction

The Standard Model (SM)[1] aims to describe the various interactions among fundamental particles. It was initially developed for leptonic interactions by Glashow, Weinberg and Salam [6, 7, 8]. The SM has been derived in the context of Quantum Field Theory (QFT), whose main ingredients are[2]:

- The fields of the elementary particles one wants to describe;
- A gauge group with its generators (one vector field for each generator, and $N + 1$ scalar fields, if one wants to have $N$ massive vector fields.)
- The most general Lagrangian which is invariant under the gauge group, and describes all the couplings among the above fields.

As already mentioned in chapter 1, the SM works well with the weak, electromagnetic and strong interactions, but fails to include gravitation.

[1] Developing the SM is beyond the scope of this thesis. There exist many good books on the subject, one for all could be [5]. Here only a few reminders, necessary to understand the following, are given. Of course, this dissertation is neither complete nor exhaustive.

[2] See for example [9] for a good introduction to the field of QFT.

### 2.1.2 Construction of the Standard Model

#### Fermionic fields

The SM aims to describe the interactions of known fundamental fermions, i.e. the leptons $\ell$ and the quarks $q$. They are normally grouped by generations[3]:

$$\ell = \begin{pmatrix} \nu_e \\ e \end{pmatrix}, \quad \begin{pmatrix} \nu_\mu \\ \mu \end{pmatrix}, \quad \begin{pmatrix} \nu_\tau \\ \tau \end{pmatrix}$$

$$q = \begin{pmatrix} u \\ d \end{pmatrix}, \quad \begin{pmatrix} c \\ s \end{pmatrix}, \quad \begin{pmatrix} t \\ b \end{pmatrix}$$

Quarks and leptons are easily distinguished since the latter ones do not interact strongly. The weak interaction not being invariant under parity transformations (P), it is useful to define the left-handed and right-handed states of the fermions[4]. They are obtained applying respectively the two operators $L = \frac{1}{2}(1 - \gamma_5)$ and $R = \frac{1}{2}(1 + \gamma_5)$, and are noted with the subscripts $_L$ and $_R$.

The phenomenology indicates a difference between the boson couplings to leptons and quarks. The coupling of the scalar field to the leptons and the quarks is in fact different, since leptons and quarks masses are different (for example, all 6 quarks are massive). Moreover the flavor of the quarks can be changed by weak interactions (while being conserved by strong and electromagnetic ones) involving charged gauge bosons. This is described in more details in section 2.2.

#### Gauge group and its generators

The phenomenology of the physical interactions suggests the form of the gauge group $G$, which is given by:

$$G = SU(3) \otimes SU(2)_L \otimes U(1)$$

where:

- $SU(3)$ is the gauge group of the strong interaction. It has 8 generators: the gluons. The interaction between quarks and gluons is described by the Quantum Chromo Dynamics (QCD) theory.
- The group $SU(2)_L \otimes U(1)$ describes the weak and electromagnetic interactions. The Higgs mechanism [10] is used to spontaneously break the $SU(2)_L \otimes U(1)$ symmetry into the $U(1)$ electromagnetic symmetry, and to give mass to the gauge bosons $W^\pm$ and $Z^0$.

#### The Lagrangian

The SM Lagrangian can be split up in components which account for the various interactions:

$$\mathcal{L} = \underbrace{\mathcal{L}_{\mathrm{BB}} + \mathcal{L}_{\mathrm{FB}}}_{\mathcal{L}_{\mathrm{GWS}}} + \underbrace{\mathcal{L}_{\mathrm{SB}} + \mathcal{L}_{\mathrm{SF}}}_{\mathcal{L}_{\mathrm{Higgs}}} + \mathcal{L}_{\mathrm{QCD}}$$

[3] Why there exists only three generations of fermions is one of the unanswered questions of the SM.
[4] There are no right-handed neutrinos in the SM.

where:

- $\mathcal{L}_{\rm GWS}$ describes the electroweak part of the Lagrangian. The term $\mathcal{L}_{\rm BB}$ describes the self-coupling of the generators of the gauge group $SU(2)_L \otimes U(1)$. The term $\mathcal{L}_{\rm FB}$ accounts for the coupling of the fermions to the gauge bosons, and it contains a right-handed and a left-handed part.
- $\mathcal{L}_{\rm Higgs}$ contains the (Yukawa) coupling of the Higgs boson to the $SU(2)_L \otimes U(1)$ gauge bosons ($\mathcal{L}_{\rm SB}$) and to the fermions ($\mathcal{L}_{\rm SF}$).
- $\mathcal{L}_{\rm QCD}$ describes the couplings of gluons and quarks. The gluons being massless, they do not couple to the Higgs scalar field.

## 2.2 Flavor physics

### 2.2.1 Introduction

To fix the gauge boson ($W^{\pm}$,$Z^0$, the photon, and the gluons) masses, the so-called interaction basis is used. In this basis, gauge interactions are diagonal, and no gauge coupling within fermions of different generation exists. However, the scalar Higgs boson interactions are quite complicated, and involve fermions of different generations. Therefore the interaction eigenstates (the fermions) do not have well-defined masses in this basis. In the mass basis, Yukawa interactions are diagonal, and fermion masses can be determined. Nevertheless in this basis quarks of different generations are mixed by the gauge interactions. Flavor physics refers to the interactions that distinguish between the fermion families[5].

### 2.2.2 The CKM matrix

The matrix that describes the change of basis from the interaction to the mass basis is the weak mixing matrix $V_{\rm CKM}$[6]. It is usually defined to mix the down-type quarks:

$$\begin{pmatrix} \mathrm{d}' \\ \mathrm{s}' \\ \mathrm{b}' \end{pmatrix} = \underbrace{\begin{pmatrix} V_{\rm ud} & V_{\rm us} & V_{\rm ub} \\ V_{\rm cd} & V_{\rm cs} & V_{\rm cb} \\ V_{\rm td} & V_{\rm ts} & V_{\rm tb} \end{pmatrix}}_{V_{\rm CKM}} \begin{pmatrix} \mathrm{d} \\ \mathrm{s} \\ \mathrm{b} \end{pmatrix}$$

A general unitary $N \times N$ matrix has $N^2$ parameters. $N(N-1)/2$ of those can be taken as Euler angles. The remaining parameters are complex phases. However we know from quantum mechanics that phases cannot always be measured (what matters here is not the absolute phases but the relative phases of different fields). It can be shown that for the above matrix $2N-1$ phases are not measurable [14]. Therefore we are left with 3 angles and a complex phase, which completely define the $V_{\rm CKM}$ matrix.

The $V_{\rm CKM}$ matrix allows flavor changing charged currents. Flavor Changing Neutral Currents (FCNC) are still forbidden in the SM at tree level, but are present in many SM extensions. They are however allowed in the SM at higher orders, using the so-called GIM[7] mechanism [15].

[5] This discussion is inspired by [11].
[6] From its authors Nicola Cabibbo [12], Makoto Kobayashi and Toshihide Maskawa [13].
[7] From its authors Glashow, Iliopoulos and Maiani.

If neutrinos were massive, as the last experimental results seem to indicate [16], a similar mechanism would exist for the leptonic part of the SM, and charged currents would allow mixing of leptons of different generations.

#### 2.2.2.a The quark mixing parameters

While the fermion masses are determined from kinematics of various processes so that the values are model independent, the mixing parameters can only be determined from weak interaction processes and could be affected by new physics [11]. Intensive efforts are therefore being made to measure the $V_{\rm CKM}$ elements.

There exists three places where one can look for new physics in the mixing sector:

i) Direct measurement: tree level SM processes. Contribution from new physics is however expected to be very small.

ii) Unitarity of the $V_{\rm CKM}$ matrix: it holds true if only three generations of quarks exist, and would be violated in case of a fourth generation.

iii) Indirect measurement: SM loop processes which are suppressed in the SM, but not necessarily in some SM extensions.

Particularly suited to the measurements of $V_{\rm CKM}$ elements are the neutral meson systems $K$-$\overline{K}$ and $B$-$\overline{B}$ (see section 2.3.1).

## 2.3 CP violation

In weak interactions Parity (P) and Charge conjugation (C) are violated in a maximal way. However their product (CP) still seems to be a good symmetry in almost all the cases. "Almost" is quite a disturbing word for physicists, which aim to find a theory that works successfully in all possible cases. Moreover understanding the violation of this symmetry is a fundamental step to confirm cosmological models (see also chapter 1). Thus, CP violation has to be explained in some way in the SM.

Within the theory, CP violation may occur in the following sectors:

- in the quark sector, via the phase of the $V_{\rm CKM}$ matrix. See section 2.3.1;
- in the lepton sector via the phases of the neutrino mixing phase if, as it seems more and more likely, neutrinos do have a non-zero mass. These have not been explored by experiments up to now[8];
- in the strong interactions. However in this sector no CP violation has been found, which is still unexplained.

While the SM gives a satisfactory parametrization of the violation of CP, it fails in providing an explanation. CP violation is therefore quite an interesting sector for physicists to look for new physics, and giving a better understanding is one of the goals of the LHCb experiment.

[8] See for instance [17] for a recent dissertation on the status and future of experimental neutrino physics.

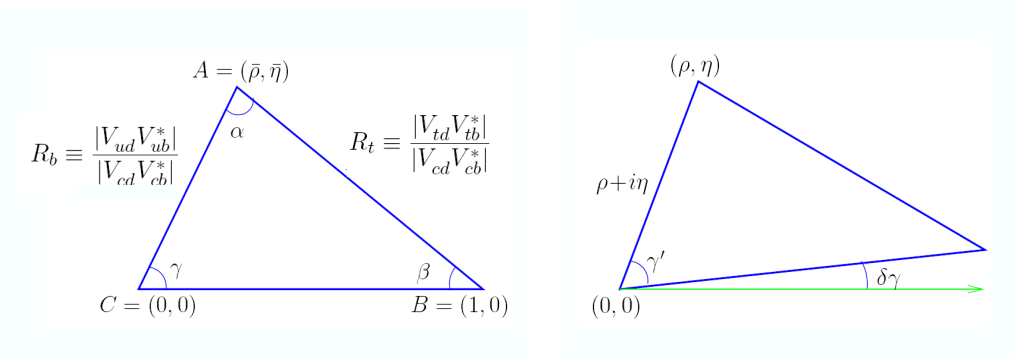



Figure 2.1: *The unitarity triangles corresponding to the relations 2.1 (left) and 2.2 (right).*

### 2.3.1 CP violation in the quark sector

The $V_{\rm CKM}$ unitarity conditions can be visualized by triangles in the complex plane[9]. It can be shown that measuring CP violation can be related to measuring the angles and sizes of these triangles. The most promising relations are:

$$V_{\rm ud}V_{\rm ub}^* + V_{\rm cd}V_{\rm cb}^* + V_{\rm td}V_{\rm tb}^* = 0, \quad (2.1)$$

$$V_{\rm ud}^*V_{\rm td} + V_{\rm us}^*V_{\rm ts} + V_{\rm ub}^*V_{\rm tb} = 0 \quad (2.2)$$

which correspond to the triangles in fig. 2.1. The others triangles are squashed due to the hierarchy in quark masses, and are related to light quarks.

Relations (2.1) and (2.2) are related to the third generation of quarks, therefore a good place to look for CP violation is in the $b$ sector. The branching ratios for decays involving $b$ transitions are small, but CP violation is sizable. There is currently a worldwide effort to measure the many manifestations of CP violation expected in decays of $B$ mesons. Making these measurements requires the production of large numbers of such mesons, and the accelerator facilities designed to generate them have come to be known as "$B$ factories." Two experiments (BaBar and Belle) are currently taking data at the existing $B$ factories, respectively at the SLAC [19] (United States) and KEK [20] (Japan) accelerators. LHCb aims to make precision measurements of CP violation exploiting $b$ decays that will be available in large numbers at the next hadron collider, the LHC (see chapter 3).

## 2.4 Operator Product Expansion

While leptons are only ruled by the electro-weak interactions, hadrons are also subject to the strong force, therefore their study always involves the interplay between the electro-weak theory and QCD.

It can be shown that the amplitude for a process involving hadrons can be written as [21]:

$$A(M \to F) = \langle F|\mathcal{H}_{\rm eff}|M\rangle = \sum_i C_i(\mu)\langle F|O_i(\mu)|M\rangle \quad (2.3)$$

[9] See for example [18] for a parametrization of the $V_{\rm CKM}$ matrix and a precise definition of the complex plane ($\rho$, $\eta$) that is generally used to draw the unitarity triangles, as well as a comprehensive review on CP violation in the quark sector.

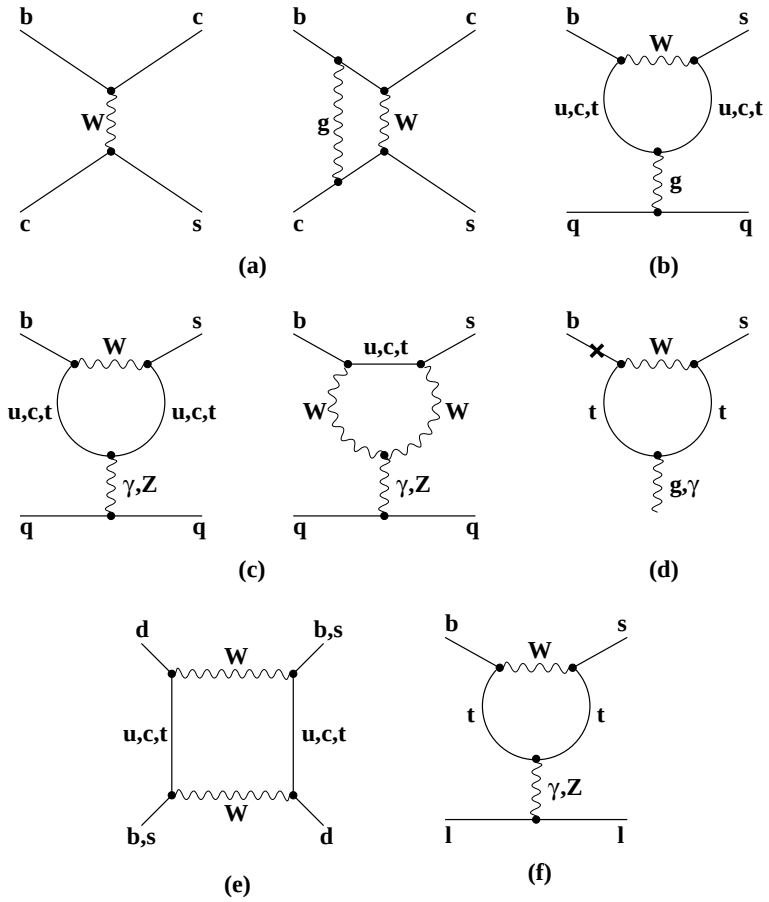



Figure 2.2: *Typical lowest order Feynman diagrams corresponding to the OPE operators. (a) current-current operators $Q_1$ and $Q_2$, (b) QCD penguin operators $Q_3$, $Q_4$, $Q_5$, $Q_6$, (c) electroweak penguin operators $Q_7$, $Q_8$, $Q_9$, $Q_{10}$, (d) magnetic penguin operators $Q_{7\gamma}$ and $Q_{8\mathrm{G}}$, (e) $\Delta S, B = 2$ operators, (f) semileptonic operators $Q_{9\mathrm{V}}$ and $Q_{10\mathrm{A}}$. Figure from [23].*

where the effective Hamiltonian $\mathcal{H}_{\mathrm{eff}}$ is factorized into a sum of matrix elements of local operators $O_i$. Each operator is multiplied by the corresponding Wilson coefficient $C_i$ which expresses the strength with which it enters the Hamiltonian. The Wilson coefficients take into account all fields with a mass larger than the renormalization scale $\mu$, which is chosen to be $\mathcal{O}(1\,\mathrm{GeV})$. This useful tool is called Operator Product Expansion (OPE), and was first introduced by Wilson and Zimmermann [22].

One of the advantage of the OPE is that it allows a separation of different contributions to the effective Hamiltonian. Short distance effects, which involve all interactions that can be solved in a perturbative way, are described by the Wilson coefficients, while long distance contributions, for which no perturbative calculation is possible, are taken into account by the local operators. In this way one can use the Fermi theory, which states that at scales $\mu \ll m_{\mathrm{W}}$ the interactions mediated by a heavy boson correspond to a point-like interaction, to calculate the Wilson coefficients. Calculations exist for all $C_i$ at Next-to-Leading Order (NLO). Many techniques have been developed to solve the non-perturbative part of the problem, which lies in the local operators, as for instance the Heavy Quark Effective Theory (HQET) [24].

Equation (2.3) can be rewritten to show explicitly the relevant $V_{\mathrm{CKM}}$ matrix elements:

$$A(M \to F) = \frac{G_F}{\sqrt{2}} V_{lj} V_{lk}^* \sum_i C_i(\mu) \langle F|Q_i(\mu)|M\rangle \tag{2.4}$$

where $\frac{G_F}{\sqrt{2}} = \frac{g^2}{8m_{\rm W}}$ is the Fermi coupling constant, the indices $j$ and $k$ refer to the external quark lines, and $l$ refers to the internal quark line. The Wilson coefficients are calculated in expansions of the strong coupling constant $\alpha_s$ [25].

In the case of $b$-quark decays, which is the sector of interest for LHCb, the renormalization scale $\mu$ is normally chosen as the mass of the $b$ quark itself. Some of the operators that regulate $\Delta B = 1$ transitions are shown in picture 2.2. More details can be found in [18, 25, 26, 27]:

## 2.5 Rare radiative $b$-hadron decays

As we have shown in the previous paragraphs, one of the most promising places to look for new physics in the $b$ sector is given by rare decays mediated via FCNC. This sector has drawn much attention lately due to the growth of statistics for events of this type at the $B$ factories (Belle and BaBar), but the full potential of these decays will be exploited at the LHC, where even more $b$-hadrons will become available.

These processes are associated to the FCNC currents in $b \to s$ transition, which are forbidden at the tree level in the SM, and are strongly suppressed by the GIM mechanism, but may occur via penguin diagrams. However, as of today, the measured $b \to s\gamma$ Branching Fraction (BF) [28, 29] is in good agreement with the SM prediction [30]:

- Theory prediction: BF($b \to s\gamma$) = $(357 \pm 30)\cdot 10^{-6}$ [31]
- Experimental result: BF($b \to s\gamma$) = $(355 \pm 24\ ^{+9}_{-10} \pm 3)\cdot 10^{-6}$ [32]
  Average from various measurement by BaBar, Belle and Cleo.

On the other hand, these decays may be very sensitive to new physics effects in the operators and Wilson coefficients that appear in the low energy effective Hamiltonian. The photon emitted in $b \to s$ transitions is predicted to be mainly left-handed in the SM, because of the chiral structure of the W boson coupling in the loop[10]. However a variety of new physics models (left-right symmetric models, super-symmetric models with large left-right squark flavor mixing, and models containing new vector-like quarks) predicts the presence of right-handed components.

Several methods have been proposed to probe the photon polarization in $B$ meson radiative decays:

- $B$-$\overline{B}$ interference: CP asymmetries from the interference of mixing and decay in radiative $B$ neutral decays require that both $B$ and $\overline{B}$ decay to a common state, i.e. with the same photon helicity. Therefore if the photon is polarized, as predicted in the SM, the CP asymmetry from the mixing should vanish [34]. The world average for the CP asymmetry (measured from a time dependent analysis of $B \to K_S\pi^0\gamma$ decays) is $0.00 \pm 0.28$ [32]. The result is consistent with 0, but errors are still large.

[10]This argument holds as long as $b \to s\gamma$ is a two-body decay, however it cannot be applied to multi-body final states such as $b \to s\gamma$ + gluons. Once QCD corrections are properly included, right-handed contributions may arise already within the SM [33]. See chapter 5 for more details.

- $e^+e^-$ conversion: conversion electron pairs can be effectively used to probe the photon polarization by measuring the angular correlations between the recoiling $K^*$ and the $e^+e^-$ in $B \to K^*\gamma$ decays, where the photon can be either real (and converts into a $e^+e^-$ pair in the beam pipe) [35] or virtual [36].

- interference of several higher $K^*$ resonances decaying to $K\pi\pi$ gives access to the photon polarization [37]. However from the experimental point of view disentangling the resonance structure is not trivial (see the latest BaBar measurement [38]).

- interference between $B$ decays to the same final state but through different resonances (for instance $B \to K^*(K\gamma)\gamma$, $B \to \eta_c(\gamma\gamma)K$, and $B \to \chi_{c0}(\gamma\gamma)K$ [39].

None of these methods has brought clarifying results up to now, due to the limited statistics at the currently running $B$ factories.

However the photon polarization can also be probed in polarized $b$-baryons decays, which will be produced in large quantities at the LHC. We will therefore focus on the study of radiative decays of $\Lambda_b$ baryons of the type $\Lambda_b \to \Lambda(X)\gamma$, where $X$ is the mass of the $\Lambda$ baryon, with particular attention to their sensitivity to New Physics, and the measurement of LHCb performances for these decays. It will be shown that, if the initial $\Lambda_b$ is polarized, as it is foreseen at the LHC, the polarization of the emitted photon can be probed by measuring the angular correlations between the initial and the final states. This study will be the subject of part III of this thesis.

# Chapter 3

# The LHCb experiment



*In this chapter a general description of the LHCb experiment is given. First the LHC accelerator is presented, then the LHCb spectrometer is described with particular attention to the trigger system, in whose context a great part of this thesis work has been developed.*

## 3.1 The LHC

CERN (Conseil Européen pour la Recherche Nucléaire) was founded in 1954 as one of the first joint ventures in Europe [40]. It provides scientists the tools (basically particle accelerators) to study the smallest building blocks of matter. It was founded by 12 countries, and it now counts 20 member states. Ever since, it has continuously upgraded its accelerators in order to answer to the ultimate particle physics challenges.

The LHC will represent the next (and last, for the moment) generation of circular colliders [41]. It will be placed in the LEP (Large Electron Positron collider) tunnel, but it will collide protons or heavy ions, instead of electrons and positrons. The tunnel is 27 km long and spans across Swiss and French territory, buried several meters underground. The collisions will happen at a center-of-mass energy of $\sqrt{s} = 14$ TeV. The technology change from electrons to protons is necessary to reach such high energies without too many losses due to synchrotron radiation. The drawback of proton collisions is the high hadronic background.

Another requirement LHC has to satisfy is that of high luminosity, in order to have the chance to study rare decays or to find the Higgs boson, whose production cross-section is still of a few tens of fb at LHC energy. Since antiprotons are hard to produce and store, proton-proton collisions have been chosen, even if a proton-antiproton collider is much easier to design. The design luminosity[1] of LHC is $\mathcal{L} = 10^{34}\text{cm}^{-2}\text{s}^{-1}$, and it will be reached after 1 to 4 years of operation.

[1]The luminosity is a quantity that measures the collisions rate (given by the product of the luminosity and

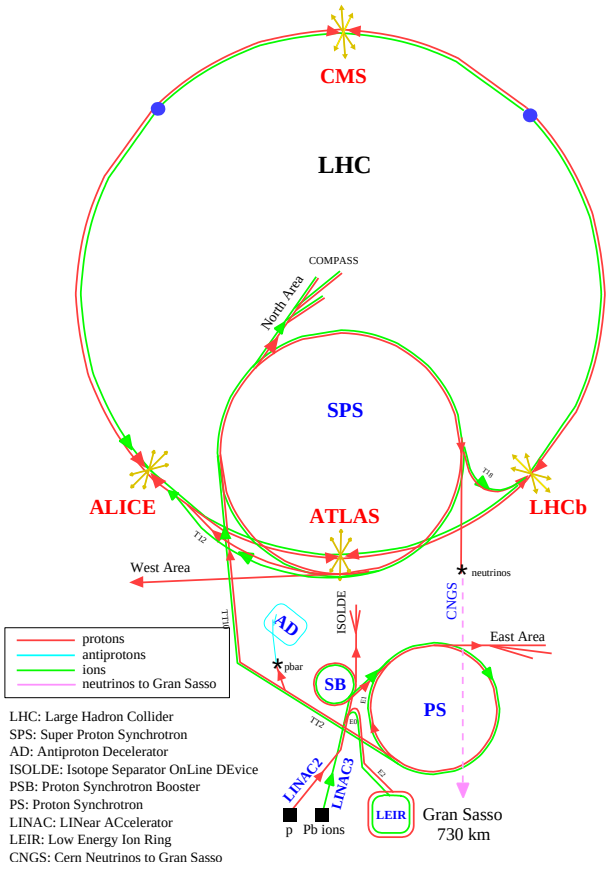



Figure 3.1: *The CERN accelerator complex. Picture from [4].*

The accelerator chain is shown in figure 3.1. Protons of 50 MeV coming from the LINAC will be accelerated up to 1 GeV by the Proton Synchrotron Booster (PSB). They pass then into the Proton Synchrotron (PS) where they reach an energy of 26 GeV before entering the Super Proton Synchrotron (SPS), where they are accelerated to 450 GeV. From there the protons are directly injected into the LHC rings, where they attain an energy of 7 TeV. Proton-proton collisions will take place at a rate of 40 MHz in four interaction points, where LHC experiments are located. Only ATLAS and CMS requires LHC design luminosity, in their quest for the Higgs. LHCb will use only a fraction of LHC luminosity, while ALICE will study ion collisions (Pb-Pb).

LEP machinery has been reused for the LHC quite as a whole (including the tunnels and injection scheme), the only modification being the necessity for two distinct rings in which the two opposite proton beams circulate. In fact, since the two beams are made of the same kind of particles (or at least of the same charge), they obviously cannot share the same ring. The two beams only meet each other at the four interaction points, where the experiments' detectors are installed.

### 3.1.1 LHC challenges

The energy reached by a single beam in LHC, 7 TeV, is about 7 times higher than that of the Fermilab Tevatron. Moreover, it will reach a luminosity ($10^{34}\text{cm}^{-2}\text{s}^{-1}$) that will be 100 times higher than that of the Tevatron ($1.6{\cdot}10^{32}\text{cm}^{-2}\text{s}^{-1}$ [42]). The KEKB accelerator currently holds the record luminosity ever attained in a collider ($1.6{\cdot}10^{34}\text{cm}^{-2}\text{s}^{-1}$ [43]). Nevertheless, this machine works at quite low energy (10 GeV) with respect to the LHC.

---

the cross section for a given process). For a collider the luminosity is given by:

$$\mathcal{L} = \frac{N_1 N_2 k_b f \gamma F}{4\pi\beta^* \epsilon}$$

where $N_i \approx 10^{11}$ are the number of protons per bunch, $k_b$ the number of bunch crossings at the considered interaction point, $f = 11.25$ kHz the revolution frequency and $\gamma = E_\text{p}/m_\text{p}$. The emittance $\epsilon = 3.75\ \mu\text{m rad}$ measures the compactness of the beam and the betatron function $\beta^* = 0.5$ m measures the ability of the magnets to focus the beam at the interaction point. Finally $F$ is a factor which takes into account the crossing angle of the two beams.

To achieve the design luminosity, the two LHC rings will be filled with about 2800 bunches of $10^{11}$ particles each. The resulting current of 0.53 A is quite a challenge for a machine made of superconducting magnets operating at cryogenics temperatures. In fact the magnetic field needed to bend the particles into a 27 km circular trajectory requires 8.3 T furnished by magnets operated at 1.9 K.

Several effects limit the maximal available luminosity. First of all the beam needs to be well focused at the interaction points (the transversal beam size will be of 17 $\mu$m at the LHC). Secondly beam-beam interaction reduces the maximum number of particles per bunch. This happens at interaction points, when only a few of the protons do interact with the protons of the other beam, the other ones being deflected by the electromagnetic field of the other beam. This eventually leads to particle losses. Moreover the various bunches interact with one another through an electromagnetic wake-field, which perturbates particles trajectories, which can finally result in beam loss. Small non-linearities in the deflection and focusing magnets can also produce beam instabilities. All these effects need to be counteracted by sophisticated feedback systems. Moreover the beams need to be kept for several hours (10 hours is the present plan), during which they make four hundred million revolutions in the accelerator.

If instabilities are not accurately taken care of, they can propagate quite easily and result in uncontrolled beam loss. This could be deadly for the detectors and all nearby apparatus, and has to be carefully avoided. Monitoring systems are being developed to respond quickly to all kind of possible dangers.

### 3.1.2 Cross sections at the LHC

Table 3.1: *Cross sections assumed throughout this document [44].*

| Cross-section | | |
|---|---|---|
| Total | $\sigma_{\rm tot}$ | 100 mb |
| Inelastic | $\sigma_{\rm inel}$ | 55 mb |
| $\rm c\bar{c}$ | $\sigma_{\rm c\bar{c}}$ | 3.5 mb |
| $\rm b\bar{b}$ | $\sigma_{\rm b\bar{b}}$ | 500 $\mu$b |

The relevant cross-sections at the LHC are listed in table 3.1. The values are extrapolated from SPS and Tevatron data. Unfortunately errors on the estimations are quite large, so that for example the expected $b\bar{b}$ cross section lays between 175 and 950 $\mu$b. In this document we assume it to be 500 $\mu$b, which is the value currently adopted as a reference by LHC collaborations. These numbers need of course reconfirmation as soon as the LHC starts taking data.

The average number of interactions per bunch crossing can be estimated starting from the inelastic cross section $\sigma_{\rm inel}$:

$$< N_{pp} >= \frac{L\sigma_{\rm inel}}{kf}$$

where $k$ is the number of bunch crossings at a given interaction point, $L$ the luminosity, and $f = 11.25$ kHz the revolution frequency. Since luminosity requirements for the various experiment are different we have:

| | $\mathcal{L}$ (cm$^{-2}$s$^{-1}$) | $k$ | $< N_{pp} >$ |
|---|---|---|---|
| **ATLAS, CMS** | $1 \cdot 10^{34}$ | 2808 | 17.4 |
| **LHCb** | $2 \cdot 10^{32}$ | 2652 | 0.37 |

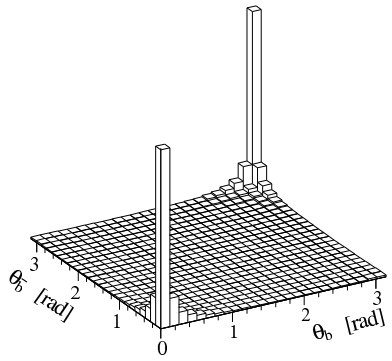



Figure 3.2: *Polar angle distribution of $b$ hadrons at LHC. Figure from the Technical Proposal [45].*

Hence, at the LHCb interaction point, there will be about one $p$-$p$ interaction out of three bunch crossings. This is to avoid having multiple interactions (called "primary" vertices) in the same event. These could be in fact misleadingly interpreted by the trigger as detached ("secondary") vertices. The choice of the luminosity is the resulting compromise between the need to keep radiation damage low and the maximization of the probability of having just one interaction per bunch crossing.

For what concerns $b\bar{b}$ production, the dominant mechanism is believed to be the fusion of two or more gluons radiated by the constituent quarks of the protons. The result of this process is a quite flat distribution in rapidity[2] and hence a very peaked angular distribution for low polar angles (see figure 3.2, where the reference system has been chosen with the coordinate $z$ in direction of the beam axis). $b$ particles are then more likely to be produced in the same forward (or backward) cone. Although LHCb is the LHC experiment designed to exploit $b$ physics features, CMS and ATLAS both have a $b$ physics program for the first years of data taking, while waiting for the LHC to achieve its design luminosity.

## 3.2 The LHCb spectrometer

Since we have just shown that $b$ decay products will fly close to the beam axis, it is clear that a detector aiming to study this kind of physics has to cover low polar angles. This is the case for LHCb, a forward single arm spectrometer as can be seen in fig. 3.3. The angular coverage ranges from 10 mrad to 300 (250) mrad in the bending (non-bending) plane. Only one of the two possible forward regions is covered by the detector. LHCb will be installed at IP8, and will use the cavern occupied by the Delphi experiment during LEP running. To avoid any civil engineering it has to fit into the old cavern, which sets a limit to its dimensions. LHCb is 20 m long and 10 m wide.

To reduce the material budget and to improve trigger performances, the detector layout has undergone some modifications from the original proposition of the Technical Design Report [45]. The changes are described in the Reoptimized Detector TDR [46].

LHCb must satisfy the following requirements to efficiently study rare $b$ decays:

- a versatile and efficient trigger scheme, in order to cope with a variety of channels with low branching fractions;
- a precise particle identification in order to study as many channels as possible;
- a high-resolution vertex detector, to define primary and detached vertices, for precise proper-time measurements. Vertexing is especially important since $b$ hadrons decays are quite displaced from the original p-p interaction point, due to the long life time and the Lorentz boost.

[2]The rapidity is the dimensionless quantity defined as $\theta = \tanh^{-1}\beta$

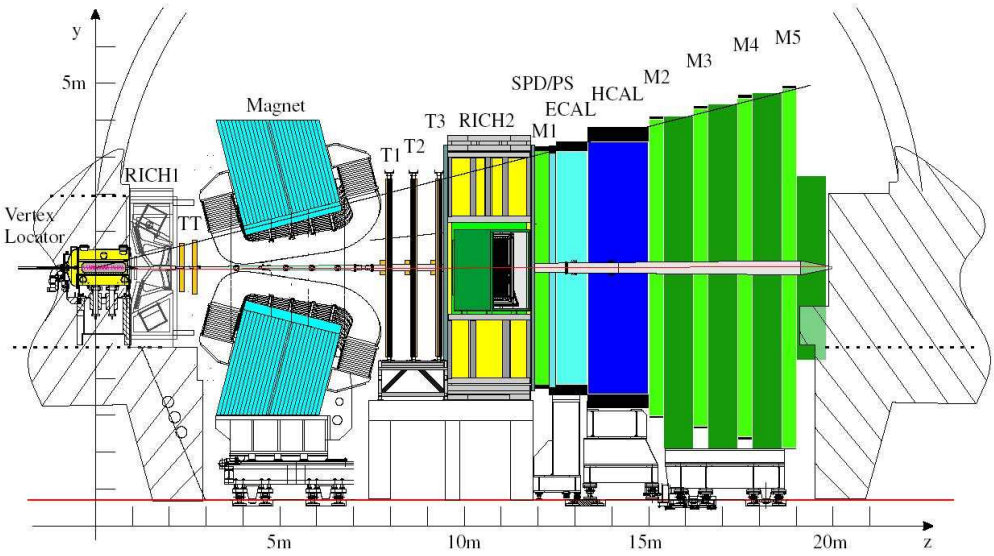



Figure 3.3: *The LHCb spectrometer. Side view of the detector (non-bending plane). Also shown is LHCb reference system, which is chosen as the following: the $z$ axis is along the beam pipe, with the origin close to the interaction point and pointed toward the detector. The $y$ axis is in the vertical direction, which also coincides with LHCb magnetic field direction. The $x$ axis is horizontal and is chosen to have a right handed coordinate system. Picture from [46].*

This is accomplished by the following detector layout (have a look at fig. 3.3 from left to right, or downstream):

- the vertex detector (VELO, VErtex LOcator);
- the upstream Ring-Imaging Cherenkov detector (RICH1);
- the Trigger Tracker (TT);
- the dipole magnet;
- the main tracking stations (T1-T3);
- the downstream Ring-Imaging Cherenkov detector (RICH2);
- the Scintillating Pad Detector (SPD) and Preshower (PS);
- the electromagnetic calorimeter (ECAL);
- the hadronic calorimeter (HCAL);
- the muon detector (M1-M5).

Track reconstruction and particle identification is performed in LHCb in the following way: first prompt tracks are reconstructed to find the primary vertex, secondly a $b$ hadron is searched for looking at secondary vertices. This will be the main task of the VELO detector. Particle momenta will be measured by combining the information of the four tracking stations (TT, T1-T3). Energy measurements for hadrons and (mainly) electromagnetically interacting particles (photons and electrons) are provided respectively by the hadronic and

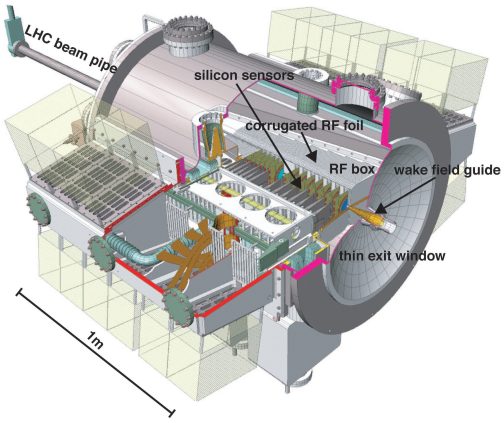



Figure 3.4: *3D view of the VELO detector (with the old 25 stations design). Picture from [46].*

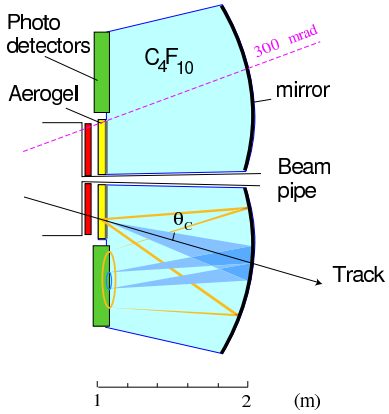



Figure 3.5: *Schematic layout of the RICH1 detector. Picture from [47].*

electromagnetic calorimeters. Muon identification is accomplished by the muon detector, while the identification among the various types of hadrons is the main task of the RICHes. A description of the various subsystems is given below. The experiment is also completed by a trigger and DAta acQuisition (DAQ) system, which is described in section 3.3.1.

### 3.2.1 The VErtex LOcator (VELO)

The VELO is a solid-state detector, which measures precisely charged particle coordinates. It is a silicon strip detector, and features 21 stations displaced along the beam direction (see picture 3.6). It is placed outside the LHCb magnetic field, to simplify the track reconstruction performed by the trigger. In order to have the minimum amount of material between the interaction point and the detector, a thin ($\sim 100$ $\mu$m) aluminium box replaces the beam pipe (see picture 3.4). The box is also used to separate the VELO vacuum from the beam pipe vacuum, and serves as RF shield. The shape has been carefully studied in order to reduce the multiple scattering, which is a source of confusion for the trigger. For precise vertexing, the sensors are placed very close to the beam pipe, and need to be retracted during LHC beam injection phase. Possible misalignments are corrected on a run-by-run basis.

The VELO has undergone major modifications during LHCb re-optimization, namely the reduction of the number of stations from 25 to 21, with insignificant reduction of physics performances [46].

Each station measures the $r$ and $\phi$ of a charged particle that flies through the detector. The sensors are half-circular silicon foils, with inner and outer radius of respectively 8 and 42 $\mu$m. They cover 182° each, allowing for overlap to cover completely the acceptance. The sensors are single-sided, and each station features two silicon planes separated 2 mm from each other (each one with two half-circular sensors), one for measuring $r$, and the other $\phi$.

The spatial resolution is on average (depending on the number of tracks) 42 $\mu$m along the beam axis, and 10 $\mu$m in the transverse direction. The VELO is the only detector that can give information about backward tracks.

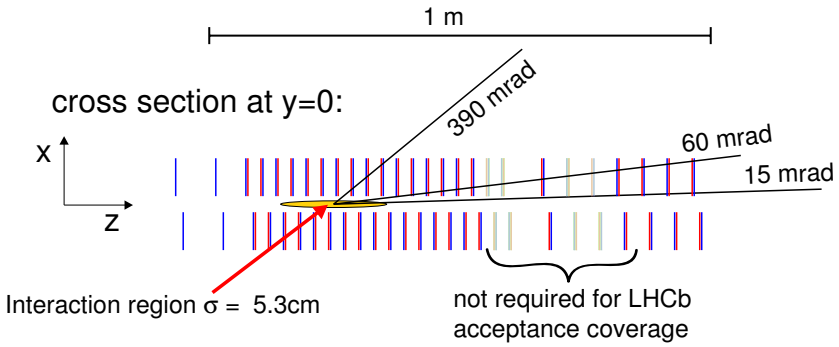



Figure 3.6: *View of VELO stations setup. Shaded stations are the ones removed in the new setup. Picture from [46].*

### 3.2.2 The RICH

The main aim of the RICH detector is hadron identification in LHCb, especially the separation of pions from kaons over the full momentum range [47]. This is accomplished by two Ring Imaging Cherenkov detectors, which employ the fact that energetic charged particles traversing a transparent medium can produce light (called Cherenkov light) with a speed larger than the speed of light in that medium. As one can see from figure 3.5, the emitted Cherenkov photons, represented as blue cones around the track, are reflected by a spherical mirror towards the detector (cylindrical pixelated Hybrid Photo Diode (HPD) tubes), where they form ring images. The RICH detector is placed outside the area of influence of the LHCb magnet, since HPDs are quite sensitive to magnetic fields. It is also segmented into two parts, to allow identification of particles with different momentum ranges. This is due to the fact that the polar angle of a track is strongly correlated with its momentum ($\theta \sim 1/P$). The upstream RICH1 is located before the magnet, and employs as radiators silica aerogel and $C_4F_{10}$. Its aim is to detect tracks with low momentum (ranging from 1 to 70 GeV) and high polar angles (from 30 to 300 mrad). The downstream RICH2 is placed after the bending magnet, and uses $CF_4$ as a radiator. It is to detect particles with high momentum (12-150 GeV) and small angles (15-120 mrad). Momenta higher than 150 GeV are unlikely to belong to $b$ tracks.

### 3.2.3 The magnet

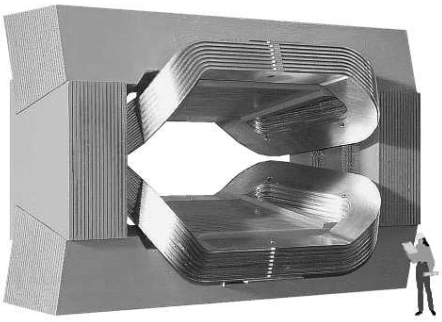


Figure 3.7: *The LHCb magnet. Picture from [48].*

The LHCb magnet is made of 9 km of aluminium conducting wires (weighing 50 tons in total) and of a 120 kt steel plate yoke [48]. It features a bending power of $\int Bdl = 4$ Tm (integrated over 10 m, 1.1 T maximal magnetic field intensity) and dissipates about 4 MW. It is located as close as possible to the interaction point in order to keep its dimensions to a minimum but, as previously said, after the VELO and RICH1. The magnetic field is oriented in the vertical direction, which makes tracks bend in the horizonal plane $xz$. It covers 300 mrad in the bending plane and 250 mrad in the vertical plane. To compensate for left-right asymmetries in the detector, the possibility to invert the magnetic field was a requirement to the magnet

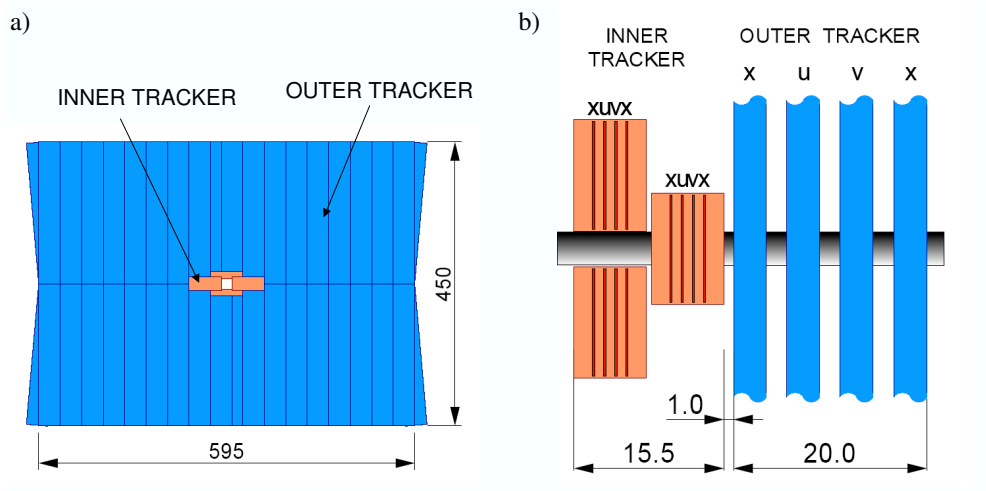



Figure 3.8: *Front (a) and top (b) view of a tracking station. Dimensions are given in cm. Lateral dimensions in b) are not to scale. Picture from [49].*

design. This (together with cost reduction) led to the choice of a classic warm magnet instead of a superconducting one.

### 3.2.4 The trackers

The tracking system allows the measurement of the momentum of charged particles. It is also used to link the VELO tracks to hits in the calorimeters and muon chambers, and as a seed for RICH information. To reduce detector material, the original design of nine stations has been abandoned, and the tracker consists now of only four stations. The first one is located downstream of the RICH1 and in front of the magnet, and it is called Trigger Tracker (TT), since its information is employed by the Level-1 trigger to measure momenta of charged tracks. It is also used to recover low momentum tracks that are otherwise bent out of the acceptance of T1-T3. The TT station consists of four plates of silicon strip detectors. While the first and the fourth layer have vertical strips ($x$-layer), the second and the third one have a stereo angle of $\pm 5^\circ$ ($u$- and $v$-layers).

The rest of the tracking system is actually split in two parts (see fig. 3.8). The inner one, in a region where high multiplicity is expected, is still a silicon strip detector, while in the outer part, where the occupancy is much lower, straw drift tubes can be used. The Inner Tracker (IT) consists in four detection layers. The overall sensitive surface of the three stations amounts to 4.2 $m^2$. The charged particle flux is expected to be $5{\cdot}10^5$ $cm^{-2}$ $s^{-1}$ in the innermost region, and rapidly decreasing with increasing distances from the beam axis. The Outer Tracker (OT) detects charged tracks with a radial angle greater than 15 mrad. The OT, as the TT and IT, is made up by four detection layers (the first and the fourth are $x$-layers, whereas the second and the third respectively $u$- and $v$-layers). The gas drift chamber technology allows for good spatial resolution at a moderate cost (compared to silicon detectors). The gas mixture (Ar - 75%, $CF_4$ - 15%, $CO_2$ - 10%) has been chosen to optimize drift times.

### 3.2.5 The calorimeters

The calorimeters are used to identify hadrons, electrons and photons, and to provide a measurement of their energy and position [50]. The most important task of the calorimeters is to provide information to the first level of trigger, in order to select interesting events according to their energy content. For this reason, the readout needs to be fast (40 MHz), and the number of channels has been chosen as a compromise between fast detector response and good precision and resolution.

Four different subsystem make up the LHCb calorimeters:

- A Scintillator Pad Detector (SPD), to reduce the background due to high energy $\pi^0$ in the electron trigger.
- A pre-shower detector (PS) that separates photons and electrons according to the topology of the electromagnetic shower produced in ECAL.
- An Electromagnetic CALorimeter (ECAL) to detect photons and electrons.
- A Hadronic CALorimeter (HCAL) to detect hadrons.

The SPD and PS consist of 15 mm thick scintillator pads, and are placed on either side of a 12 mm thick lead wall. The ECAL uses the Shashlik technology with lead as absorber material, while the HCAL is built with 16 mm thick iron and 4 mm thick scintillating tiles parallel to the beam. In all cases the scintillation light is driven through wavelength shifting (WLS) fibers to multi-anode photomultipliers.

### 3.2.6 The muon detector

Since muons are present in many final states of CP-sensitive decays, they are of particular interest to LHCb. Since their interaction probability is so low, they turn out to be the only charged particles to pass through the calorimeters (the other particle, neutral, to accomplish this is the neutrino). In order to allow any other particle but the muons to pass through, an additional shield made of four layers of steel is placed after the calorimeters.

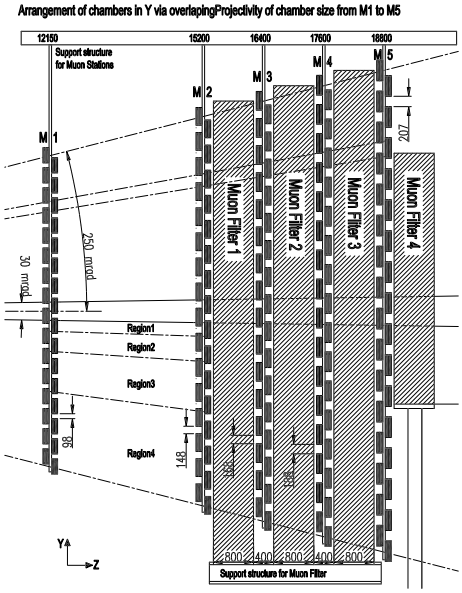



Figure 3.9: *Side view of the Muon detector. Picture from [51].*

The Muon detector is divided into five stations. The first one, M1, is used to measure the transverse momentum of the tracks that are found in the residual stations (M2-M5), and is used as an input to the first level of trigger. The five stations are made of multiple wire proportional chambers (MWPC). The acceptance is 20-306 mrad in the bending plane, and 16-258 mrad in the non-bending plane, which can be translated into a 20% geometrical acceptance of muons coming from $b$ decays.

## 3.3 LHCb data acquisition and trigger

When a high energy physics experiment is running, detector information needs to be collected and stored for later analysis. Storing all data coming out of the detectors is generally not possible since this would take up too much time and resources. For example at the LHC the bunch crossing frequency is 40 MHz, which means a new event is being produced every 25 ns, and in LHCb an event is made of thousands of signals produced by all the experiment sensors. Raw data needs first to be processed and translated into a more compact form, in order to reduce the event information to a reasonable size. They normally need to be amplified, digitized, and the level of noise they contain must be reduced as much as possible. Even after this first step, the LHCb event size corresponds to about 0.1 MBytes. Hence, to record all events, one should be able to save data at a rate of 4 TB per second, which is beyond the possibilities of current technologies.

To cope with such high rates, particle physics experiments need a trigger system, which must be capable of recognizing interesting events on-the-fly, and store just those. Since precision measurements require high statistics, it is obvious that the selection process must be as precise as possible (see picture 3.10). This delicate task is performed by the LHCb trigger and data acquisition system.

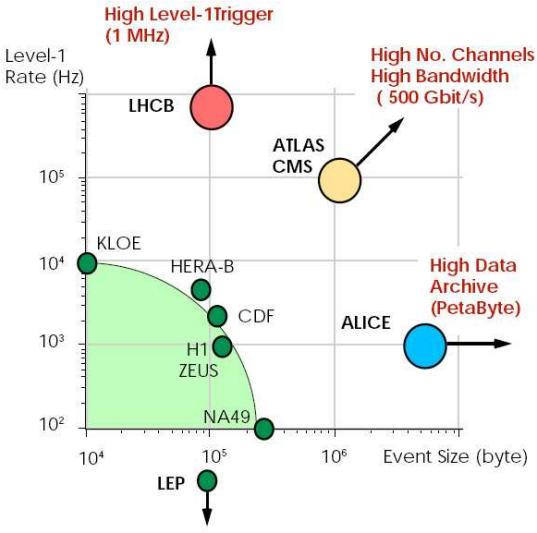



Figure 3.10: *Event size versus first level trigger rate for some high energy physics experiments. Picture from [52].*

Signals coming from different subsystems are treated differently, but in general only a preliminary amplification and processing is done close to the detector. The high radiation level in the detector proximity requires full custom electronics. All components must be tested and certified to work in a high radiation environment, and only "simple" electronic devices can actually be used in such harsh conditions. Hence data are transmitted along transmission lines (50-100 m long) of copper or optical fibers to the counting room, which is located in a radiation-safe area farther away from the pit. Here most of the processing is done, and events passing the LHCb trigger are finally stored to disk.

A difficult task that comes along with data acquisition is the synchronization and control of all subsystems among themselves, and to the LHC environment. Fast controlling and clock distribution is accomplished by the Timing, Trigger and Control (TTC) system which is common to all LHC experiments [53], while slow controlling, together with initialization, calibration, debugging and error checking is performed by the LHCb Experiment Control System (ECS) [54].

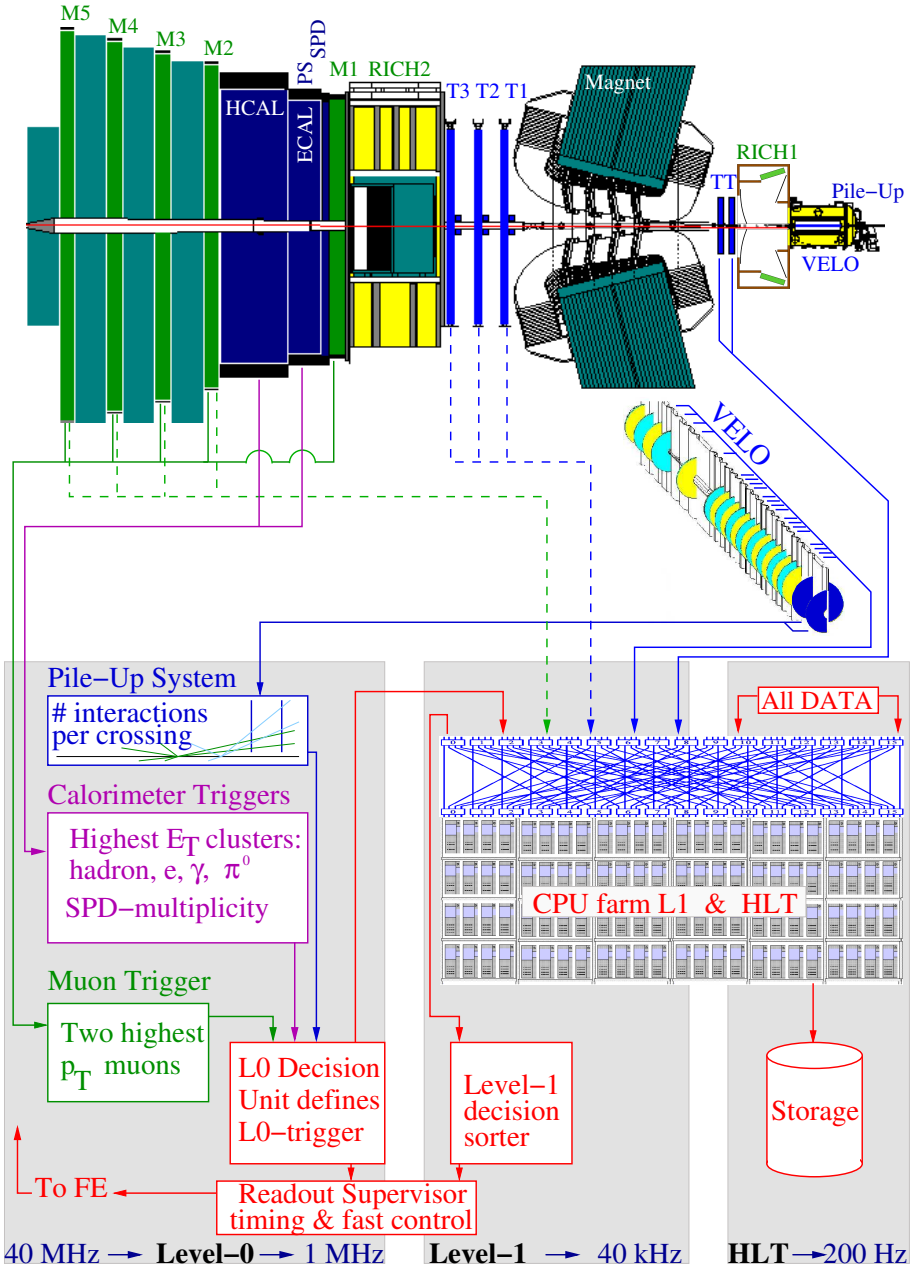



Figure 3.11: *Overview of LHCb trigger levels as described in the Trigger TDR. The muon stations M1-M5 reconstruct two muons per quadrant. The calorimeters are responsible for finding the largest transverse energy photon, $\pi^0$, electron or hadron, the charged particle multiplicity, and the total energy. The pile-up system recognizes events with multiple primary interactions. L0 uses all this information to reduce the output rate to 1 MHz. With the aid of VELO, TT and L0 information, L1 takes the rate down to 40 kHz. Data from all detectors but the RICH are used by HLT to further reduce the rate to 2 kHz. Picture from [55].*

### 3.3.1 Trigger overview

At the LHCb luminosity, the expected frequency of crossings with p-p interactions visible[3] by the spectrometer is about 10 MHz [55]. However, the rate of $b\bar{b}$ events is of only 100kHz, and only 15% of those will be in LHCb acceptance. Moreover, branching ratios of channels of interest for CP violation studies are typically less than $10^{-3}$. Offline selections are tuned to exploit typical $b$ signatures, namely large transverse momentum and high impact parameter[4] (respectively due to the high mass and the long lifetime of $b$-hadrons). Hence it is fundamental for the trigger to recognize those few events that can be later selected, out of the high background.

The LHCb trigger system described in the Trigger TDR [55] featured a multilevel trigger to achieve the reduction of the event rate to 2 kHz (see fig. 3.11). This was accomplished in three levels: a first one, called Level-0 (L0)[5], which was (and still is) implemented in custom electronics due to the tight requirements in terms of speed, while the other two levels, Level-1 (L1) and High Level Trigger (HLT) were to be executed on a farm of commercial PCs. The LHCb readout strategy was however modified in September 2005, when the collaboration accepted the so-called "1 MHz readout proposal" [56]. In the new scheme, all L0 accepted data are sent to the PC farm, rather than a reduced format of only a few subdetectors.

All the trigger and electronics studies described in this document have been completed before September 2005, thus they are based on the old readout scheme (see section 3.3.2). The results and conclusions are still valid in general for the new system. A detailed discussion of the new architecture is beyond the scope of this thesis, however its general principles are described for completeness in section 3.3.4.

### 3.3.2 The old strategy

#### 3.3.2.a L0 trigger

The L0 trigger aims to reduce the event rate from 40 MHz down to 1 MHz. At this rate, in fact, all subdetectors but the RICH can in principle be read out and employed in the subsequent trigger levels. Only the calorimeters, the muon chambers and the Pile-Up Veto have response times short enough to be used at L0. Massive $b$-hadrons are likely to decay into leptons, hadrons or photons with high transverse energy ($E_T$) and momentum ($p_T$). Therefore L0 reconstructs:

- the highest $E_T$ hadron, electron or photon clusters in the calorimeters;
- the two highest $p_T$ muons in the muon chambers.

Events are rejected on the basis of global variables such as charged track multiplicities and the number of interactions as reconstructed by the Pile-Up system (an upstream section of the VELO). At LHCb luminosity 40% of the events have more than one p-p interaction. These events are difficult to reconstruct, and could be accepted by high $p_T$ triggers, filling

[3] A visible interaction is defined as one producing at least two charged tracks with a sufficient number of hits in the VELO and T1-T3 to be reconstructed

[4] The impact parameter of a given track is defined as the distance between the Primary Vertex (PV) and the point of closest approach of the track to the PV. It can be shown that the mean impact parameter of a decay is proportional to the lifetime of the decaying particle.

[5] Not for simplicity's sake, LHCb L0 corresponds to the Level-1 trigger of the other LHC experiment. In the same way, LHCb L1 and HLT correspond respectively to Atlas or CMS L2 and L3.

up the L0 bandwidth. The Pile-Up system detects these events by histogramming the $z$ intercept of all tracks made by the combination of two hits. Events with more than one peak are discarded. The efficiency on single interaction events is 90%, while the rejection power on multiple interactions events is 70%.

The Pile-Up veto reduces the event rate down to 9 MHz. The factor 9 reduction still needed is achieved with cuts on transverse energy and momentum:

**Electron trigger** Combines M1, PS and ECAL data. Requires $E_T \geq$2.8 GeV.

**Photon trigger** Combines M1 (used to veto), PS and ECAL data. Requires $E_T \geq$2.6 GeV.

**Hadron trigger** Combines M1, PS and HCAL data. Requires $E_T \geq$3.6 GeV ;

**Muon trigger** Reconstructs tracks in M1-M5, then checks their compatibility with the hypothesis of a high $p_T$ muon coming from the VELO region. Requires $E_T \geq$1.1 GeV for a single muon candidate, $\sum E_T \geq$1.3 GeV for more than one muon.

The efficiencies on interesting physics channels range from 90% for channels with muons, to about 50% for purely hadronic channels.

#### 3.3.2.b L1 trigger

The L1 trigger has access to L0 information, and to VELO and TT data. The L1 algorithm will be discussed in more details later, but it features track reconstruction starting from VELO hits, muon matching using L0 information, and momentum measuring from TT hits. The L1 decision is then taken combining the results of a generic algorithm that selects $b$ events by asking for high impact parameter and $p_T$, with specific algorithms that enhance the content of channels with electron, photon, single and di-muons, using L0 information [57]. At L1, the event rate is reduced to 40 kHz, while the efficiencies range from around 80% for hadronic channels to around 90% for channels with muons.

#### 3.3.2.c High Level trigger

The HLT has access to all detector data. The HLT algorithm can be divided in the following steps [58]:

- Reconfirmation of the L1 algorithm, taking advantage of the better momentum resolution due to the employment of T1-T3, and fast muon identification;
- An inclusive stream of $D^*$ and muon events is formed to cover about 1.8 kHz of the bandwidth;
- Exclusive selection of specific channels (meaningful for LHCb physics goals), covering the remaining 200 Hz.

Preliminary studies show efficiencies of the order of 95% for dimuon channels, and around 90% for channels with two hadrons in the final state.

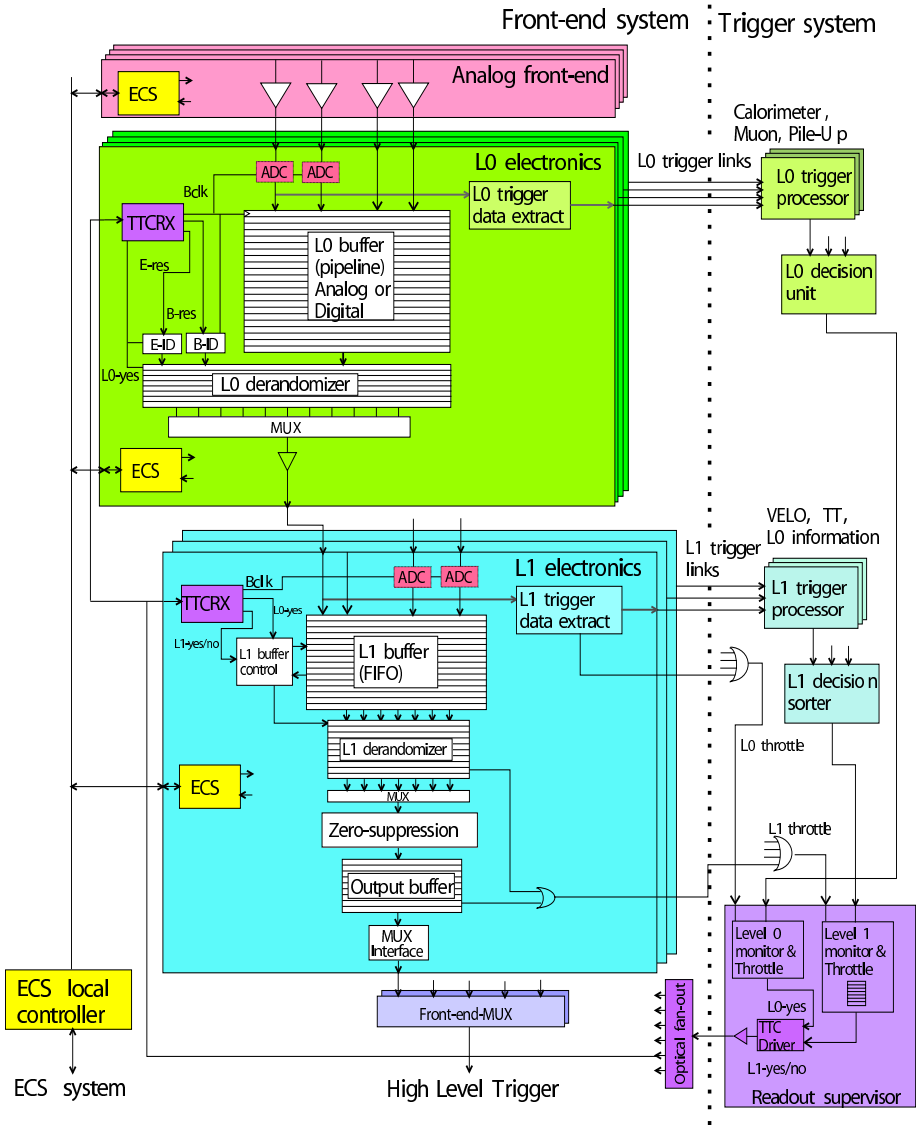



Figure 3.12: *Overview of LHCb Front End architecture. See text for explanation. Picture from [55].*

### 3.3.3 Data acquisition overview

Because of the high radiation level, the electronics in the proximity of the LHCb detector is kept to a minimum. It is responsible for data extraction and transmission over long cables to the counting house. All the data taking is coordinated by the LHCb Time and Fast Control system (TFC)[59]. A scheme of the data acquisition is given in fig. 3.12. The general idea behind it is simple: each trigger level electronics consists of a buffer (defined by the trigger latency) where data are stored waiting for the trigger decision, an interface to the trigger to receive it, and an output buffer where data are derandomized and sent out to the next trigger level. The L0 electronics is the part of the DAQ that comes before the L0 decision, while the L1 electronics is the part before the L1 decision, but after L0 decision.

L0 data coming from the analog Front End (FE) are collected and processed in the counting room, and the decision is sent to the L0 Decision Unit. The L0 latency, which is defined as the time between a p-p interaction, and the arrival of the L0 decision to the FE electronics, has been fixed to 4 $\mu$s (160 LHCb clock cycles). This includes time-of-flight, cable lengths, and 2 $\mu$s for the actual processing. The L0 readout of a complete event is done is 900 ns, which gives a maximal L0 accept rate of 1.1 MHz. The derandomizer buffer is 16 events deep, and overflows are prevented by the Readout Supervisor (RS), which throttles the L0 accept rate if the buffer is getting full. The L0 electronics requirements are specified in [60].

The L1 latency is variable, but all events are to be delivered in chronological order to the trigger processors[6]. Following the same order, the L1 decision is then given to the RS. The maximum output rate has been fixed to 40 kHz, and the buffer depth to 58254 events, which corresponds to a maximal latency of 52.4 ms[7] [61]. Again buffer overflow is prevented by the L1 throttle given by the RS. Apart from data buffering and derandomization, noise filtering and zero suppression are also implemented in the L1 electronics.

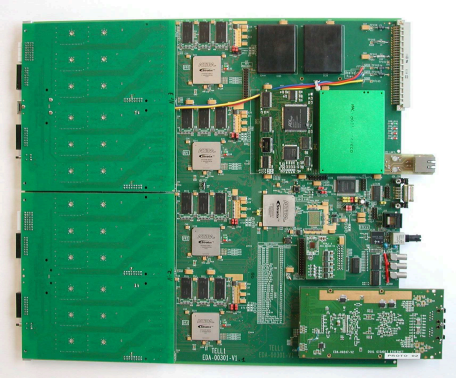


Figure 3.13: *A picture of the TELL1 readout board.*

The L1 readout board that has been chosen for LHCb is called Trigger ELectronics and Level-1 (TELL1) board [62]. It started out as the VELO readout board and has now been adopted by all LHCb subdetectors but the RICH. The R&D for this device started in 1998 [63]. Three prototypes have been built since then: RB1, a 10 MHz board with 2 channels, in 1999; RB2, a 40 MHz board with 4 channels, in 2000 [64]; and RB3, again a 40 MHz board but with 16 channels, in 2002 [65]. RB2 has been extensively used in test beams, while RB3 has been used as a test platform. Part of this thesis will be dedicated to describe the R&D for the TELL1 board.

[6] The described scheme refers to the old readout strategy, previous to the "1 MHz readout proposal".

[7] The L1 event fragment size is 36 words (32 for the actual data and 4 for the header), and the buffer size is 2 M words. This results in 58254 events spaced of 900 ns (L0 readout rate), hence the L1 latency is 58254 $\times$ 900 ns = 52.4 ms.

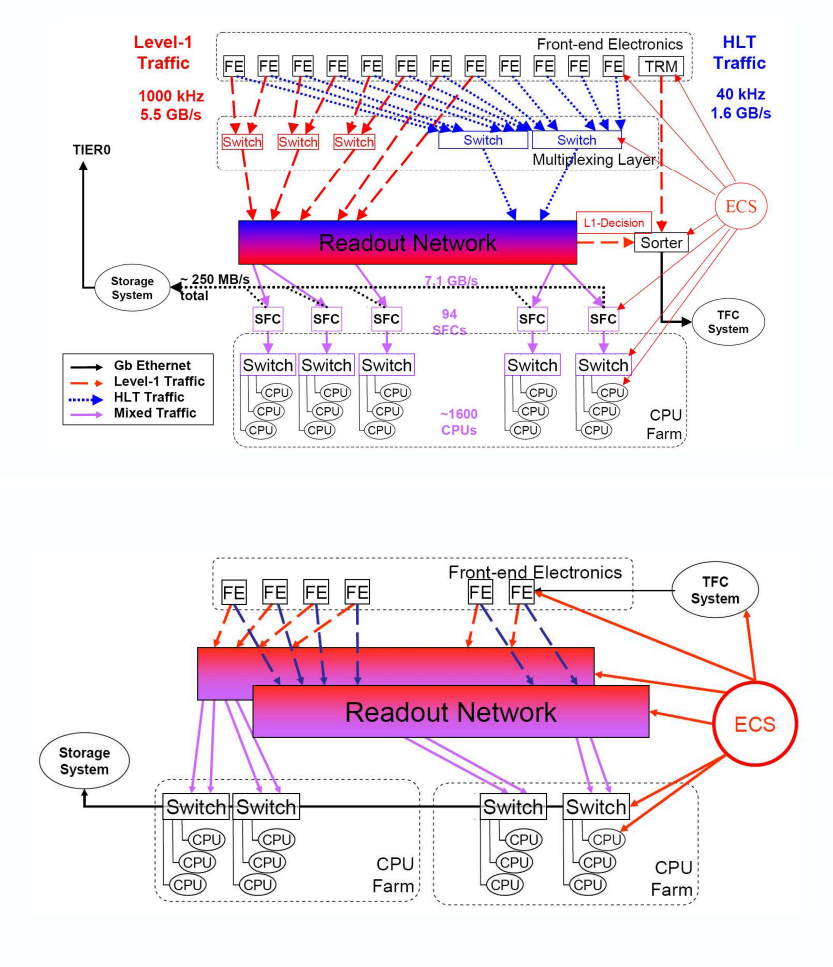



Figure 3.14: *The old (top) and new (bottom) architecture of the LHCb online system. Many elements of the old architecture have been removed in the new scheme: the Sub-Farm Controllers (SFCs), the L1 Trigger Receiver Module (TRM) and the decision sorter. Picture from [66].*

### 3.3.4 The 1 MHz readout

The L0 readout strategy remains unchanged. All subdetectors are then readout in a single data-stream at L0-accept rate (in the old scheme, only the VELO and TT were readout at 1.1 MHz). All information are therefore available for the trigger algorithm. However the entire HLT sequence cannot obviously run at 1.1 MHz. A still-to-be-defined sequence of algorithms will gradually reduce the event rate to the originally foreseen values, by exploiting the current L1 strategy, i.e. selecting events with detached secondary vertices, but without having the current L1 limitation of running at 40 kHz. Hence the required computing power does not increase dramatically, as one could naively expect (by applying the current HLT algorithm at 25 times more events). Since more detectors are added to the 1 MHz data path, the new scheme requires however more bandwidth, which can be obtained increasing the number of TELL1 boards (by $\sim$10%).

The 1 MHz solution has many advantages. Firstly, it is simpler (as one can see from fig. 3.14) since it removes the need for two separate data streams (L1 and HLT) and the

L1 latency limitation for event processing. The trigger scheme is more flexible since all detector information is available anytime with full granularity and precision. This opens up new possibilities in terms of physics performances[8]. The main drawback is that it is more vulnerable to changes of average event sizes. In the worst scenarios, this can be controlled by lowering the L0 readout rate.

## 3.4 The LHCb software

Particle physics experiments are getting more and more complex. To understand the detector response, and to develop an efficient reconstruction software, precise simulations are needed. Obviously, as of today, there is no LHCb data to analyze. The whole collaboration is preparing the software framework that will be used from 2007, when real data will become available. The logical structure of the software is common to all high energy physics experiments (see fig. 3.15). On one side we have the events generation and the simulation of the detector response, while on the other we have raw data directly coming from the detector. This latter is of course only available when the experiment is taking data. The last steps are common to both data paths and involve event reconstruction and analysis.

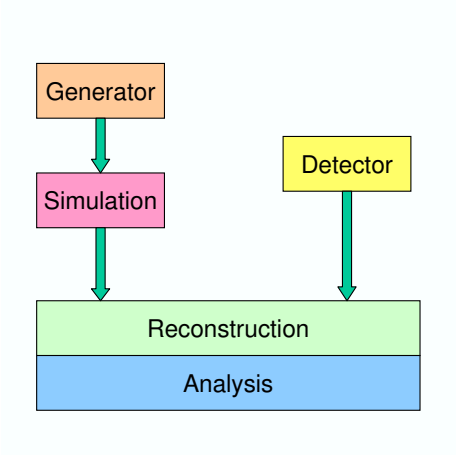



Figure 3.15: *Data flow of a typical analysis framework.*

The LHCb software is evolving in time, as new contributions become available. Here we give the status of the software that was used for the physics analysis described in part III.

The LHCb offline software performs the following tasks [46]:

**Event generation** Two different packages are used at this stage: Pythia and EvtGen [67]. Pythia is used to generate p-p interactions at $\sqrt{s} = 14$ TeV, including hard QCD processes, single and double diffraction, and elastic scattering. No acceptance cut is imposed for minimum bias events, while when generating $b$ events a true polar angle smaller than 400 mrad is required for the particle that contains the $b$ quark. Particles produced by Pythia are decayed by EvtGen [68].

**Particles tracking through the detector** This task is performed by the GEANT4 package. Both active and passive materials are included in the LHCb detector description. The energy cutoff has been chosen to be 10 MeV for hadrons, and 1 MeV for electrons and photons.

**Simulation of the detector response** In each sensitive region the detector response is simulated as a function of the arrival time of the particle, taking into account the sensitivity of each detector. Cross-talk and electronic noise is also included. LHC

[8] Even if no specific implementation to demonstrate the improvement exist at the moment, many previous studies have shown that the L1 trigger algorithm could significantly gain in efficiency by using more subdetectors [55].

bunch crossings are considered, but the LHC bunch structure is ignored. The lifetimes of particles across the detector can span more than 25 ns, so that spillover is also taken into account.

**Simulation of the trigger decision** L0, L1 and HLT algorithms are run over digitized raw data, and their output simulates the data how they will actually be stored during data taking.

**Event reconstruction** (including track finding and particle identification) Track reconstruction aims to find all tracks from the VELO to the Calorimeters, using hits in the VELO itself and in the trackers (TT, IT and OT). It actually consists of two steps: pattern recognition and track fitting. Particle identification is provided by the RICH, the Calorimeters and the Muon detector. Hadrons are identified in the RICH and HCAL, while photons, electrons and $\pi^0$ (using the decay $\pi^0 \to \gamma\gamma$) in ECAL. $K^0_S$ are identified through the decay into two charged pions.

**Offline selection of specific decay channels** Interesting $b$ events are selected from the combinatorial background mainly by applying cuts on the tracks transverse momenta and impact parameters, vertex $\chi^2$ distributions, and invariant masses.

In the last three steps simulated data are processed as if they were real data. Monte Carlo (MC) truth information are only accessed to assess the various algorithm performances.

LHCb software packages are all based on the Gaudi framework, an experiment independent project that provides the necessary interfaces and services for building data processing applications in the high-energy physics domain [69]. Both event generation and simulation of the detector response are done in the Gauss application. Boole takes as input the Gauss simulation, adds hits from spillover events and LHC background, and simulates the detector response [70]. It simulates also the trigger behavior, and performs the digitization. The reconstruction program is called Brunel [71], which executes the tracking and vertexing algorithms. Last but not least comes DaVinci, the LHCb analysis program [72], in which particles are formed and events are selected according to their physics content.

Part II

# Contribution to the L1 electronics

Chapter 4

# R&D for the TELL1 board: choice of the L1 buffer technology




*This chapter describes the technical part of this thesis work, and is a contribution to the R&D for the design of the TELL1 board. It focuses on the tests aimed to choose the L1 buffer memory technology, and in particular the feasibility of a mixed DSP-FPGA architecture.*

## 4.1 Introduction

The LHCb trigger strategy, as described in the Trigger TDR [55], is based on three levels (see also the scheme in fig 4.1)[1]:

- L0: a fully synchronous and pipelined trigger with a fixed latency of 4 $\mu$s and maximal accept rate of 1.11 MHz;
- L1: a software trigger with maximal latency of 52.4 ms and maximal accept rate of 40 kHz;
- HLT: a software trigger with output rate of $\sim$2 kHz.

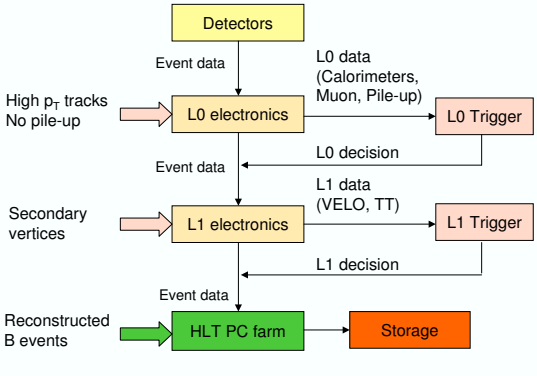



Figure 4.1: *LHCb multi-level trigger scheme. Picture taken from [73].*

In the Technical Proposal [45], only VELO data were supposed to be used at L1, but more recent optimization studies have shown the utility of using also information from

[1] This scheme is not valid anymore, but it was the current implementation at the time of the development of the L1 electronics (see 3.3.1).

the trackers, and possibly the muon stations [55]. The Lausanne electronics group is responsible for developing an "off detector" acquisition board for the VELO and the Silicon Tracker. The main task of the board is to read out L0 accepted data and output them to the L1 and HLT trigger system after some processing. To accomplish this, various prototypes have been designed: the so-called RBx series (Readout Board 1, 2 and 3).

However, as more and more subdetectors were added to the L1 trigger, the necessity of having a common L1 and HLT data path, and data buffering during L1 latency, pushed the collaboration to the development of a common readout board (TELL1) [74]. Since intensive R&D had already been done through the years for the VELO readout, the choice of taking these prototypes as starting point for TELL1 development was almost obliged. The main tasks of the TELL1 board were: take L0 accepted data as input, and output them to L1 and HLT after data processing which includes event synchronization, L1 pre-processing and zero suppression, L1 buffering, and HLT zero suppression (all these terms which might sound obscure will be explained in the following paragraphs). Various solutions for implementing the different functionalities have been studied in the last years. In this chapter, the R&D for choosing the L1 buffer memory technology is described.

The current LHCb trigger strategy does not foresee two separate data paths to the L1 and HLT trigger. All subdetectors are readout in a single data-stream at L0-accept rate (see 3.3.1). Thanks to the flexibility in the design of TELL1, the board can still be used in the new scheme without modifications. The TELL1 board will be used by the VELO, the Trackers (Trigger, Inner and Outer), the Muon detector and the calorimeters. It will also be used as L0 Decision Unit, and for the L0 Muon and Pile-up triggers.

At the time of the L1 buffer study, the baseline implementation for the LHCb trigger was the Trigger TDR implementation. Throughout this chapter, we therefore refer to the old scheme. The TELL1 board will be used without changes also in the new scheme, thus the conclusions of this study are not affected by the strategy change.

## 4.2 The readout board RB3

### 4.2.1 The VELO readout

The L1 buffer studies have been carried out using RB3, the last prototype of the TELL1 readout board. Since RB3 had been originally developed for the Vertex Locator, a short summary of the VELO readout scheme is given here (more information on the subject can be found for example in [65]). The VELO detector is divided into 21 stations, each one of them is equipped with 4 silicon sensors (2 for measuring the $r$ coordinate, and 2 for the $\phi$ coordinate, see also section 3.2.1). Each sensor features 2048 strips, which are readout by 16 FE (Front-End) chips.

Analogue rather than binary readout has been chosen for the VELO since it provides better resolution and provides more information on the distribution of radiation damage to the silicon detector [45]. The FE chip for the VELO readout has been developed on the basis of the HERA-B HELIX chip, and is called Beetle. It features standard radiation hard 0.25 $\mu$m CMOS technology. The Beetle accepts 128 input channels at 40 MHz. The data are brought off-chip at a clock frequency of 40 MHz, multiplexed to 4 analogue signals (32 channels per output line) [75].

Analogue signals from the FE chips are carried out from the vacuum tanks to repeater cards, and then via analog links over a 60 m distance to the L1 readout boards located in the counting room, which is located in a radiation free area (see fig. 4.2), thus allowing

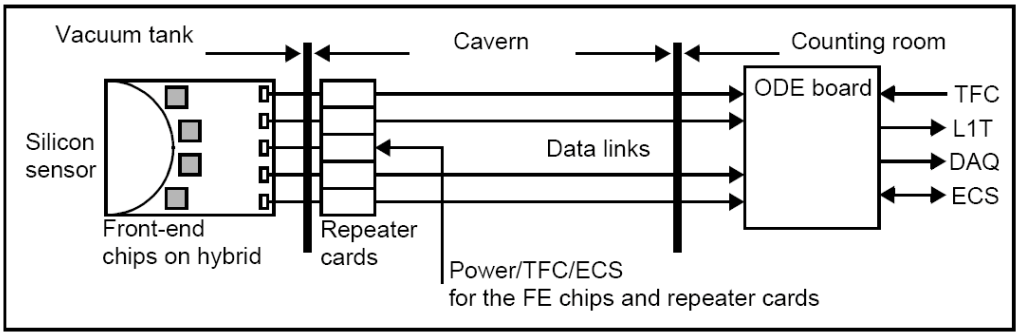



Figure 4.2: *VELO readout scheme. Analog signals coming out from the Front-End chips (FE) are sent to the counting room by repeater cards located just outside the vacuum tank. They are readout by the TELL1 board (here called "ODE" Off Detector Electronics), and finally sent out to the L1 trigger and the DAQ. Picture from [65].*

the use of standard components for the L1 electronics. Each sensor is readout by one TELL1 board, therefore each board has 64 analog inputs, corresponding to the output of 16 Beetles.

### 4.2.2 RB3 technologies

RB3 has all the functionalities of the final TELL1 board, but a restricted number of input channels (16 instead of 64). Its main tasks are:

- Digitization of the analog data coming from the FE chips. This is accomplished by Fast Analogue-to-Digital Converter (FADC) chips.
- Digitized data are synchronized, checked for errors, zero suppressed (this is called L1 trigger preprocessing) and sent out to the L1 trigger.
- L1 buffering during L1 latency: digitized data need to be stored on board, waiting for the L1 decision.
- HLT preprocessing: L1 accepted data undergo a zero suppression algorithm (similar to L1T preprocessing), before being sent out to the DAQ.

All these tasks need to be implemented in microprocessors, and the technology choice depends heavily on the type of processing and the performance needed. Possible solutions for the TELL1 design are[2]:

- ASIC (Application Specific Integrated Circuits). It is a chip which has been specifically designed for a particular application. The required logic is burned in, thus ASICs are not reprogrammable. They are produced only once the design has been

[2]An interesting dissertation on the various kinds of microprocessors available to system designers can be found in Appendix B of [76].

finalized. Due to their lack of flexibility, they have not been considered a feasible solution for the TELL1 project.

- FPGA (Field-Programmable Gate Array). It consists of arrays of AND and OR gates (usually thousands of them) that can be programmed to perform complex functions. Modern FPGA families also include higher level functionality fixed into the silicon. Example of these include multipliers, generic DSP (see below for a DSP definition) blocks, embedded processors, high speed IO logic and embedded memories. FPGAs are very versatile, since the single logic elements are available to the programmer (via HDL, the Hardware Description Language), but using them efficiently requires a good knowledge of the chip and of hardware issues.

- DSP (short for Digital Signal Processor). It is a microprocessor specifically designed for performing the mathematical operations involved in digital signal processing, typically Fast Fourier Transforms or various filter techniques. Most DSPs functions are built-in the chip and programmable via high level languages as C. This makes them easier to use than FPGAs, but less versatile and slower.

A description of RB3 architecture and dataflow is given in the appendix 4.A (at the end of this chapter). Here we focus on the L1 and HLT preprocessing since they are relevant to the L1 buffer R&D.

The L1T preprocessing has to run at L0 accept rate (1.1 MHz), thus this task can only be accomplished by FPGA chips. On the other hand, HLT preprocessing is steered by L1 accepts, whose rate is quite lower (40 kHz). Hence a DSP approach becomes possible.

## 4.3 The L1T and HLT preprocessing

The functionalities of L1T and HLT preprocessing are similar since they both involve cluster detection and zero suppression. The input of the L1 and HLT algorithm are clusters of adjacent strips. The selection of hits to form the clusters is quite delicate, since one has to be aware of faulty or too noisy channels, and of the correlation of electronic noise. To perform this task a simple algorithm (Linear Common Mode Suppression, LCMS) has been developed, and his parameters optimized to achieve the highest possible trigger efficiency [77]. A description of the LCMS algorithm will follow.

L1T and HLT functionalities (in chronological order) are:

**Pedestal subtraction** An offset is subtracted to each detector channel: it is the electronic noise specific to each strip. It can be determined from uncorrected detector data taken in a special run with no $p$-$p$ interactions. Pedestal values are downloaded via ECS at initialization (1 Byte per channel is reserved to store the pedestal value). In the case that pedestal values fluctuate often during data taken, the possibility of a local and continuous update has been studied for the TELL1 board [76], but had not been implemented in RB3 tests.

**Topological reorder** Some rearranging of the detector channels is performed in case the readout order differs from the geometrical order.

**Faulty channel masking** Too noisy or dead channels need to be masked out for the following hits detection. A table containing the faulty channels is also downloaded via ECS at initialization.

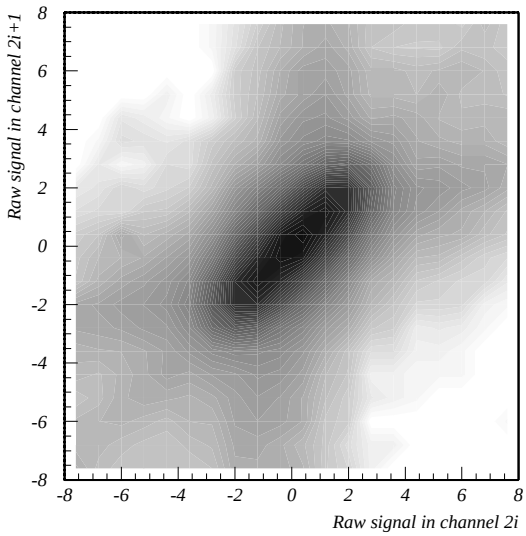



Figure 4.3: *Correlation of raw signal in two consecutive strips in a testbeam run using the SCTA chip. The level of gray indicates the probability density. Plot obtained with May 1999 testbeam data [2].*

**Linear Common Mode Suppression (LCMS)** Since in most cases the noise has the form $a + bi$, where $i$ is the channel number, a simple linear common mode reduction is applied. The implementation of the algorithm is kept as flexible as possible, to allow modifications or even other algorithm to be implemented in case of need.

**Hit detection** After LCMS, if a channel value is above a certain threshold, then the corresponding strip is considered to have been "hit" by a charged particle passing through. The hit thresholds are defined individually for each channels, and again they are contained in a table downloaded at initialization via ECS.

**Cluster encoding and encapsulation** Clusters of one or more strips are formed. The two (L1T_ and DAQ_) Link FPGAs receive clusters from the SPP FPGAs and DSPs, and build an event fragment to be sent to L1T and HLT via S-Link connections. Since the clusterization and encoding scheme is different for L1T or HLT preprocessing, it will be described in more details in section 4.5.2.

### 4.3.1 L1T and HLT zero suppression

Signals coming from adjacent strips are strongly correlated (as can be seen in fig. 4.3 from the elliptical shape centered around (0,0)). The common-mode noise origin could be radio-frequency pickup (from the beam itself, which is quite close to the VELO sensors) or the capacitive cross-talks in the strips and routing lines (induced by power supply variation in the FE chips, or ground loops over the transmission lines). The common mode noise is higher in the outer part of the VELO (for $r$ sensors) i.e. where the strips are longer. A detailed analysis on noise dependency on geometry can be found in [78].

The linear dependence of the common-mode noise with the strip number can be effectively used to reduce the noise. This can be seen in fig. 4.4, where the rms of the noise of all strips in a testbeam sensor is shown before and after the application of the LCMS algorithm.

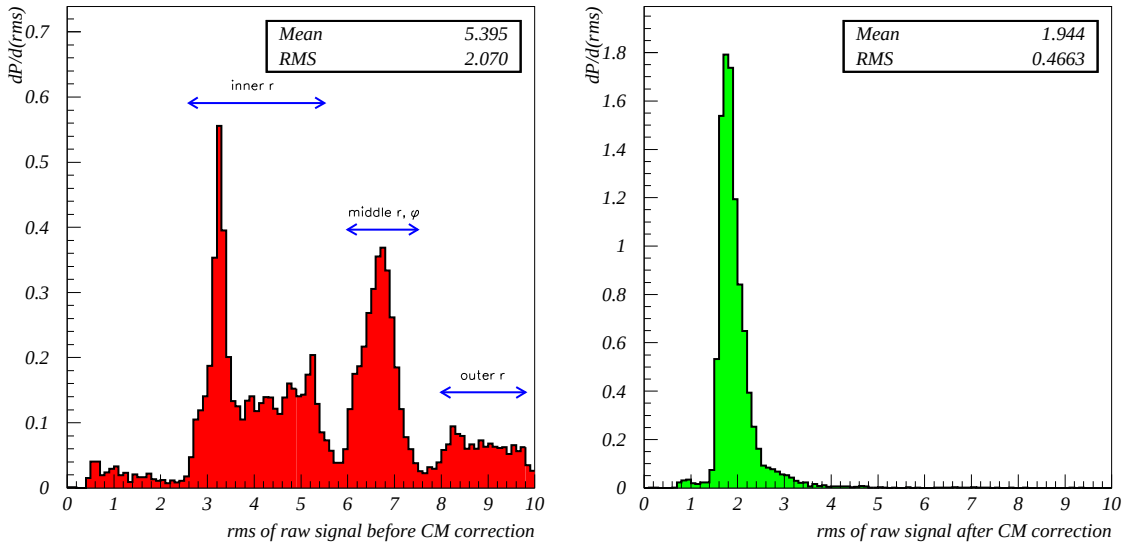



Figure 4.4: *Distribution of the rms of the raw signal before (left) and after (right) CM correction. The origin of the various peaks in the uncorrected distribution are indicated (TP geometry). Plots from [2].*

The signal $y_i$ in strip $i$ can therefore be described by the following expression:

$$y_i = \bar{y}_i + a + b \cdot i + u_i + C_i$$

where

$\bar{y}_i$ is the pedestal of strip $i$, i.e. the mean value of $y_i$ when there is no signal in $i$.

$a$ and $b$ are respectively the offset and the slope common to all strips read out by the same chip and transmitted by the same transmission line (32 strips in the present design).

$u_i$ is the uncorrelated (irreducible) part of the noise. It is assumed to be a Gaussian distributed random variable. After common mode noise suppression the average strip rms is about 2 ADC counts, as can be seen in the right plot of fig 4.4. If the correction is perfect, this would be the rms of $u_i$.

$C_i$ is the signal due to the charge deposited in strip $i$.

### 4.3.2 The Linear Common Mode Suppression algorithm

The LCMS is applied on a set of 32 detector channels (due to the features of the Beetle readout), and it consists of two identical iterations, in which a linear approximation of the common mode is evaluated. This involves the calculation of a linear regression, with some approximations introduced to save resources in the real implementation of the algorithm.

The function for a linear regression is given by:

$$\tilde{y}(x) = \bar{y} + \frac{\sum_{i=0}^{N-1} x_i y_i - \bar{y} \sum_{i=0}^{N-1} x_i}{\sum_{i=0}^{N-1} x_i^2 - \bar{x} \sum_{i=0}^{N-1} x_i}(x - \bar{x}) \tag{4.1}$$

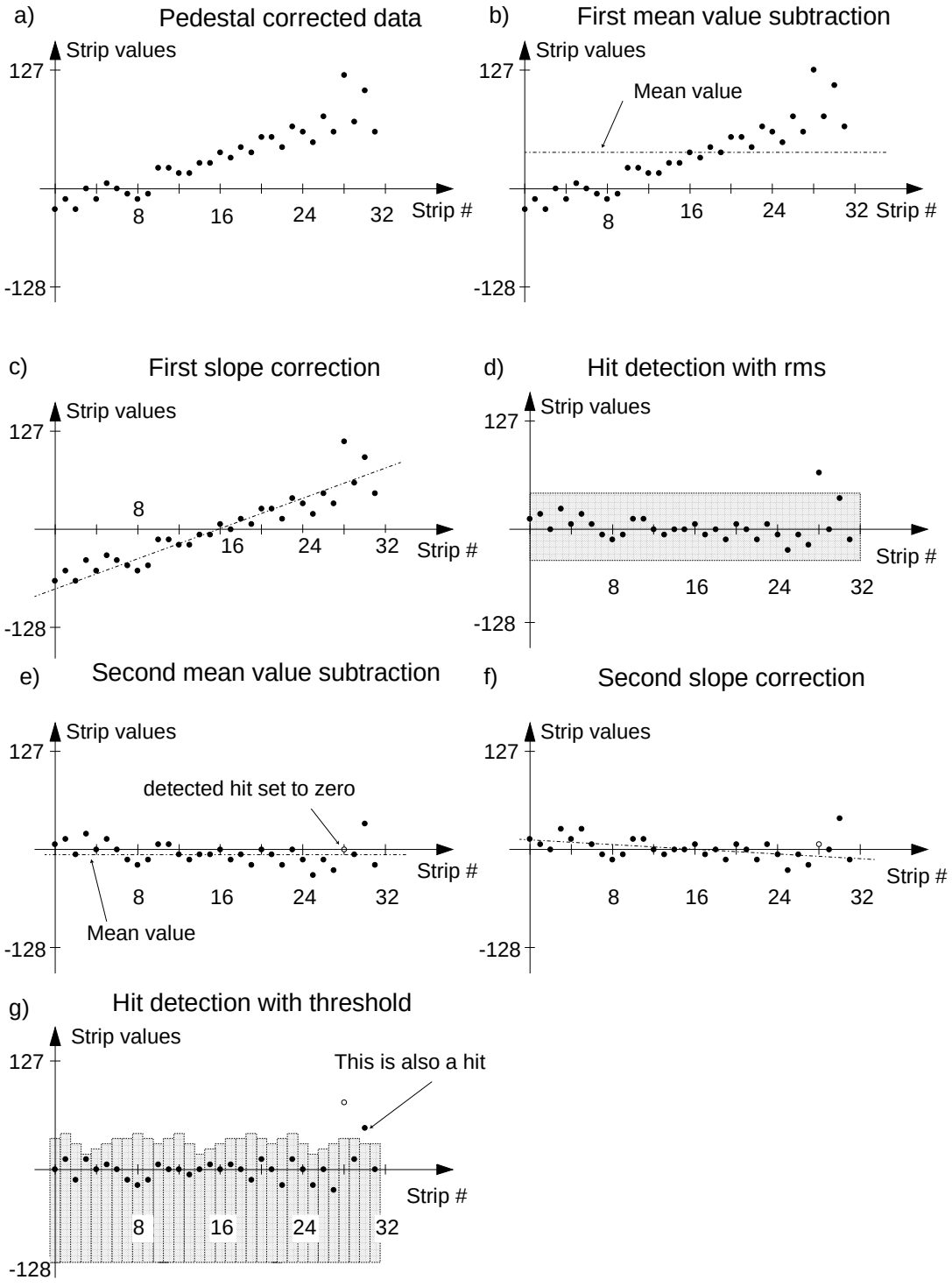



Figure 4.5: *Principle of the LCMS algorithm. After pedestal subtraction (a), the 32 sample values are shifted to obtain a mean value of 0 (b). Then a first linear regression is done (c), which leads to the distribution in (d), whose rms is calculated (the hatched region shows a window whose amplitude is the rms). Data outside of the window are tagged and zeroed (e). Then a second linear regression is applied (f). This can reveal hits hidden by large fluctuations during the first iteration. Hits detection is then performed using individual thresholds (g). Figure from [77].*

where $N$ is the number of samples, $x_i$ and $y_i$ are the Cartesian coordinates of the sample points and $\bar{x}$ and $\bar{y}$ are the mean values over all samples in $x$ and $y$ direction. This formula can be simplified if a translation is performed in such a way that the average values $\bar{x}$ and $\bar{y}$ are close to 0. This is accomplished in the following way. Since the samples are about equally spaced in $x$, and by taking $x_i = i - 16$, one can approximate:

$$\bar{x} = \frac{1}{32}\sum_{i=0}^{31} x_i = -\frac{1}{2} \approx 0 \tag{4.2}$$

In order to center the ordinate at 0, we shift the $y$ values by subtracting the average

$$a_i = y_i - \bar{y}_i \tag{4.3}$$

Then equation 4.1 can be approximated as follows:

$$\tilde{a}(x) = \frac{\sum_{i=0}^{31}(i-16)a_i}{\sum_{i=0}^{31} x_i^2}\, x \tag{4.4}$$

with

$$\sum_{i=0}^{31} x_i^2 = 2736 \tag{4.5}$$

The division by the number 2736 is not an easy task to perform in an FPGA, since it is not a division by powers of 2. We can approximate:

$$2736 \approx \frac{2^{13}}{3} = 2730.\bar{6} \tag{4.6}$$

and replace the division by a multiplication by 3 and a simple shift operation. The error introduced by this approximation is negligible for 8 bit precision.

**First iteration**

To summarize, after pedestal subtraction, the following steps are performed in chronological order:

- Mean value calculation
$$\bar{y} = \frac{1}{32}\sum_{i=0}^{31} y_i \tag{4.7}$$
- Mean value subtraction
$$a_i = y_i - \bar{y} \tag{4.8}$$
- Slope calculation
$$b_1 = \frac{3}{2^{13}}\sum_{i=0}^{31}(i-16)a_i \tag{4.9}$$
- Linear CM subtraction
$$Y_i = a_i - b_1(i-16) \tag{4.10}$$
where $Y_i$ contain the corrected signal values.

### First hit detection

After the first linear CM subtraction the channels with an extreme value (positive or negative) are identified in the following steps:

- Calculation of the variance of $Y_i$. Since the mean value is now $0$, we simply have

$$V = \frac{1}{31}\sum_{i=0}^{31} Y_i^2 \tag{4.11}$$

- The signal of each channel $i$ is then compared to the square root of the variance.

$$Y_i^2 F_1 > V \tag{4.12}$$

  where $F_1$ is an integer constant which has to be optimized. For instance, $F_1 = 3$ is equivalent to a $3.2\sigma$ cut

$$\sqrt{\frac{31}{F_1(=3)}} \approx 3.2 \tag{4.13}$$

In this way the corrected $Y_i$ valuer are compared with an adaptive limit built from the rms of the sample distribution.

### Second iteration

The channels tagged by the first iteration are set to zero. A second mean value $\bar{Y}$ and slope $b_2$ are calculated in the same way as in the first iteration. The CM found in this way is finally subtracted from the output data of the first iteration giving the final common-mode corrected data:

$$c_i = Y_i - \bar{Y} - b_2(i - 16) \tag{4.14}$$

### Hit detection

The hits are found by comparison with a channel individual hit threshold value ($T_i$). Channel $i$ is a hit if $c_i > T_i$. The optimization of $T_i$ is described in [77].

Other algorithms (as Fast Fourier Transform, Finite Impulse Response or wavelets) have been tested with Monte Carlo and test beam data, and found to be even more efficient in the case of a wave-shaped noise, typical for example of radio frequency pickup [2].

### Clusterization

Clusters are formed according to the following scheme:

- cluster of one hit: the cluster and strip position coincide;
- cluster of two hits: the cluster position is the first hit strip, an extra bit indicates two-strip clusters;
- cluster of more than two hits: the first two strips are treated as a two-strip cluster, remaining hits are treated independently;
- clusters between adjacent detector zones are not formed.

The implementation of L1T preprocessing was prototyped on a FPGA to estimate the needed resources [77]. The HLT preprocessing will be treated in more details after a summary of the technologies involved in its implementation.




Figure 4.6: *The TMS320C6711 DSP Starter Kit (bottom) with a mezzanine card containing a first implementation of the L1 Buffer (top) used for first tests. Asynchronous memory has been used for the L1 Buffer.*

## 4.4 A DSP-FPGA shared memory implementation for the L1 Buffer

Since L1 accept rate is 25 times lower than L1T preprocessing, a DSP approach is possible for HLT preprocessing. Efforts have been concentrated on the TMS320C6211 (from now on called simply 6211). The 6211 is a fixed-point DSP by Texas Instruments (TI) which combines good performances (CPU running at 166 MHz) with a low price (25$ per chip) [79].

A first series of tests have been conducted in early 2002, to show that L1 electronics requirements [61] could be satisfied with such a system, and in order to guide the necessary decisions for hardware development of the final DAQ_DSP mezzanine card.

To this aim an evaluation board by TI (called DSK, DSP Starter Kit, see picture 4.6), equipped with a TMS320C6711 DSP [79] has been used. This is a floating-point chip with the same performances as the 6211 DSP for what concerns fixed point operations, which are the only ones required by the LCMS algorithm.

The DSK has been used together with a simple mezzanine card equipped with ASRAM (see section 4.4.1 for a description of the various memory types) as implementation of the L1 Buffer. Despite the fact that asynchronous memory was not fast enough for our needs, there was not much choice for these first tests, since the DSK does not support synchronous memory.

In order to check TI competitors' DSPs, the code for DAQ zero-suppression has also been run on a ADSP-2161N (using a simulator). This chip (100 MHz CPU frequency, 1-Mbit On-Chip RAM for 39$) is the direct opponent by Analog of the TI DSP [80]. Benchmarks resulted in slightly less (10%) performances, so the TI DSP was kept as final choice for the DAQ_DSP.

Before starting describing the tests or the final board itself, a brief description of the technologies involved becomes necessary.

### 4.4.1 Memory types overview

Various solutions for the L1 Buffer have been investigated among the possible choices of memories that could be easily interfaced with the DSP (i.e. that could be accessed using the built-in memory controller). A short summary of the available memory technology follows [81]:

**FIFO** (First In First Out). It consists of two independent ports, one for reading and one for writing. As the name suggests, what has been written in first, is also first to be readout. The address generation is taken care of automatically by the memory logic. The latest devices also allow to increase the read pointer without actually reading the data out (thus allowing to change the read order). For their simplicity and speed, FIFO are very convenient to use, especially to interface subsystems with different clock domains and bus width. They are also rather expensive (high end devices, 2 to 4 times smaller than SRAM, can cost up to 3 to 4 times more) since they are produced in smaller quantities compared to standard SRAM.

**SRAM** (Static Random Access Memory). It has only one data port and the address port, thus read and write operations have to be scheduled by the controller. The major advantage is that as long as power is applied, the transistor cell maintains a stored value indefinitely, so no special refresh or control cycles are necessary. The disadvantage is that the density of an SRAM array is much smaller if compared to a DRAM array. Another advantage is that SRAM devices normally utilize a linear addressing scheme. In other words, with the address pins available for a given device, the entire depth of the SRAM memory can be directly addressed. There is no performance penalty for accessing opposite extremes of the SRAM memory. For small data transfers and random access, SRAM performs better than DRAM. Pipeline Static Burst Synchronous memories (SBSRAM) achieve higher performances by registering both inputs and outputs, resulting in a 2-cycle read latency and a 0-cycle write latency.

**SDRAM** (Synchronous Dynamic Random Access Memory). It employs only one capacitor per cell, thus denser memory arrays are achievable. Nevertheless the charge on the capacitor cell leaks over time and must be continuously refreshed. This adds additional complexity to either the DRAM itself or to the memory controller, depending on which device is responsible for refreshing the memory. The DRAM chip is organized in banks, columns and rows, thus a time multiplexed row/column addressing scheme is used. This is an advantage in that a larger address reach is possible with fewer pins. However, additional controller complexity and latency is added since separate control cycles are required for row addressing, column addressing, and other command overhead. DRAMs are especially suited for large data transfer, since consecutive columns can be accessed without having to recharge the row address.

**ASRAM** (Asynchronous Static Random Access Memory). As the name implies, ASRAM operates asynchronously; that is, no clock is used internally to pipeline operations. The address at the inputs (in conjunction with the appropriate control signals) begins the read access to the memory array and the data is available at the outputs some time later. The amount of time between control/address valid signal to output data valid signal is totally dependent on device physics. The opposite is true for writes. The setup time required by the memory before the write actually takes place is dependent on the amount of time it takes for the external data to propagate

into the memory array. Slow asynchronous SRAM may be used as a cheaper alternative if lower performance is acceptable or if a simple shared memory scheme is implemented with some other external device.

Unfortunately when the DAQ_DSP board has been designed, no DSP support for the newer generation memory (as DDR SDRAM[3]) was foreseen. This was due to the fact that DSPs only supported Low Voltage TTL (Transistor Transistor Logic) I/O standard, while a faster and more expensive I/O standard (as SSTL-2) was needed to operate DDRs.

### 4.4.2 The L1 Buffer

The principle of operation of the L1 buffer, as it was outlined in the Technical Proposal [45], is fairly simple: it is a FIFO, with L0 accepted data written at L0 accept rate (1.1 MHz) on the write side. On the read side, the readout is steered by L1 decisions. L1 accepted data are transferred to a derandomizer (needed to uniform in time the event spacing), which finally outputs them to HLT (see figure 4.7). At TP times, a L1 latency of 256 $\mu s$ was easily achievable. Since then, it has grown up by almost 3 orders of magnitude[4] [76]! This is essentially due to the grower complexity of the trigger algorithm which now uses information from several LHCb subsystems [55]. During TELL1 R&D, the latency requirements (and thus the buffer size) kept on increasing, forcing for various solutions to be taken into account to satisfy the new demands.

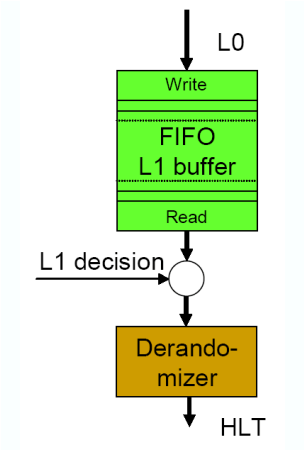



Figure 4.7: *L1 Buffer principle with FIFO. Picture taken from [76].*

The data access can instead be well specified: L0 accept rate being 1.1 MHz, the event spacing is 900 ns.[5] The write access can be done in so-called "bursts" of 36 words to consecutive addresses. However the read access is much less frequent, L1 accept rate being only 40 kHz. Hence the read and write port can be shared, and the bus must be arbitrated by the controller.

Despite the simplicity of the mechanism, FIFOs soon seemed too expensive and limited in size to be considered as a real solution for the L1 buffer. At the time of the DSP studies, the buffer depth was of 2048 events (now is 58254), thus allowed for SRAM or DRAM to be considered. The major advantage of DRAM over SRAM is that SRAM arrays are much larger. However, because of the needed refresh cycles and the complicated address scheme (multiplexed row/column addressing), DRAM is more difficult to use and slower. The choice has been made taking into account the fact that the bus would be shared between the RB3 FPGAs, called SPP (see appendix 4.A), for writing at L0 accept rate, and the DSP (reading at L1 accept rate). The complication of having a shared DRAM interface made us prefer SRAM. This allowed us to implement a simple hand-shaking mechanism to arbitrate the bus (see section 4.4.3).

[3]DDR (Double Data Rate) memory is used commonly nowadays. It achieves higher transfer rates by sending the data and address respectively on the rising and the falling edge of the clock.

[4]Before falling to 0 in the new trigger scheme!

[5]Each event is made of maximum 36 words and one clock cycle lasts 25 ns.

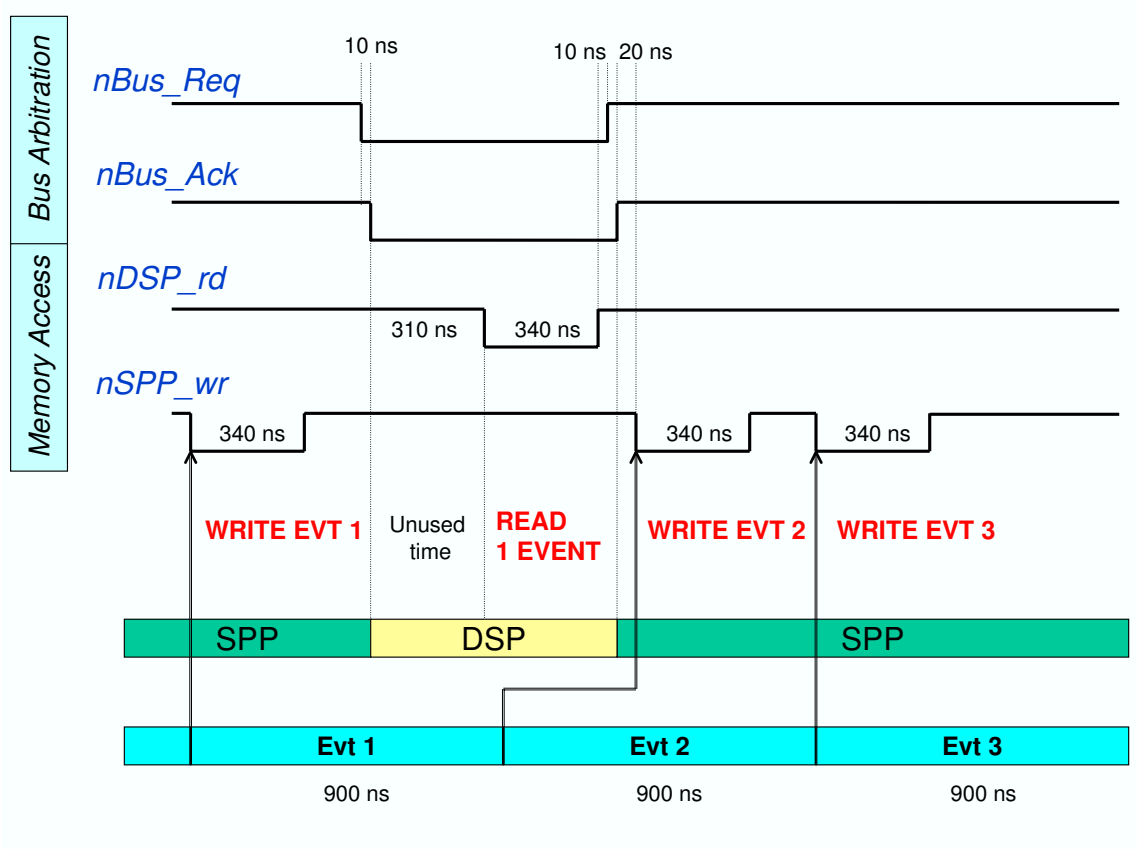



Figure 4.8: *The handshake mechanism. The DSP asks for the bus asserting the nBus_Req signal low. The SPP releases the bus and asserts low nBus_Ack. When nSPP_wr is low, the SPP is writing one event to L1B, when nDSP_rd is low the DSP is reading one event. The unused time is due to the penalties (minimum 100 ns) the DSP suffers to recognize or to assert a value on an I/O pin. We can easily recover from this additional time (about 100 ns) in the next 900 ns*

### 4.4.3 Bus arbitration

The strict timing requirements could only be satisfied by allowing the FPGA to be master of the bus, while the DSP acts as slave. Thus the L1 buffer is directly connected to the SPP, and bus switches isolates it from the DSP. In normal conditions, the switches are open and the FPGA can access the memory.

When the DSP needs to read an event from the memory (i.e. when a L1 accept arrives) it requests the bus from the SPP. If the FPGA is not using it (i.e. to write out one event), the SPP closes the switches, and notifies the DSP that the bus is available. When the event transfer is finished, the SPP opens the switches again and retakes control of the bus.

In figure 4.8 we show how we can achieve the required minimum event spacing at input (900 ns). At 100 MHz (1 clock cycle = 10 ns), it takes 340 ns for the FPGA to write out one event (one event is made of 34 words, 2 header 32 data words, see later), which will also be the maximum delay suffered by the DSP in receiving the bus. This leaves 560 ns per event for the DSP to access the buffer (340 ns to read out, while 310 ns are needed for the handshake).

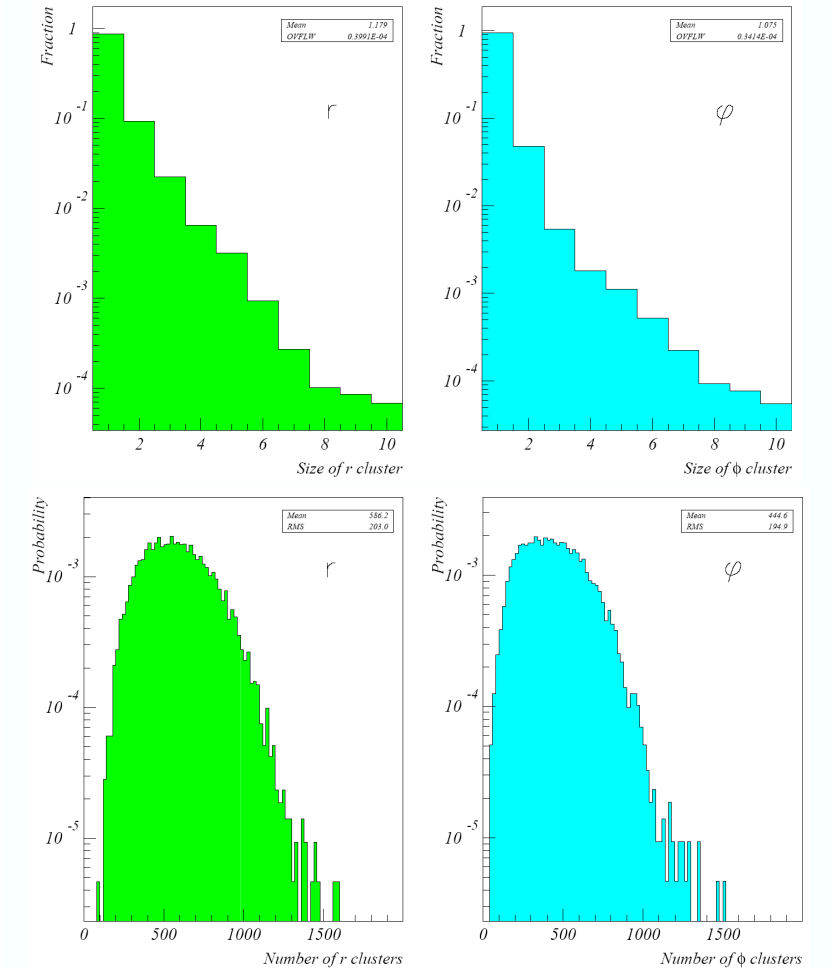



Figure 4.9: *The top plots show the cluster size probability for $r$ (left) and $\phi$ (right) sensors, while the bottom plots show the distribution of the number of clusters for $r$ (left) and $\phi$ (right) sensors in minimum bias events. Picture from [77].*

### 4.4.4 The clusterization

While the common mode suppression algorithm has been kept as close as possible to the FPGA version for L1 trigger preprocessing, the clusterization scheme is different and worthy to be discussed[6]. In fact only the cluster position and value of the strips forming it is transmitted to the L1 trigger, while we want to be able want to transmit to the HLT also the value of the 4 neighboring strips.

In general, we define a cluster as formed by one or more subsequent strips where a hit was detected. The hits distribution is given by [77]:

- 91% of the clusters formed by 1 strip;
- 7% of the clusters formed by 2 strips;
- 2% of the clusters formed by more than 2 hits;

[6]The current implementation of the clusterization scheme can be found in [82]

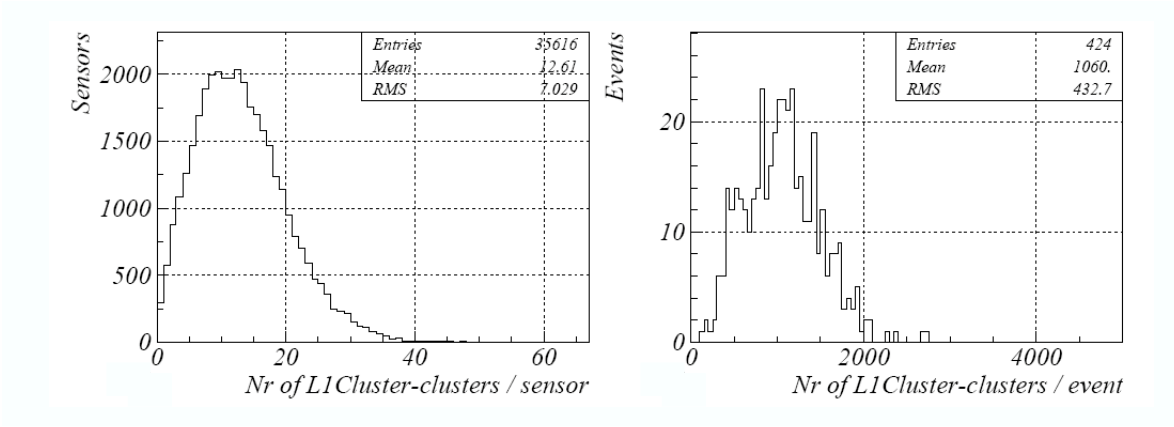



Figure 4.10: *Number of L1 clusters per sensor (left) and per event (right). The data sample corresponds to 424 L0 accepted minimum bias events. Plots from [83].*

Clusters formed for the L1 trigger are formed by 1 or 2 strips. For simplicity's sake only single hit clusters are considered in the HLT preprocessing. It can be shown that 2 hits cluster can be easily added at no bandwidth cost.

Supposing then that each hit is a cluster, a simple encoding scheme that allows to transmit the hit position (7-bit strip number) and the value of 4 adjacent strips is (3 16-bit words per cluster are needed):

| ... | ... |
|---|---|
| Strip Value (8) | 0 & Center Strip position (7) |
| Center Strip Value (8) | Strip Value (8) |
| Strip Value (8) | Strip Value (8) |
| ... | ... |

Therefore with this scheme, to encode 100 clusters (91 + 7x2+ 2x3)x3 = 333 words are needed (we assumed the cited hits distribution, and that clusters with more than 2 hits are actually 3 hits clusters).

To treat separately the 2 hits cluster, just one more 16-bit word is needed, to hold the value of the second hit strip. The information that it is a 2 hits cluster can fit into the first cluster word, since just 7 bits are needed to identify the strip position. The 8th bit could then be used to distinguish between 1 or 2 hits clusters. In this case the bandwidth needed for 100 clusters would be of (91x3 + 7x4 + 2x(3+4))= 315 words.

## 4.5 RB3 and DAQ_DSP tests

The L1 Buffer tests have been conducted in our Lausanne lab, where we had two RB3 boards, for the DSP and analog transmission lines tests [84]. The setup comprises also a Beetle chip, with a charge injection system to simulate charge collection.

However in order to control the input stage, data coming from the FADC have not been used in the DSP tests. A data generator has been instead implemented into the SPP

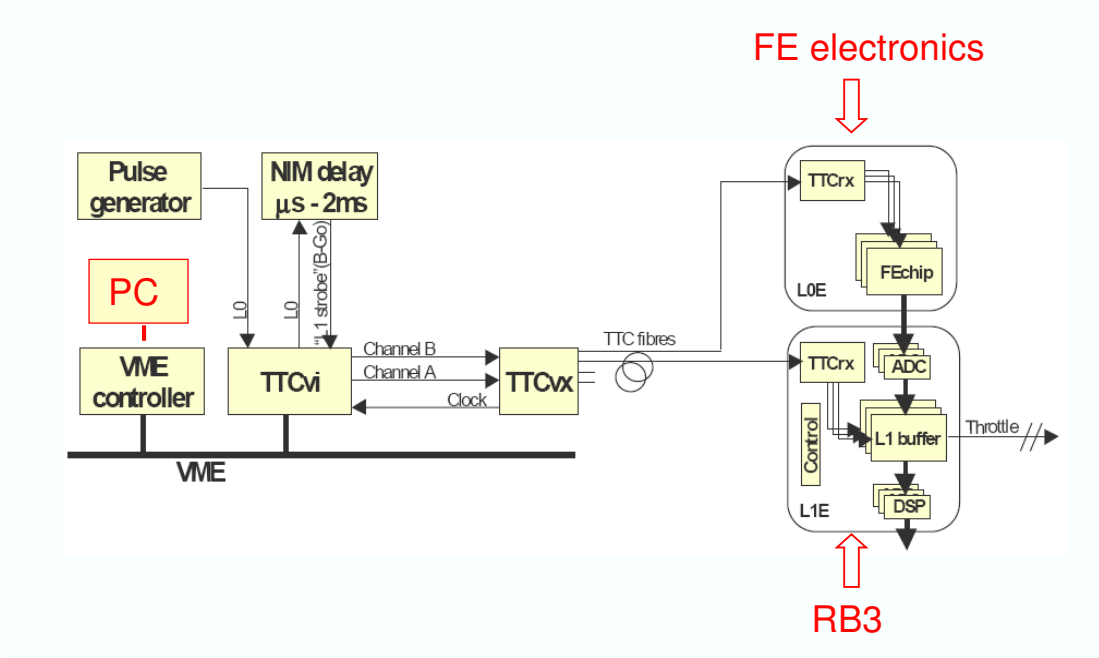



Figure 4.11: *Test bench setup to test the FE and L1 electronics with standards TTC components. Figure from [86].*

FPGA, which allowed us to check that the data processing and transfer had been correct at the output. The data generator can work in a single (used for debugging) or continuous event mode. In the last mode it outputs one event every 900 ns. The generated events contained one L1 cluster per FE chip. This is a conservative choice: the average number of L1 clusters per sensor (thus for 16 FE chips) has been found to be about 12 (see plots in fig. 4.10)[83].

The ECS interface has been replaced by a simple I2C interface. A mezzanine card from DevaSys [85], allows I2C commands to be sent from a PC (via the USB port). From the same PC the DSP could be debugged via a JTAG interface. Through the same interface the DSP boot code could be downloaded on the Flash ROM.

The TFC interface has been realized implementing the setup described in [86]. Before the Readout Supervisor (see chapter 3 for a short description of the RS) becomes available, in fact, a series of modules have been developed in order to reproduce a TFC environment. A scheme of the setup is found in fig. 4.11. Clocks, triggers and resets are generated into a module called TTCvi [53], which can be controlled by a PC via a VME interface. TTC commands are then encoded by the TTCvx, and sent via optical fibers to the TTCrx chips on the FE and L1 electronics. The TTCvi has been configured to generate random L1 accepts, with an average spacing of 25 $\mu$s.

The HLT interface has been realized with a PC equipped with an S-Link receiver card [87], thus allowing output data to be checked and compared with the input stage.

### 4.5.1 Test results

The VHDL implementation of the data generator and of the memory controller needed to output raw data to the L1 buffer at 100 MHz was straightforward. More time demanding

has been the DSP programming. Critical parts in the dataflow have been the reception of L1 accepts by the DSP, with a reasonable rate and no loss, and the consecutive readout of the L1B. We successfully tested the process sending continuously 64k L1 accepts. The LCMS algorithm implementation has also been carefully studied and we finally achieved a benchmark performance of 1960 clock cycles (12.25 $\mu$s @160 MHz.) for 128 detector channels (corresponding to one FE chip). For clusterization and formatting an additional overhead of 8 $\mu$s have to be added.

### 4.5.2 DSP Software development

The 6211 DSP can be programmed either in C or Assembler. A first series of tests showed that, if the C code is appropriately written and the compiler correctly configured, even critical parts of code can be implemented in C. Hence to ensure better readability and to facilitate code reuse, efforts were made in writing efficient C code and avoiding the use of Assembler as much as possible.

TI also provides a Built-in Operating System (BIOS), especially designed to help developers to implement embedded real-time software. DSP/BIOS provides a small firmware real-time library, and tools for real-time tracing and analysis [88]. The BIOS is object-oriented, and makes the use of all available peripherals quite easier, allowing the programmer to address them as objects dynamically created in memory. Nevertheless, even if the library is optimized to require a small number of instruction cycles, with even a significant portion implemented in assembly language, the simple overhead of accessing a structure was found to be too high for some timing-demanding parts of the code. In those cases a direct access to the DSP registers that control the peripherals has been preferred.

The dataflow on the DAQ_DSP daughterboard, and all subtilities used in programming the DSP are described in details in the appendix 4.C.

### 4.5.3 L1 electronics requirements

L1 requirements have been constantly changing over the years, as more and more data were added to the L1 event, until they were finalized with the design of the TELL1 L1 requirements. In order to reach a conclusion for our L1 buffer tests, we decided to stick to the requirements described in [61] as of 2002.

With our implementation, we verified the following main points:

- L0 minimum event spacing at input: 900 ns;
- L1 buffer depth: 2048 events;
- Nominal L1 trigger rate 40 kHz;
- L1 derandomizer depth: 16 events;
- Average event spacing at output: 22.5 $\mu$s;
- Average zero-suppression time: 20 $\mu$s;
- Maximum event fragment size: 1 KB.

We also have the possibility of:

- Error detection;

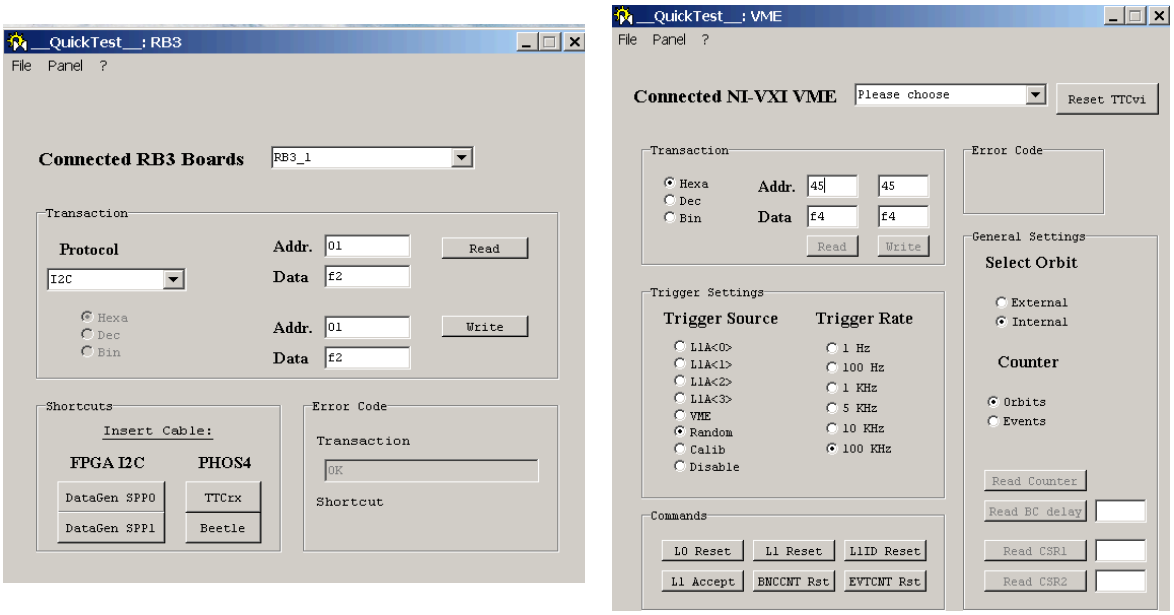



Figure 4.12: *The PVSS graphical interface implemented to control RB3 peripherals (through the I2C interface, on the left) and the TTC interface (through the VME bus, on the right).*

- Inclusion of event tags from the L1 buffer (error flags, L0-ID, L1-ID, B-ID, trigger type);
- Masking input sources;
- Overflow detection;
- Programmable zero-suppression parameters (pedestals, thresholds);
- Event size information available in header.

### 4.5.4 Other tests: Integration with the PVSS system

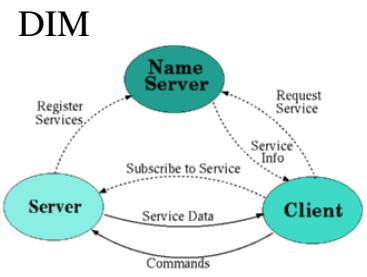



Figure 4.13: *The DIM protocol. Picture from [89].*

All LHC hardware (and online software as well) components have to be integrated into a highly distributed control system, which will be responsible of acquiring all subsystems data, use it for their supervision, monitor their behavior and perform the necessary operations of initialization, configuration, and operation [90]. To accomplish all these tasks CERN has chosen a industrial SCADA[7] package: PVSS.

PVSS provides for very large applications the control of thousands of hardware devices. In the case one PVSS would not been enough, several PVSS instances can be run in a distributed environment. Nevertheless, PVSS allows the various components to be run stand-alone. For development and debugging the

[7]SCADA systems are widely used for Supervisory Control And Data Acquisition of industrial processes. At CERN they have already been used by L3 muon detector and NA48.

control system can be partitioned, and the concurrent operation of the various pieces is possible.

To access the different hardware devices a DIM (Distributed Information Management) protocol has been developed at CERN, and integrated with PVSS [89]. DIM is based on a client/server architecture, and its main concept is that of service. Services are provided by DIM server, and are set of data (of any type or size).

DIM provides the interface between PVSS and the hardware device drivers in the sense that a DIM server publishes as services the driver functionalities, and PVSS accesses them through the integrated DIM client. A Domain Name Server (DNS), which publishes information about the available DIM servers and services, is used for transparency and allows easy crashes recovery or servers migration.

Two DIM servers and a PVSS interface have been developed, to allow the remote control of RB3 and the TTC interface. The first server allows the user to set and write RB3 registers through the I2C interface, while the second one can be used to send TTC commands as resets or triggers through the VME interface.

## 4.6 Conclusions

A DSP-FPGA shared memory bus implementation for the L1 buffer has been presented. It has been tested with RB3, the last prototype of the TELL1 board, and shown to satisfy L1 electronics requirements at the time of its development (2002). However the DSP technology has been abandoned in the design of TELL1. An SRAM implementation of the L1 buffer is no longer possible due to the increased L1 latency (52.4 ms) and buffer size (58254 events deep). To cope with this, DDR SDRAM are used on the TELL1 board. Support for the DDR SDRAM technology was initially not foreseen for the DSPs. Besides this limitation, many of the problems encountered during this study were already driving the final technology choice towards FPGAs.

Advantages of a DSP architecture were the lower cost and the built-in instructions that make the LCMS algorithm implementation rather straightforward [73]. However, recent developments in FPGA technology led to the inclusion of large on-chip memory and embedded multiply accumulate blocks [91]. Moreover, while design requirements were easily met by the FPGAs on RB3, DSP programming required quite a lot of efforts. DSPs are designed for tasks that range between 2 $\mu s$ to several ms. execution time [88]. The requirement of running the HLT preprocessing algorithm at 40 kHz is really in the high end of DSP target applications. Therefore most of DSP/BIOS facilities in thread scheduling cannot be used, thus resulting in additional complexity and development time. Also the design of a board with both FPGAs and DSPs (16 were needed!) would require additional effort, since one has to master (and afterwards maintain) both technologies.

The hybrid DSP-FPGA solution has then been dropped in favor of a FPGA only architecture, which assures more flexibility and higher system integration. Nevertheless, successful tests of RB3, and integration with PVSS and the TTC components have been conducted, which proved to be very helpful for the design of the TELL1 board.

Another remarkable result of the RB3 tests with different mezzanine cards was the migration of three FPGAs (the FSC, the L1T and the DAQ) into one combined chip. This was driven by the necessity of tight connections and access to full TTC information in all stages. This choice has been crucial for the migration from the old to the new readout scheme.

### The present: the TELL1 board

The final L1 board has to satisfy the needs of most of the LHCb subsystems, not only of the VELO. Therefore it accepts as input either 24 optical links running at 1.6 GHz, or 64 analogue links, sampled by 10-bit FADC at 40 MHz. The output toward the L1T and HLT is provided by four Gigabit Ethernet links. Both L1T and HLT preprocessing are performed by the on-board FPGAs. The TELL1 board is equipped with 256 Mbit DDR SDRAM. They are operated at a frequency of 120 MHz to achieve a data transfer rate of 240 MHz [76].

### And the DSPs?

The 62xx family is now the low-cost solution for TI DSPs (as low as 9 USD/chip!). The maximum available clock frequency is 300 MHz. As of today, chips from the 64xx series are in the same price range as the FPGAs used on the TELL1 board ($\sim$300 USD). They feature clock frequencies up to 1 GHz, support DDR 2 500 SDRAM technologies (data transfer rate of 1 GHz), and have, among the others, Gigabit Ethernet, PCI, and even $I^2C$ interfaces. One can therefore suppose that a DSP solution for TELL1 would still be feasible nowadays (an in-depth study would of course be necessary before drawing any conclusion). However the problems that arose during the tests described in this chapter still remain. DSPs are not as versatile as FPGAs, therefore changes in the specifications are likely not to be painless. Moreover, the additional know-how necessary to maintain and develop both DSP and FPGA technology is a too heavy burden in terms of time and manpower for such a small design as TELL1.

# Appendix to Chapter 4

## 4.A RB3 architecture

To allow the testing of various solution for the final TELL1 board, most of RB3 tasks are actually accomplished by mezzanine cards. A picture of RB3 can be found in fig. 4.14, where the main blocks can be recognized. A short description of each part is given below (more information can be found in [65]):

**Input** Four FADC Receiver (RX) cards receive the analog data coming from the FE chips. Each card receives data coming from one Beetle. Analog data are digitized at a rate of 40 MHz and with 8 bit precision.

**Front-End eMulator (FEM)** A daughter card equipped with a Beetle chip is used to reproduce the behavior of the front-end chip concerning the readout timing. It reproduces counters used for event identification, such as event, bunch, and pipeline column number counters [92].

**FPGA**

- The **FSC** (Fast Synchronization and Control) FPGA interprets TTC commands[8], distributes L1 and L0 accepts and issues resets for the other FPGAs. It also provides the interface to the FEM, decodes the necessary information for data synchronization and error checking, and sends them to the SPP FPGAs.
- Four **SPP** (Synchronization and L1 Pre Processor) FPGAs receive raw digitized data. They are responsible for their synchronization to RB3 clock domain and error checking using FEM-generated event identification counters. SPPs also perform L1T preprocessing, and sends L1T clusters to the L1T_Link FPGA. On the other hand, they write raw data to the L1 buffer, where they are kept during L1 latency.
- The **L1T_Link** FPGA collects data coming from SPP FPGAs and sends them to the L1 trigger through a S-link Tx (transmitter) mezzanine card.
- The **DAQ_Link** FPGA collects data coming from DSPs and sends them to HLT through a S-link Tx mezzanine card.

**Output** Two S-link mezzanine cards [87] provide the interface to L1T and HLT.

**Interface to LHC TFC system** A mezzanine card (TTCrm), equipped with a TTCrx chip, receives the 40 MHz LHC clock, the L0 and L1 decisions, and the resets from the TTC system [93], and makes them available to RB3 chips.

**Interface to LHCb ECS** A mezzanine card should have provided link to the ECS control system. Since this card never became available, a simple I2C interface[9] was used. It allows the slow control of the board, through registers on the FPGAs the user can write and read. It is also used to configure the Beetle chip on the FEM.

[8] The Timing, Trigger and Control (TTC) system is common to all LHC experiments, and it is responsible for fast controlling and clock distribution [53]. See also section 3.3.

[9] I2C is a serial communication protocol specified by Philips Semiconductors [94]

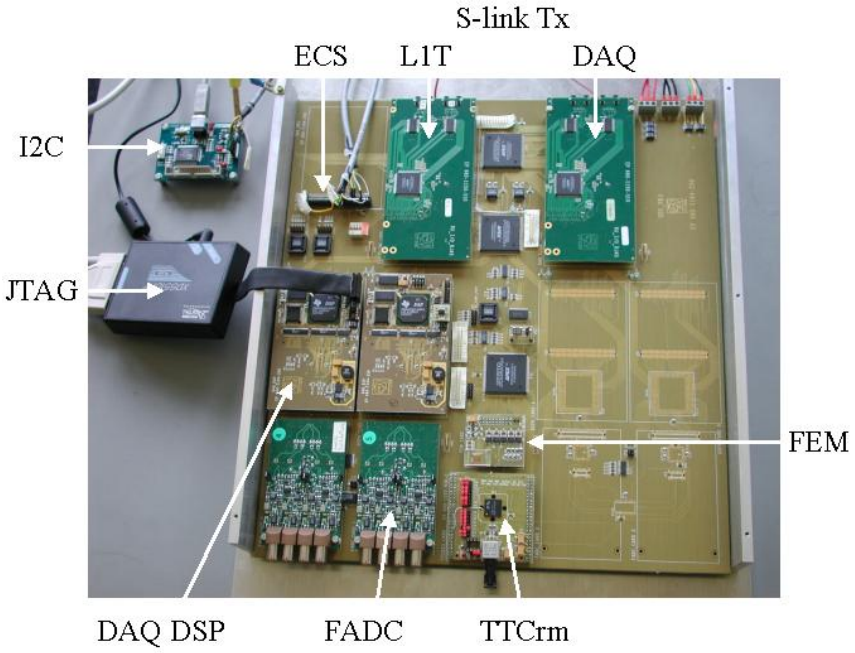



Figure 4.14: *A picture of RB3. One can recognize several mezzanine cards: The FADC, FEM, S-Link, TTCrm, and the DAQ_DSP. The JTAG interface used to access the DSP is also visible. The ECS mezzanine card is not present. At its place, a simple I2C interface is realized, with the aid of a little external card by DevaSys, controlled by a host PC [85]. See text for explanation.*

**Interface to the L1 Buffer** Two connectors allow the use of different daughter boards to test various solutions. The daughter board must then host a memory implementation of the buffer, and a microprocessor responsible for HLT preprocessing and for transmitting HLT clusters to the DAQ_Link FPGA. The tests described here have been done using a mezzanine card with a DSP chip (DAQ_DSP). Another mezzanine board employing an FPGA chip has also been tested [95], to gain experience with the FPGA technology and to guide the FPGA choices for the final board [76].

### 4.A.1 RB3 dataflow

Data coming from the FADCs are going directly into the SPP FPGA. Here synchronization and error checking are performed, using information coming from FSC [65, 92]. Then the data flow is split (see fig. 4.15).

Raw data going to the L1 trigger are zero suppressed and sent from the SPP to the L1T_Link FPGA, where they are finally encoded and transmitted to the L1T over a S-Link connection. On the other hand, raw data going to the DAQ are written out to the L1 Buffer.

Only L1 accepted events will be read out by the DSP, zero-suppressed and sent to DAQ_Link FPGA. From this chip, they are finally sent out to the HLT through the second S-link mezzanine board.

A more detailed description of RB3 functionalities can be found in [65, 92].

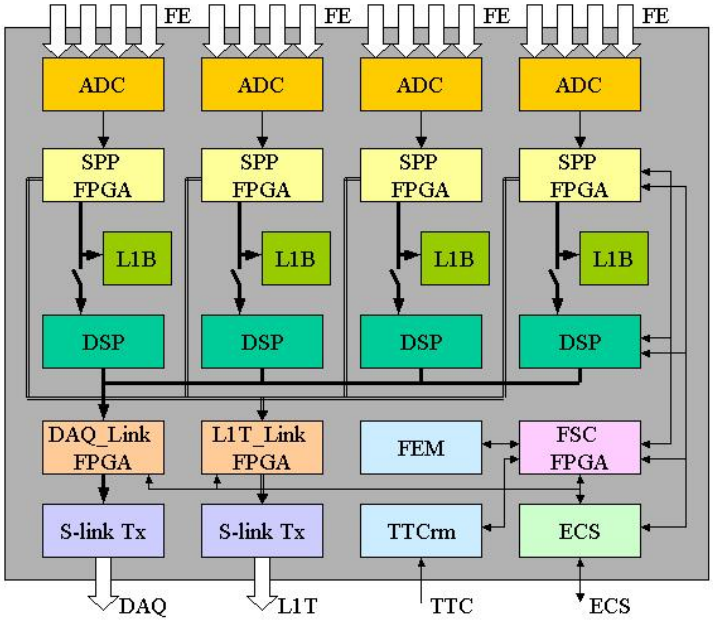



Figure 4.15: *RB3 Block diagram and dataflow. This chapter will focus on the data path from L1B to DAQ (marked with thick solid lines in the picture).*

## 4.B The DAQ_DSP mezzanine board

Finally the DAQ_DSP board has been equipped with a TI 6211 DSP and SBSRAM for the L1 buffer. The SBSRAM can store 128k words of 32 bits, and the supported clock frequency is 100 MHz. The other components of the mezzanine card are (see block diagram in figure 4.16):

**Flash ROM (512k x 8)** It contains the boot code for the DSP[10].

**Bidirectional switches** They connect the SBSRAM signals to both the SPP FPGA and the 6211 DSP. The switches direction is controlled by the SPP FPGA.

**PLL Clock Driver** It provides the 100 MHz clock to both the SBSRAM and the SPP.

**Emulator Connector** A JTAG[11] interface to a host PC, used to download test code into DSP and for debugging purposes.

### 4.B.1 TMS320C6211 Architecture

The TMS320C6211 core consists of 32 32-bit general-purpose registers and eight functional units: two multipliers and six Arithmetic Logic Units (ALU) [96]. Thus in principle

[10] A Read-Only Memory (ROM) is a special kind of memory where data are stored even when the power is turned off. They can be programmed only a limited number of times.

[11] A standard written by the Joint Test Action Group (JTAG) for accessing and controlling the signal levels on the pins of a digital circuit. It also has some extensions for testing the internal circuitry of the chip itself, which is what is used here.

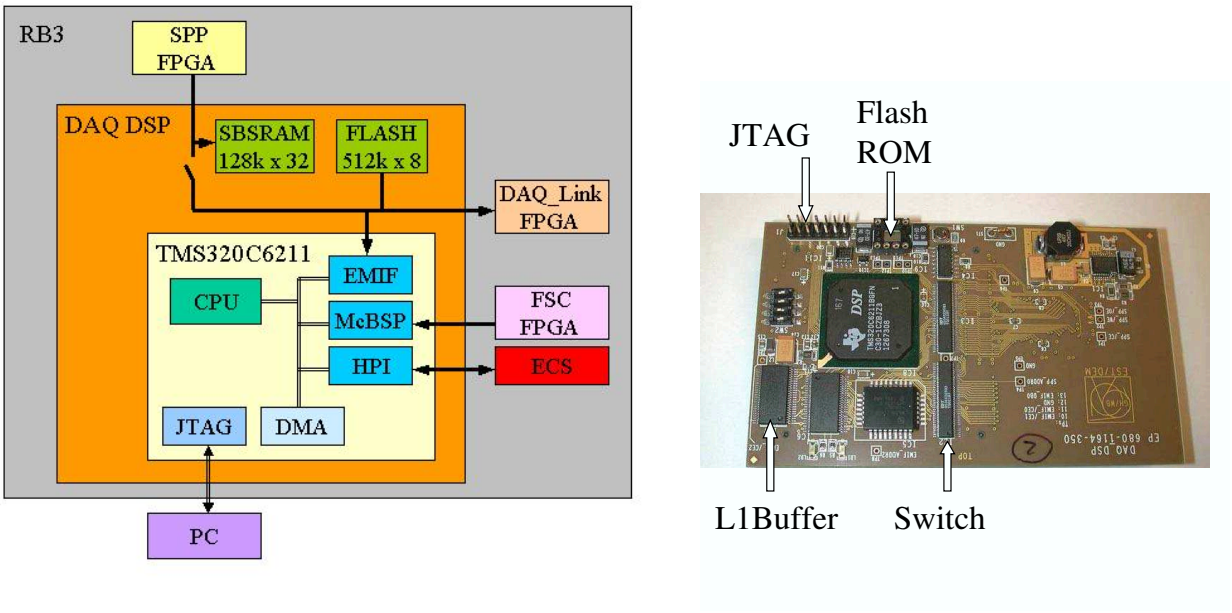



Figure 4.16: *A picture (right) and block diagram (left) of the DAQ_DSP mezzanine card.*

the 6211 can execute up to eight 32-bit instructions per cycle, if correctly programmed and if the various operations can be split across the different functional units. Moreover the registers and functional units are split into two groups, which allows the parallel execution of two different data paths (see figure 4.17).

Available peripherals on the 6211 DSP are [97]:

**Internal memory** A 64K IRAM (Internal Random Access Memory) is available and can be configured as program memory or as 2-level cache.

**Direct memory access (DMA)** An EDMA (Enhanced DMA) controller transfers data between address ranges in the memory map without intervention by the CPU. It has 16 programmable channels, that can also be linked.

**External Memory InterFace (EMIF)** It provides glueless interface to various types of external memory (SDRAM, SBSRAM, SRAM, ASRAM, see section 4.4.1 for definition of the available memory types).

**Parallel port** A Host Port Interface (HPI) allows a host (master) to directly access the DSP's memory space (external, internal and memory-mapped peripherals). It can be used for DSP debugging.

**Serial port** A MultiChannel Buffered Serial Port(McBSP) is present. It can buffer serial samples in memory automatically with the aid of the EDMA controller.

**Timers** Two general-purpose 32-bit timers are available. They can also be used as general I/O.

**Clock** A PLL[12] (Phase Lock Loop) generates the DSP internal clock and the EMIF clock.

[12]An electronic circuit that controls an oscillator so that it maintains a constant phase (i.e. lock) on the

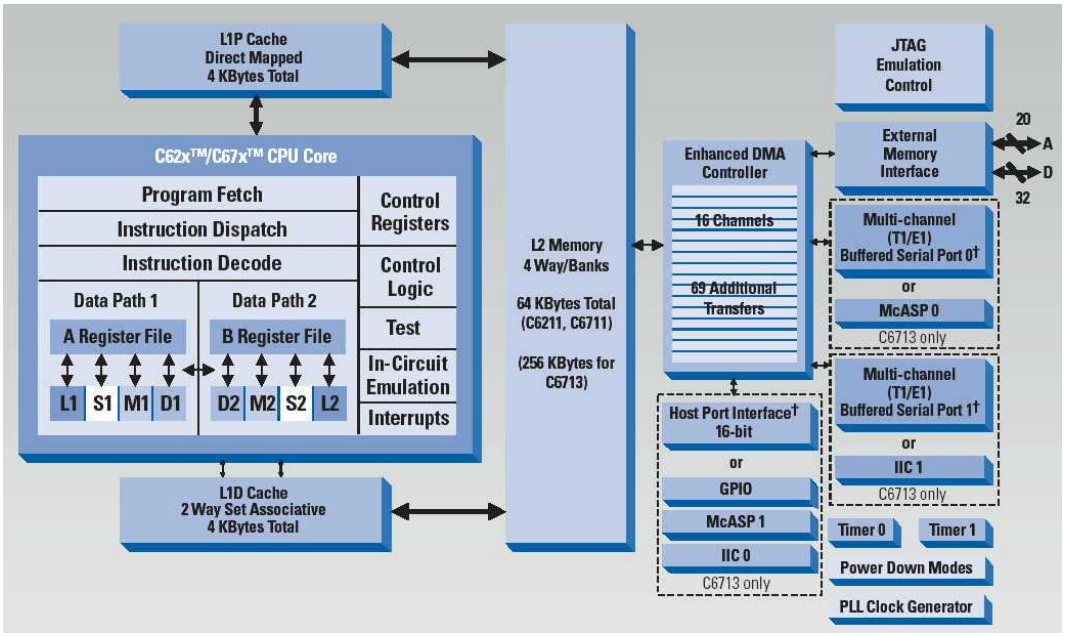



Figure 4.17: *TMS320C6211 DSP Block Diagram.*

## 4.C HLT Dataflow

The dataflow on RB3 has already been described in section 4.A.1. For what concerns the DAQ_DSP mezzanine card, the L1 buffer is filled at L0 accept rate. When a L1 accept arrives from the TTC system, it is decoded by the FSC FPGA, and immediately sent to the DSP. A simple handshaking mechanism has been implemented to allow the SPP and the 6211 to share the L1 buffer bus. Upon the reception of a L1 accept, the DSP reads the corresponding event from the buffer, performs the HLT preprocessing, and transmits the event fragment to the DAQ_Link FPGA, which collects data from all the DSPs, builds the HLT event fragment, and sends it out to the HLT.

### 4.C.1 The L1 Buffer

An event, as it is stored in the L1 buffer, is defined as a 2 32-bit words header, followed by 32 32-bit data words. The header contains information necessary for event identification[92]:

- 24-bit L0 event counter (EVENT CNT);
- 12-bit bunch counter (BUNCH CNT);
- 8-bit pipeline column number (PCN CNT);
- 4-bit synchronization error flags.

The event format has been chosen according to RB3 specification [65], and is given below (the header is shown in bold characters):

frequency of a reference signal. It assures that a certain signal is locked on a specific frequency.

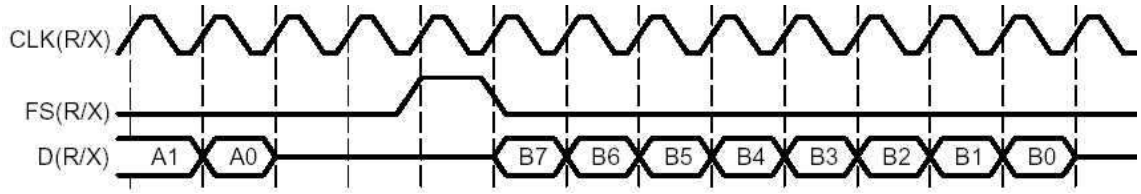



Figure 4.18: *Frame and clock operation as defined by the McBSP interface. It consists of a data path and a control path. Separate pins are used for transmission and reception Control information (clocking and frame synchronization) is communicated via four other pins. The serial clocks (CLKR and CLKX) define the boundaries between bits for receive and transmit, respectively. Similarly, the frame synchronization signals (FSR and FSX) define the beginning of an element transfer [97].*

| **ERROR FLAGS ORBIT CNT (7...0)** | **EVENT CNT (23...16) BUNCH CNT(11...8)** | **EVENT CNT (15...8) BUNCH CNT (7...0)** | **EVENT CNT (7...0) PCN CNT (7...0)** |
|---|---|---|---|
| RAW DATA(127) | RAW DATA(95) | RAW DATA(63) | RAW DATA(31) |
| ... | ... | ... | ... |
| RAW DATA(96) | RAW DATA(64) | RAW DATA(32) | RAW DATA(0) |

To simplify the L1 buffer address generation (which is easier if addresses are powers of 2), the buffer size has been chosen twice as big as required (1820 events deep). Hence 64 (instead of 36) 32-bit words can be reserved for each event. To span the address space (128k), 17 bits are necessary (the higher 11 bits are the base address of each event, while the last 6 bits span inside the event itself). To univocally determine the event address in the L1 buffer, the base address for each event has been chosen to be the 11 lower bits of the event counter.

### 4.C.2 The handshake protocol

The communication between the DSP and SPP (bus request and acknowledge) is accomplished exploiting the two timers pins available on the 6211 as general I/O. Unfortunately we found that the time needed for the DSP to read or assert a value on a pin is quite high (100 ns). We also tried to use the 6211 external interrupts to implement the handshake, but the penalties suffered in this case were even higher: it takes minimum 38 clock cycles = 238 ns@160 MHz for the DSP to service an interrupt.

### 4.C.3 Interface with the FSC FPGA

The L1 accept is received from the TFC system as broadcast command by the TTCrm on RB3, and interpreted by the FSC FPGA. The event identification counter is sent to the FSC FPGA by the FEM.

The event identification number (which univocally defines the event address in the L1 buffer, as we explained before) is communicated to the DSP as soon as a L1 positive decision arrives, through a serial link (via the DSP MCBSP port). The MCBSP protocol (shown in figure 4.18) had to be implemented on the FSC FPGA.

Received event counters are stored in a circular buffer implemented in the DSP internal memory. This exploits the capability of the MCBSP port of starting an EDMA transfer (i.e.

without the DSP intervention) upon data reception. EDMA transfers can be linked, in such a way that the next one will write to the next element of the circular buffer.

### 4.C.4 Data transfer from the L1 buffer

Several mechanisms have been tried in order to find the most efficient way to trigger the transfer of an event from the L1 buffer to the DSP internal memory, when a L1 accept is received. A critical part of the system is in fact being able of liberating the bus as soon as possible, in order to allow the continuous write out of L0 accepted events to the L1 buffer. While the simple solution would have been to service an interrupt sent to the DSP by the serial port, triggered by data reception, this again proved to be too slow.

Finally we chose a method called *flag polling*. Every 3 $\mu$s we check if an element in the event counter circular buffer has changed. If yes, the DSP asks for the bus and, once it receives it, starts a QDMA (Quick Direct Memory Access). A QDMA transfer is a sort of quick DMA transfer, with less functionalities, in the sense that it can only be started by the CPU and does not have linking capabilities, but is faster to submit, since it needs less registers to be set. This solution saves critical time, needed to prevent buffer overflows.

Events read out from the L1 buffer are written into the DSP IRAM, where a 16 events deep L1 derandomizer is implemented.

### 4.C.5 HLT zero suppression

The HLT zero suppression algorithm has already been described in section 4.3.1. Each DSP has to process 128 x 8 bit channels. In the FPGA implementation 4 channels are processed in parallel [77], but this is not allowed by the DSP architecture.

The maximum number of bits required by the operations of the LCMS algorithm is in fact 11 (used in mean values calculations). The 6211 registers are 32 bit wide, so they obviously cannot accomodate 11 x 4 = 44 bits. However a 2 channel version can be implemented (16 bits reserved for each channel). The DSP has built-in functions that allow to perform the sum or subtraction of the upper and lower halves of two 32-bit registers and return the result, all in one CPU instruction.

However these instructions cannot be executed by the two arithmetic units (as standard sums and subtractions), but only by dedicated logical units, which are unfortunately also used to retrieve and store data to memory. Therefore these units are often stuck during the algorithm execution, and no gain in performance is observed compared to a single channel version of the LCMS algorithm.

The benchmarks for the multichannel version are of 900 clock cycles against 470 for the single channel, thus not justifying the increased complexity of the code needed to use such special instructions. Both implementations has been verified to give exactly the same results as the VHDL version of the L1T zero-suppression algorithm.

### 4.C.6 Cluster encapsulation

Once clusters are formed, they are rearranged using the following scheme:

| Header |
|---|
| Cluster 1 |
| Cluster 2 |
| ... |
| Cluster n |

| Trig Type (4) | Data length (12) |
|---|---|
| Reserved (4) | BUNCH CNT (12) |
| EVENT CNT (23...16) | EVENT CNT (15...8) |
| Reserved (8) | EVENT CNT (7...0) |
| Error Flag (8) | PCN CNT (8) |

The header (in bold on the right) is formed by 5 16-bit words that contain information on the trigger type, error status, and event identification numbers as required by [61].

In order to keep the event size under control, the maximum number of cluster allowed per DSP (i.e. 128 channels) is 10, which corresponds to a fragment size of 35 words. If more than 10 clusters are found this is flagged in the fragment header, and the whole event (not the clusters) is sent to HLT, together with the hit mask (additional 8 words needed). In this case the fragment size would be of 77 words.

### 4.C.7 Interface to the DAQ_Link FPGA

Every 9 $\mu$s the EDMA transfers the event fragment to the DAQ_Link FPGA. The interface between the DSP and the FPGA is implemented as a 16-bit 256-word deep FIFO. Actually this is not supported by the EMIF, so the DSP is configured to see the FPGA as an asynchronous memory, and the necessary glue logic has been implemented into the DAQ_Link in order to fill a 8 event deep FIFO. With this implementation the time needed to transfer 1 16-bit word is 64 ns.

### 4.C.8 HLT interface

All event fragments are gathered in the DAQ_Link, and sent to the HLT over a S-Link connection [87]. The format of the output data is:

| Header |
|---|
| 0x00C0FFEE |
| Event Size |
| **Event Data** |
| DSP0 Event Fragment |
| DSP1 Event Fragment |
| DSP2 Event Fragment |
| DSP3 Event Fragment |
| **Trailer** |
| CRC |
| NOT(Event Size) |
| 0x00C0FFEE |

The header contains, as required in [61]:

- 4-bit L1 trigger type;
- 12-bit data length;
- 12-bit bunch counter;
- 24-bit event counter;

- 8-bit pipeline column number;
- 8-bit error flag.

The trailer contains control information (CRC[13] and event size) to check the transfer from RB3 to HLT.

[13]The Cyclic Redundancy Check (CRC) allows to detect small changes in a block of data, and is particularly suited to check transmission errors.

Part III

# Search for polarized radiative $\Lambda_b$ decays at LHCb

Chapter 5

# Phenomenology of polarized radiative $\Lambda_b$ decays

*This chapter describes the motivations for the study of radiative decays of $\Lambda_b$ hadrons. In particular, we want to probe the polarization of the emitted photon. Detailed calculations of decay amplitudes and angular distributions, which depend on the photon polarization, are carried out.*

## 5.1 Introduction

Polarized radiative $\Lambda_b$ decays are well suited for probing a large variety of new physics effects, while imposing at the same time important constraints on the Standard Model (SM) at the quantum level [98]. Even if the measured decay rate is in good agreement with the SM prediction, new physics may still be hidden in more subtle observables. One of the most promising is the polarization of the emitted photon, which is predicted to be mainly left-handed in the SM. An overview of the experimental methods which have been proposed to probe the photon polarization has been presented in section 2.5.

In this chapter, we especially focus on radiative $\Lambda_b$ decays of the type $\Lambda_b \to \Lambda(X)\gamma$, where $X$ is the mass of the $\Lambda$ baryon. These decays will in fact be produced in large quantities at the LHC, and could open a window of opportunity for LHCb to measure the photon polarization.

Besides their different mass, the $\Lambda$ baryons can be characterized by their spins and decay modes: the ground state $\Lambda(1115)$ has spin 1/2 and mainly decays weakly in $p\pi$ (64% of the times), while heavier $\Lambda$ decay strongly. The spin ranges from 1/2 to 9/2 for the heaviest known state, while the mass varies from 1405 to 2100 MeV. The first state above the $N\bar{K}$ threshold is the $\Lambda(1520)$. Status and various parameters of the $\Lambda$ resonances (above the $\Lambda(1115)$) are given for reference in table 5.1.

The full decay chain can be written as:

$$\Lambda_b \to (\Lambda(1115) \to p\ \pi)\gamma \qquad (a)$$

$$\Lambda_b \to (\Lambda(X) \to p\ K)\gamma \qquad (b)$$

Decay ($a$) has already been studied in the framework of Heavy Quark Effective Theory (HQET) [98, 99, 100]. A new observable, the angular asymmetry between the $\Lambda_b$ spin and the photon momentum, has been proposed. Its measurement, combined with the $\Lambda(1115) \to \mathrm{p}\pi$ decay polarization asymmetry, can be used to test the $V-A$ structure of the SM. However from the experimental point of view the $\Lambda(1115)$ reconstruction is quite delicate since it may traverse a large fraction of the experiment tracking system before decaying to $p\pi$. We will therefore study if decays of type ($b$) involving $\Lambda$ resonances, which decay strongly in $pK$, can be competitive, and if they can be used to improve the experimental sensitivity to the measurement of the photon polarization.

Table 5.1: *Status of the $\Lambda$ resonances. The first column contains the name of the state, then its quantum numbers in spectroscopic notation, the width of the resonance, the status, as explained below, and finally the branching fractions for the decay modes $N\overline{K}$ and $\Sigma\pi$. The status and the resonance parameters are estimations from the Particle Data Group [101].*

| Particle | $L_{I\cdot 2J}$ | $\Gamma$ [MeV] | Status | $N\overline{K}$ | $\Sigma\pi$ |
|---|---|---|---|---|---|
| $\Lambda(1405)$ | $S_{01}$ | 50 | **** | - | 100% |
| $\Lambda(1520)$ | $D_{03}$ | 15.6 | **** | 45% | 42% |
| $\Lambda(1600)$ | $P_{01}$ | $\approx 150$ | *** | 15–30% | 10–60% |
| $\Lambda(1670)$ | $S_{01}$ | $\approx 35$ | **** | 20–30% | 25–55% |
| $\Lambda(1690)$ | $D_{03}$ | $\approx 60$ | **** | 20–30% | 20–40% |
| $\Lambda(1800)$ | $S_{01}$ | $\approx 300$ | *** | 25–40% | seen |
| $\Lambda(1810)$ | $P_{01}$ | $\approx 150$ | *** | 20–50% | 10–40% |
| $\Lambda(1820)$ | $F_{05}$ | $\approx 80$ | **** | 55–65% | 8–14% |
| $\Lambda(1830)$ | $D_{05}$ | $\approx 95$ | **** | 3–10% | 35–75% |
| $\Lambda(1890)$ | $P_{03}$ | $\approx 100$ | **** | 20–35% | 3–10% |
| $\Lambda(2000)$ | ??? | ??? | * | ??? | ??? |
| $\Lambda(2020)$ | $F_{07}$ | ??? | * | ??? | ??? |
| $\Lambda(2100)$ | $G_{07}$ | $\approx 200$ | **** | 25–35% | 5% |
| $\Lambda(2110)$ | $F_{05}$ | $\approx 200$ | *** | 5–25% | 10–40% |
| $\Lambda(2325)$ | $D_{03}$ | $\approx 170$ | * | ??? | ??? |
| $\Lambda(2350)$ | $H_{09}$ | $\approx 150$ | *** | $\sim 12\%$ | $\sim 10\%$ |

| | |
|---|---|
| **** | Existence is certain, and properties are at least fairly well explored. |
| *** | Existence ranges from very likely to certain, but further confirmation is desirable and/or quantum numbers, BR, *etc.* are not very well determined |
| ** | Evidence of existence is fair. |
| * | Evidence of existence is poor. |

## 5.2 Theoretical framework

The decay $\Lambda_b \to \Lambda(X)\gamma$ corresponds at the quark level to the electromagnetic penguin $b \to s\gamma$ (see picture 5.1). Long distance contributions, such as $W$ or intermediate meson exchange, have been found to be negligible [99]. In the framework of Heavy Quark Effective Theory (HQET) one can write the effective Hamiltonian at Leading Order (LO) in $\alpha_s$

as[1]:

$$\mathcal{H}_{\text{eff}} = -4\frac{G_F}{\sqrt{2}}V_{ts}^*V_{tb}(C_7Q_7 + C_7'Q_7') \tag{5.1}$$

where $G_F$ is the Fermi constant, $C_7$ and $C_7'$ are the relevant Wilson coefficients, and the electromagnetic dipole operators take the form:

$$Q_7 = \frac{e}{16\pi^2}m_b\bar{s}\sigma_{\mu\nu}(1+\gamma_5)bF^{\mu\nu}, \quad Q_7' = \frac{e}{16\pi^2}m_b\bar{s}\sigma_{\mu\nu}(1-\gamma_5)bF^{\mu\nu}$$

which contain the right- and left-handed projectors $P_R, P_L = \frac{1}{2}(1 \pm \gamma_5)$.

The ratio of the Wilson coefficients gives the relative strength of the opposite chirality dipole operators and is normally defined as $r = \frac{C_7'}{C_7}$. In the SM $r$ is given by the ratio of the masses of the $s$ and $b$ quarks, $r = \frac{m_s}{m_b}$, hence it is expected to be small, and the photon emitted in $b \to s$ transitions predominantly left-handed.

This argument holds as long as $b \to s\gamma$ is a two-body decay, however it cannot be applied to multi-body final states such as $b \to s\gamma$ + gluons. Once QCD corrections are properly included, more operators may contribute to the effective Hamiltonian, and right-handed components contribution to the photon polarization may not be negligible [33]. Unfortunately no explicit calculations exist for $\Lambda_b$ radiative decays.

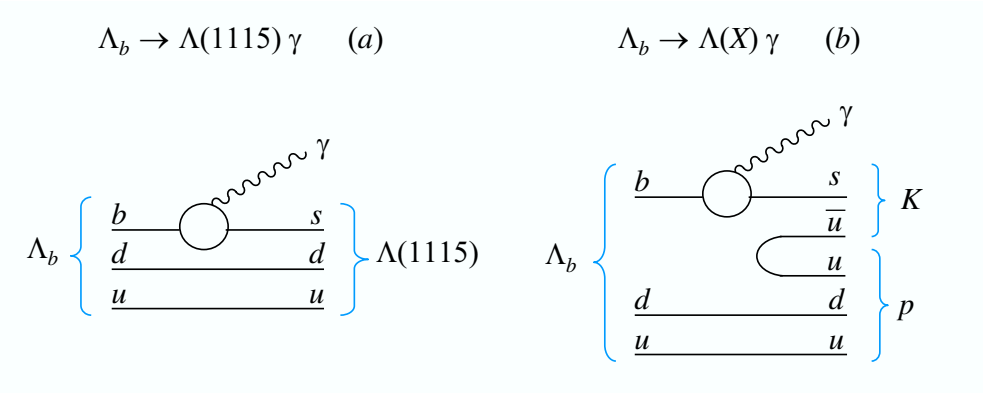



Figure 5.1: *Feynman diagrams for the two decays:* $\Lambda_b \to (\Lambda(1115) \to p\pi)\gamma$ $(a)$, $\Lambda_b \to (\Lambda(X) \to pK)\gamma$ $(b)$. *In both cases the relevant element is the electromagnetic penguin* $b \to s\gamma$.

### 5.2.1 CP violating effects

At Next-to-Leading Order (NLO) in $\alpha_s$ the effective Hamiltonian for the penguin $b \to s\gamma$ becomes:

$$\mathcal{H}_{\text{eff}} = -4\frac{G_F}{\sqrt{2}}V_{ts}^*V_{tb}(DQ_7 + D'Q_7') \tag{5.2}$$

where the dipole operators are now mediated by a linear combination of Wilson coefficients:

$$D = C_7^{(0)} + \frac{\alpha_s}{4\pi}(C_7^{(1)} + C_2^{(0)}k_2 + C_8^{(0)}k_8)$$

[1]The contents of this section are inspired by the theoretical work of [98, 99, 100]. A short introduction on how to treat hadronic decays within the SM has been given in 2.4.

$$D' = C_7'^{(0)} + \frac{\alpha_s}{4\pi}(C_7'^{(1)} + C_8'^{(0)} k_8)$$

Direct CP violation can arise at NLO[2], and will thus generate an asymmetry in the decay rate of $\Lambda_b \to \Lambda\gamma$ and its conjugate counterpart:

$$a_{\rm CP} = \frac{\Gamma - \overline{\Gamma}}{\Gamma + \overline{\Gamma}}$$

The SM predicts this asymmetry to be of the order of 1%, while many extensions foresee a sizable CP violation of the order of 10%, as in the decays $B \to X_s\gamma$.

### 5.2.2 Branching ratios

The Branching Ratios (BR) for the various $\Lambda_b \to \Lambda(X)\gamma$ decays can be derived from the formula [98]:

$$\mathcal{BR}(\Lambda_b \to \Lambda\gamma) = \tau(\Lambda_b)|C_7|^2(1+|r|^2)\frac{\alpha G_F^2 |V_{tb}V_{ts}^*|^2}{32\pi^4} m_{\Lambda_b}^3 m_b^2 \left(1 - \frac{m_\Lambda^2}{m_{\Lambda_b}^2}\right)|F(0)|^2 \qquad (5.3)$$

where $F(0)$ is the relevant form factor, and can be estimated to be $\sim 0.5$ for all $\Lambda$ baryons [102]. The suppression of the BR due to the larger mass of higher resonances is given by the kinematical factor $1 - \frac{m_\Lambda^2}{m_{\Lambda_b}^2}$.

For the decay of the $\Lambda$ baryon we consider the $N\overline{K}$ branching fractions from table 5.1 (averages have been assumed for the resonances where a range of values was given). We assume the ratio of the branching fractions $\Lambda(X) \to pK^-$ and $\Lambda(X) \to n\overline{K}^0$ equal to 1 based on isospin coupling, and neglect additional suppression factors due to higher angular momentum barrier.

Using the SM estimations for the Wilson coefficients $C_7$ and $C_7'$, one obtains (excluding the $\Lambda(1405)$ which is below the $N\overline{K}$ threshold):

| Decay | $\mathcal{BR}$ $[10^{-5}]$ |
|---|---|
| $\Lambda_b \to (\Lambda(1115) \to p\pi)\gamma$ | 4.15 |
| $\Lambda_b \to (\Lambda(1520) \to pK)\gamma$ | 1.31 |
| $\Lambda_b \to (\Lambda(1600) \to pK)\gamma$ | 0.65 |
| $\Lambda_b \to (\Lambda(1670) \to pK)\gamma$ | 0.69 |
| $\Lambda_b \to (\Lambda(1690) \to pK)\gamma$ | 0.69 |
| $\Lambda_b \to (\Lambda(1800) \to pK)\gamma$ | 0.84 |
| $\Lambda_b \to (\Lambda(1810) \to pK)\gamma$ | 0.92 |
| $\Lambda_b \to (\Lambda(1820) \to pK)\gamma$ | 1.57 |
| $\Lambda_b \to (\Lambda(1830) \to pK)\gamma$ | 0.15 |
| $\Lambda_b \to (\Lambda(1890) \to pK)\gamma$ | 0.56 |
| $\Lambda_b \to (\Lambda(2100) \to pK)\gamma$ | 0.70 |
| $\Lambda_b \to (\Lambda(2110) \to pK)\gamma$ | 0.34 |
| $\Lambda_b \to (\Lambda(2350) \to pK)\gamma$ | 0.28 |

The BRs for all interesting decay channels lie in the range $10^{-5}$–$10^{-6}$.

[2]CP violation is allowed in the Wilson coefficients $C_7$ and $C_8$ :

$$\overline{D} = C_7^{(0)*} + \frac{\alpha_s}{4\pi}(C_7^{(1)*} + C_2^{(0)} k_2 + C_8^{(0)*} k_8)$$

$$\overline{D'} = C_7'^{(0)*} + \frac{\alpha_s}{4\pi}(C_7'^{(1)*} + C_8'^{(0)*} k_8)$$

## 5.3 The photon polarization

The aim of the study of polarized radiative $\Lambda_b$ decays is the measurement of the photon polarization:

$$\alpha_\gamma = \frac{P(\gamma_L) - P(\gamma_R)}{P(\gamma_L) + P(\gamma_R)}$$

where $P(\gamma_{L/R})$ represents the probability of producing a left/right-handed photon. At LO in $\alpha_s$ only $Q_7$ and $Q_7'$ contribute to the photon polarization:

$$\alpha_\gamma^{LO} = \frac{1 - |r|^2}{1 + |r|^2} \tag{5.4}$$

However we have seen that more operators can contribute to $\alpha_\gamma$, if QCD corrections are included, or CP violating effects are taken into account. In the following, to simplify the notation, we will not consider any NLO effect, therefore $\alpha_\gamma = \alpha_\gamma^{LO}$, but will keep in mind that this relationship may be more complicated. In particular we stress the fact that, if a deviation from the LO prediction for the photon polarization is measured, additional theoretical efforts are needed to see if it can still be accommodated in the SM, or if it could be a hint of new physics.

It has been shown that the photon polarization can be tested by measuring the proton angular distribution in the decay $\Lambda_b \to (\Lambda(1115) \to p\pi)\gamma$ [99]. If the initial $\Lambda_b$ is polarized, as it is predicted at the LHC (see section 7.2), the photon polarization can also be extracted from the photon angular distribution [98]. We will now extend this result to any decay of the type $\Lambda_b \to \Lambda(X)\gamma$ where $\Lambda(X)$ is a $\Lambda$ resonance of spin 1/2 or 3/2.

## 5.4 Angular observables for $\Lambda_b \to \Lambda(X)\gamma$

To work out the final states angular distributions for polarized radiative $\Lambda_b$ decays we employ the helicity formalism [103]. We give here a pedagogical approach to the formalism, and apply it to the study of decays involving a $\Lambda(X)$ resonance with spin 1/2 or 3/2 (which already include the first 8 $\Lambda$ baryons, as one can see from table 5.1). Detailed calculations of the decay amplitudes can be found in appendix 5.A.

The results are given in terms of the helicity amplitudes characteristic of each decay and of the initial $\Lambda_b$ polarization. In the first case we will retrieve the angular distributions given in [98]. The same framework can be used to study any $\Lambda_b \to \Lambda(X)\gamma$ decay in a general way. However, if the $\Lambda(X)$ spin is $> 3/2$, the number of the relevant helicity amplitudes is greater than the number of observables, therefore no indication on the photon polarization can be derived, unless new theoretical predictions become available.

### 5.4.1 Helicity formalism for $\Lambda_b \to \Lambda(X)\gamma$ decays

In the helicity formalism, the relevant quantum numbers are the spin of the particles involved, and the possible symmetries of the decay. Hence we start from the consideration that the decays $\Lambda_b \to (\Lambda(1115) \to p\pi)\gamma$ and $\Lambda_b \to (\Lambda(X) \to pK)\gamma$ can be treated as a single decay of the type $\Lambda_b \to (\Lambda(X) \to ph)\gamma$, since the pion and the kaon have both spin 0 (so that both helicities are equal to 0).

The difference between the two decays consists in the fact that the decay $\Lambda(1115) \to p\pi$ is parity violating, while the decay $\Lambda(X) \to pK$ conserves parity. Also cases with different spins of the $\Lambda$ baryon will be treated separately.

As a common framework, and referring to fig. 5.2, we can define:

- the $z$ axis: the arbitrarily defined spin quantization axis (which we shall take parallel to the $\Lambda_b$ spin);
- the $z'$ axis: the direction of the $\Lambda(X)$ momentum;
- the angles ($\theta_\Lambda$,$\phi_\Lambda$) and ($\theta_\gamma$,$\phi_\gamma$) of the $\Lambda(X)$ and photon momenta with respect to the $z$ axis, measured in the rest frame of the $\Lambda_b$;
- the angles ($\theta_p$,$\phi_p$) and ($\theta_h$,$\phi_h$) of the proton and the pion/kaon momenta with respect to the $z'$ axis, measured in the rest frame[3] of the $\Lambda(X)$.

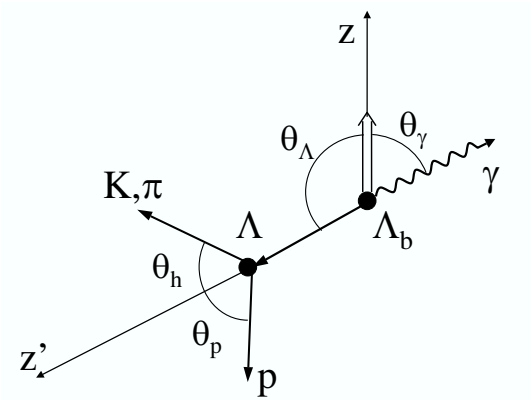



Figure 5.2: *Angles definition for the decay $\Lambda_b \to \Lambda(X)\gamma$. The angles $\theta_\Lambda$ and $\theta_\gamma$ are measured in the $\Lambda_b$ rest frame, while the angles $\theta_h$ and $\theta_p$ are measured in the $\Lambda(X)$ rest frame.*

Thus:

- the $\Lambda_b$ has angular momentum $J = 1/2$ and spin projection $M = \pm 1/2$ along the $z$ axis;
- the $\Lambda(X)$ has angular momentum $J_\Lambda$ and helicity $\lambda_\Lambda = M_\Lambda$, defined as its spin projection along $z'$;
- the final state particles have helicities $\lambda_\gamma$, $\lambda_p$ and $\lambda_h = 0$ (where $h$ is $\pi$ or $K$ according to the decay).

The amplitude probability can be written as:

$$A = \sum_{\lambda_\Lambda} D^{s_\Lambda *}_{\lambda_\Lambda,\lambda_p}(\phi_p,\theta_p,-\phi_p) D^{J*}_{M,\lambda_\Lambda-\lambda_\gamma}(\phi_\Lambda,\theta_\Lambda,-\phi_\Lambda) C_{\lambda_\Lambda,\lambda_\gamma} E_{\lambda_p} \tag{5.5}$$

where $s_\Lambda$ is the $\Lambda(X)$ spin and the quantities $C$ and $E$ are the helicity amplitudes of the two decays (respectively $\Lambda_b \to \Lambda(X)\gamma$ and $\Lambda(X) \to ph$). They are independent of the decay angles ($\theta_\Lambda, \phi_\Lambda, \theta_p, \phi_p$), and of the spin projections $M_\lambda$ and $M$.

For the strong decay $\Lambda(X) \to pK$ we can use parity to simplify eq. (5.5):

$$E_{\lambda_p} = \eta_\lambda \eta_p \eta_k (-1)^{J_\lambda - J_k - J_p} E_{-\lambda_p}$$

where $\eta$ and $J$ are respectively the parity and spin of the particles [104]. The relevant quantum numbers are $J^P(p) = 1/2^+$ and $J^P(K) = 0^-$, whereas the $\Lambda$ spin and parity can be found in table 5.1. According to the $\Lambda$ parity, we therefore obtain,

$$E_{\lambda_p} = -\eta_\lambda (-1)^{J_\lambda - \frac{1}{2}} E_{-\lambda_p} = \pm E_{-\lambda_p}$$

To write the decay probability we still need to take into account the $\Lambda_b$ polarization. We then introduce the polarization density matrix $\rho$:

$$\begin{pmatrix} \rho_{++} & \rho_{+-} \\ \rho_{-+} & \rho_{--} \end{pmatrix}$$

[3]We note that the azimuthal angles $\phi_i$ are the same in both rest frames (of the $\Lambda_b$ and $\Lambda(X)$).

where the index $+$ is related to the positive value of the spin projection $m = +1/2$ and the index $-$ indicates the negative one, $m = -1/2$; i.e. $\rho_{++}$=$\rho_{\frac{1}{2},\frac{1}{2}}$, etc.

It can be shown that if we are not interested in correlations between the production mechanism and the decays, the density matrix non-diagonal components are averaged out [105]:

$$\rho_{mm'} = \delta_{mm'}\rho_{mm'}$$

Since Tr$\rho = \rho_{++} + \rho_{--} = 1$ the $\Lambda_b$ polarization can be written as:

$$P_{\Lambda_b} = \rho_{++} - \rho_{--} \tag{5.6}$$

The decay probability finally becomes:

$$w = \sum_{M,\lambda_\gamma,\lambda_p} \rho_{MM}|A|^2 \tag{5.7}$$

where we summed over the final helicities since the experiment does not measure them. The sum over $\lambda_h$ has been dropped since $\lambda_h = 0$.

We will now give the results for resonances of spin 1/2 and 3/2. The detailed derivation can be found in App. 5.A.

### 5.4.2 $\Lambda(X)$ spin = 1/2

The decay probability takes the form:

$$w_{\frac{1}{2}} \propto 1 - \alpha_{p,1/2}P_{\Lambda_b}\cos\theta_p\cos\theta_\Lambda - \alpha_\gamma(\alpha_{p,1/2}\cos\theta_p - P_{\Lambda_b}\cos\theta_\Lambda) \tag{5.8}$$

where $\alpha_\gamma$ is the photon polarization and $\alpha_{p,1/2}$ is the proton asymmetry parameter as defined in appendix 5.A. For the ground state $\Lambda(1115)$, the weak decay parameter $\alpha_{p,1/2}$ is known to 2%, and its value is $0.642 \pm 0.013$ [101]. For heavier $\Lambda$ baryons the decay is parity conserving and $\alpha_{p,1/2} = 0$.

By integrating the decay probability, one obtains the following angular distributions for the final states:

$$\frac{d\Gamma}{d\cos\theta_\gamma} \propto 1 - \alpha_\gamma P_{\Lambda_b}\cos\theta_\gamma \tag{5.9}$$

$$\frac{d\Gamma}{d\cos\theta_p} \propto 1 - \alpha_\gamma\alpha_{p,1/2}\cos\theta_p \tag{5.10}$$

We indeed find the same results as in [98]. We have seen that the photon helicity asymmetry parameter $\alpha_\gamma$ can be related to the ratio $|r|$:

$$\alpha_\gamma = \frac{1-|r|^2}{1+|r|^2} \tag{5.11}$$

Thus, assuming the $\Lambda_b$ polarization to be known, one can probe the ratio $|r|$ by measuring the photon and proton angular distributions. The measurement of $|r|$ in two independent ways allows for good sensitivities even if the initial $\Lambda_b$ polarization is not very well measured. Otherwise combining the two measurements one can obtain the $\Lambda_b$ polarization, which could also be sensitive to physics beyond the SM. In fact if a discrepancy is found with the value measured in decays of the type $\Lambda_b \to \Lambda_c\ell\nu_\ell X$, non-standard right handed $b \to c$ currents could be present [98].

We remark that for $\Lambda(X)$ resonances that decay into $pK$, the proton angular distribution is flat, and the photon polarization can only be measured with the photon angular distribution.

### 5.4.3 $\Lambda(X)$ spin = 3/2

The decay probability can be written as:

$$w_{\frac{3}{2}} = \sum_{i=1}^{6} C_i(\phi_\Lambda, \phi_p) \cdot f_i(\theta_p) \cdot g_i(\theta_\Lambda, P_{\Lambda_b}) \tag{5.12}$$

where:

$C_i(\phi_\Lambda, \phi_p)$ are functions of the relevant helicity amplitudes and of the azimuthal angles $\phi_\Lambda$ and $\phi_p$. We remind that $|C_{\lambda_\Lambda,\lambda_\gamma}|^2$ represents the probability of producing a photon with helicity $\lambda_\gamma$, and a $\Lambda$ resonance with helicity $\lambda_\Lambda$;

$f_i(\theta_p)$ are functions of the proton polar angle $\theta_p$;

$g_i(\theta_\Lambda, P_{\Lambda_b})$ are functions depending on the $\Lambda$ polar angle $\theta_\Lambda$ and the $\Lambda_b$ polarization $P_{\Lambda_b}$.

The $C_i$, $f_i$ and $g_i$ functions are reported in table 5.2.

Table 5.2: *Summary of the terms that make up the decay probability* $w_{\frac{3}{2}} = \sum_i C_i \cdot f_i(\theta_p) \cdot g_i(\Lambda, P_{\Lambda_b})$*, in the case* $J_\Lambda = 3/2$*. For explanation see text.*

| $i$ | $C_i(\phi_\Lambda, \phi_p)$ | $f_i(\theta_p)$ | $g_i(\theta_\Lambda, P_{\Lambda_b})$ |
|---|---|---|---|
| 1 | $\lvert C_{\frac{3}{2},1}\rvert^2$ | $\frac{3}{8}\ \sin^2\theta_p$ | $1 + P_{\Lambda_b}\cos\theta_\Lambda$ |
| 2 | $\lvert C_{-\frac{3}{2},-1}\rvert^2$ | $\frac{3}{8}\ \sin^2\theta_p$ | $1 - P_{\Lambda_b}\cos\theta_\Lambda$ |
| 3 | $\lvert C_{\frac{1}{2},1}\rvert^2$ | $\frac{1}{8}\ (3\cos^2\theta_p + 1)$ | $1 - P_{\Lambda_b}\cos\theta_\Lambda$ |
| 4 | $\lvert C_{-\frac{1}{2},-1}\rvert^2$ | $\frac{1}{8}\ (3\cos^2\theta_p + 1)$ | $1 + P_{\Lambda_b}\cos\theta_\Lambda$ |
| 5 | $\mathrm{Re}\{C^*_{\frac{3}{2},1} C_{\frac{1}{2},1}\ e^{i(\phi_\Lambda+\phi_p)}\}$ | $\frac{\sqrt{3}}{2}\ \cos\theta_p\ \sin\theta_p$ | $\sin\theta_\Lambda$ |
| 6 | $\mathrm{Re}\{C^*_{-\frac{3}{2},-1} C_{-\frac{1}{2},-1}\ e^{-i(\phi_\Lambda+\phi_p)}\}$ | $\frac{\sqrt{3}}{2}\ \cos\theta_p\ \sin\theta_p$ | $\sin\theta_\Lambda$ |

Integrating the decay probability over the appropriate solid angle elements, one obtains the photon angular distribution:

$$\frac{d\Gamma}{d\cos\theta_\gamma} \propto 1 - \alpha_{\gamma,3/2} P_{\Lambda_b} \cos\theta_\gamma \tag{5.13}$$

where:

$$\alpha_{\gamma,3/2} = \frac{\overbrace{|C_{\frac{3}{2},1}|^2 + |C_{-\frac{1}{2},-1}|^2}^{\lambda_\Lambda - \lambda_\gamma = 1/2} - \overbrace{|C_{-\frac{3}{2},-1}|^2 - |C_{\frac{1}{2},1}|^2}^{\lambda_\Lambda - \lambda_\gamma = -1/2}}{|C_{\frac{3}{2},1}|^2 + |C_{-\frac{1}{2},-1}|^2 + |C_{-\frac{3}{2},-1}|^2 + |C_{\frac{1}{2},1}|^2} \tag{5.14}$$

which defines the asymmetry of the $\Lambda_b$ spin projection with respect to the photon momentum.

We will now disentangle the contributions due to the photon emission and the formation of the $\Lambda(X)$ resonance. We assume that the photon production is independent from the $\Lambda(X)$ state formed in the hadronization process, which allows us to write:

$$\alpha_\gamma = \frac{P(\gamma_L) - P(\gamma_R)}{P(\gamma_L) + P(\gamma_R)} = \frac{|C_{-\frac{1}{2},-1}|^2 - |C_{\frac{1}{2},1}|^2}{|C_{-\frac{1}{2},-1}|^2 + |C_{\frac{1}{2},1}|^2} = \frac{|C_{-\frac{3}{2},-1}|^2 - |C_{\frac{3}{2},1}|^2}{|C_{-\frac{3}{2},-1}|^2 + |C_{\frac{3}{2},1}|^2}$$

We furthermore define the ratio of the $\Lambda(X)$ helicity amplitudes:

$$\eta = \frac{|C_{\frac{3}{2},1}|^2}{|C_{\frac{1}{2},1}|^2} = \frac{|C_{-\frac{3}{2},-1}|^2}{|C_{-\frac{1}{2},-1}|^2} \tag{5.15}$$

Since parity is conserved in strong interactions, the same ratio $\eta$ can be assumed for positive and negative helicities.

Then (5.14) becomes

$$\alpha_{\gamma,3/2} = \frac{1-\eta}{1+\eta}\,\alpha_\gamma \tag{5.16}$$

The photon angular distribution has the same form as (5.9), with the additional factor $\frac{1-\eta}{1+\eta}$ which takes into account the fact that the $\Lambda(X)$ can now access more helicity states.

The proton angular distribution can be written as:

$$\frac{d\Gamma}{d\cos\theta_p} \propto 1 - \alpha_{p,3/2}\cos^2\theta_p \tag{5.17}$$

where:

$$\alpha_{p,3/2} = \frac{\overbrace{|C_{\frac{3}{2},1}|^2 + |C_{-\frac{3}{2},-1}|^2}^{|\lambda_\Lambda|=3/2} - \overbrace{|C_{\frac{1}{2},1}|^2 - |C_{-\frac{1}{2},-1}|^2}^{|\lambda_\Lambda|=1/2}}{|C_{\frac{3}{2},1}|^2 + |C_{-\frac{3}{2},-1}|^2 + \frac{1}{3}(|C_{-\frac{1}{2},-1}|^2 + |C_{\frac{1}{2},1}|^2)} = \frac{\eta - 1}{\eta + \frac{1}{3}} \tag{5.18}$$

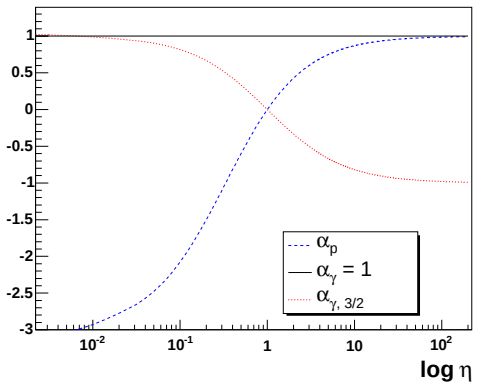



Figure 5.3: *The asymmetry parameters $\alpha_{\gamma,3/2}$ (dotted red) and $\alpha_{p,3/2}$ (dashed blue) as a function of $\log\eta$, for the SM expectation of $\alpha_\gamma$ (solid black) = 1.*

The proton angular distribution is symmetric around $\cos\theta_p = 0$, as expected in a strong decay, but it can be used to extract the value of $\eta$. Since no theoretical predictions exist for $\eta$, we will now study the three cases (see also fig. 5.3):

$\eta \ll 1$ The fraction of $\Lambda(X)$ with helicity 1/2 dominates. $\alpha_{p,3/2} \simeq -3$ and $\alpha_{\gamma,3/2} \simeq \alpha_\gamma$.

$\eta \simeq 1$ About the same amount of $\Lambda(X)$ with helicity 3/2 and 1/2 are produced. The parameters $\alpha_{p,3/2} \simeq \alpha_{\gamma,3/2} \simeq 0$, and the angular distributions (5.13) and (5.17) are flat.

$\eta \gg 1$ The fraction of $\Lambda(X)$ with helicity 3/2 dominates. $\alpha_{p,3/2} \simeq 1$ and $\alpha_{\gamma,3/2} \simeq -\alpha_\gamma$.

To summarize, if $\eta \simeq 1$ no asymmetry will be found in the photon angular distribution, and no measurement of $|r|$ is possible. On the other hand, if a photon asymmetry is measured, combining the measurement of $\alpha_{\gamma,3/2}$ and the proton parameter $\alpha_{p,3/2}$ one can obtain the photon polarization:

$$\alpha_\gamma = \frac{1}{2}\,\alpha_{\gamma,3/2}\left(1 - \frac{3}{\alpha_{p,3/2}}\right) \tag{5.19}$$

and the ratio $|r|$ can be probed as in spin 1/2 $\Lambda(X)$ decays. Note that an independent measurement of the $\Lambda_b$ polarization is necessary for the extraction of $\alpha_{\gamma,3/2}$ from the measured photon angular distribution.

## 5.5 Measuring the photon polarization in $\Lambda_b \to \Lambda(X)\gamma$ decays.

From the theoretical point of view, probing the photon polarization in the decay $\Lambda_b \to \Lambda(1115)\gamma$ is very promising due to the two independent measurements that can be extracted from the photon and the proton angular distributions. We have seen in the previous section that the photon polarization can also be measured in $\Lambda_b$ radiative decays which involve higher $\Lambda$ resonances[4] with spin = 1/2, 3/2. We will now examine which $\Lambda(X)$ resonances are the most promising from the experimental point of view.

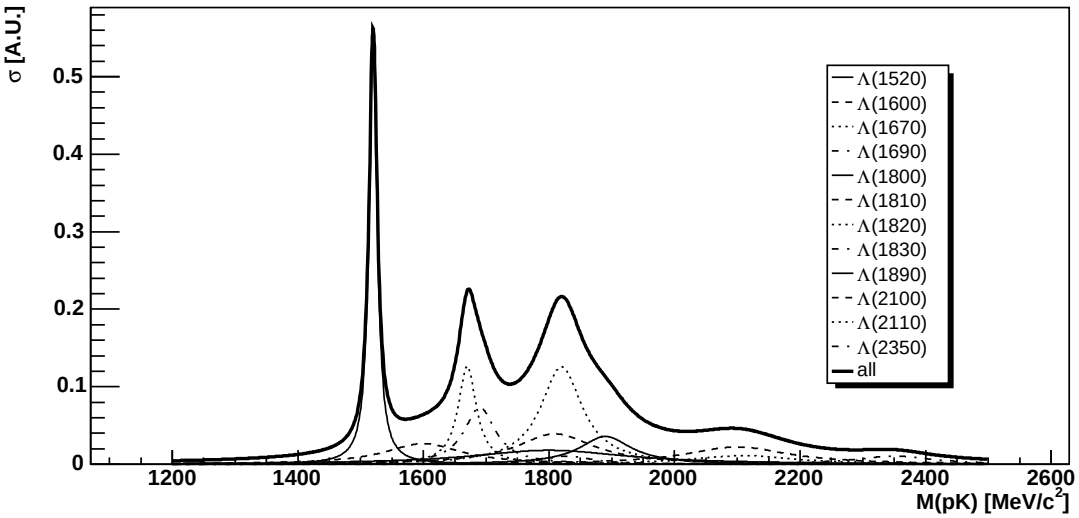



Figure 5.4: *Invariant $pK$ mass spectrum from $\Lambda_b \to \Lambda(X)\gamma$ decays. The contribution of each resonance and the overall cross section are shown. Only resonances with an experimental status of at least *** (with reference to table 5.1) are shown. The non-relativistic Breit Wigner distribution has been used for the decays $\Lambda(X) \to pK$. $\Lambda(X)$ (averaged) parameters from [101]. The $\Lambda_b \to \Lambda(X)\gamma$ decays branching ratios are assumed to be independent of the $pK$ mass (see section 5.2.2). Non-resonant contributions have been neglected.*

Fig. 5.4 illustrates the $pK$ invariant mass spectrum as we can expect to observe it from radiative $\Lambda_b$ decays. The spectrum presents three peaks in the region of the $\Lambda$ resonances. The first peak belongs to the $\Lambda(1520)$ alone, therefore this resonance should be the easiest

[4] In this case however only the photon angular distribution is useful.

to observe. Since the $\Lambda(1520)$ has spin 3/2 the extraction of the photon polarization via angular distributions is possible only if the proton parameter $\eta$ is sufficiently far from 1.

The second peak is given by both the $\Lambda(1670)$ (spin 1/2) and the $\Lambda(1690)$ (spin 3/2). It may be assumed that the different angular distributions will allow us to distinguish the two resonances. $\alpha_\gamma$ could then be extracted from a combined fit applied to events in that region.

The third (possible[5]) peak is formed by the contribution of the $\Lambda(1810)$ (spin 1/2), the $\Lambda(1820)$ (spin 5/2), the $\Lambda(1830)$ (spin 5/2) and the $\Lambda(1890)$ (spin 3/2). The dominant contribution to this peak is given by the $\Lambda(1820)$, which has spin 5/2, therefore it is not useful for the determination of the photon polarization.

We identify therefore as decays of interest for the photon polarization measurements the ones involving a $\Lambda(1115)$, $\Lambda(1520)$, $\Lambda(1670)$ or $\Lambda(1690)$ baryon. In the following chapters we will study the reconstruction of such decays in the LHCb environment, and will estimate the LHCb sensitivity to $r$.

[5]The decay width of $\Lambda$ resonances in this region are poorly known.

# Appendix to Chapter 5

## 5.A Angular distributions for the decay $\Lambda_b \to \Lambda(X)\gamma$

Detailed calculations of the final states angular distributions are given for the decay $\Lambda_b \to \Lambda(X)\gamma$, for $\Lambda(X)$ baryons of spin $J_\Lambda$ equal to $1/2$ and $3/2$. All used notations have already been defined in chapter 5.

### 5.A.1 The case $J_\Lambda = \frac{1}{2}$

Let us consider first the decay $\Lambda_b \to \Lambda(X)\gamma$. The relevant quantum numbers are:

| | $\Lambda_b$ | $\Lambda(X)$ | $\gamma$ |
|---|---|---|---|
| $J$ | $\frac{1}{2}$ | $\frac{1}{2}$ | $1$ |
| $\lambda$ | $\pm\frac{1}{2}$ | $\pm\frac{1}{2}$ | $\pm 1$ |

The allowed helicity combinations are:

| $\lambda_\Lambda$ | $\lambda_\gamma$ | $\lambda_\Lambda - \lambda_\gamma$ |
|---|---|---|
| $+1/2$ | $+1$ | $-1/2$ |
| $-1/2$ | $-1$ | $+1/2$ |

The helicity amplitudes are then given by the following $2 \times 2$ matrix:

$$C_{\lambda_\Lambda,\lambda_\gamma} = \begin{pmatrix} C_{\frac{1}{2},1} & C_{\frac{1}{2},-1} \\ C_{-\frac{1}{2},1} & C_{-\frac{1}{2},-1} \end{pmatrix} = C_{\lambda_\Lambda - \lambda_\gamma} = \begin{pmatrix} C_{-\frac{1}{2}} & 0 \\ 0 & C_{\frac{1}{2}} \end{pmatrix}$$

The amplitude probability (5.5) can be rewritten as:

$$A = \sum_\lambda D^{\frac{1}{2}*}_{\lambda_\Lambda,\lambda_p}(\phi_p,\theta_p,-\phi_p) D^{\frac{1}{2}*}_{M,\lambda}(\phi_\Lambda,\theta_\Lambda,-\phi_\Lambda) C_\lambda E_{\lambda_p} \tag{5.20}$$

where $\lambda = \lambda_\Lambda - \lambda_\gamma$.

We can use the fact that $C_{\lambda_\Lambda,\lambda_\gamma} C^*_{\lambda'_\Lambda,\lambda_\gamma} = \delta_{\lambda_\Lambda,\lambda'_\Lambda} |C_\lambda|^2$ to evaluate:

$$\begin{aligned} |A|^2 &= \sum_\lambda \sum_{\lambda'} D^{\frac{1}{2}*}_{\lambda_\Lambda,\lambda_p} D^{\frac{1}{2}*}_{M,\lambda} C_\lambda E_{\lambda_p} D^{\frac{1}{2}}_{\lambda'_\Lambda,\lambda_p} D^{\frac{1}{2}}_{M,\lambda'} C^*_{\lambda'} E^*_{\lambda_p} \\ &= \sum_\lambda |D^{\frac{1}{2}}_{\lambda_\Lambda,\lambda_p}|^2 |D^{\frac{1}{2}}_{M,\lambda}|^2 |C_\lambda|^2 |E_{\lambda_p}|^2 \end{aligned}$$

The decay probability (5.7) becomes (the sum over $\lambda_\gamma$ has been dropped since it is related to $\lambda_\Lambda$):

$$\begin{aligned} w_{\frac{1}{2}} &= \sum_{M,\lambda_p} \rho_{MM} |A|^2 = \sum_{M,\lambda_p,\lambda} \rho_{MM} |D^{\frac{1}{2}}_{\lambda_\Lambda,\lambda_p}|^2 |D^{\frac{1}{2}}_{M,\lambda}|^2 |C_\lambda|^2 |E_{\lambda_p}|^2 \\ &= \sum_{\lambda_p,\lambda} |C_\lambda|^2 |E_{\lambda_p}|^2 |D^{\frac{1}{2}}_{\lambda_\Lambda,\lambda_p}|^2 \left[ \rho_{++} |D^{\frac{1}{2}}_{\frac{1}{2},\lambda}|^2 + \rho_{--} |D^{\frac{1}{2}}_{-\frac{1}{2},\lambda}|^2 \right] \end{aligned}$$

Let us now add some considerations on the second decay $\Lambda(X) \to p\, h$, where we have:

| | $\Lambda(X)$ | $p$ | $x$ |
|---|---|---|---|
| $J$ | $\frac{1}{2}$ | $\frac{1}{2}$ | 0 |
| $\lambda$ | $\pm\frac{1}{2}$ | $\pm\frac{1}{2}$ | 0 |

In this case the helicity matrix takes the simple form:

$$E_{\lambda_p} = \begin{pmatrix} E_{\frac{1}{2}} \\ E_{-\frac{1}{2}} \end{pmatrix}$$

Adding in, we obtain for the decay probability:

$$\begin{aligned} w_{\frac{1}{2}} &= \sum_{\lambda} |C_\lambda|^2 \left[ |E_{\frac{1}{2}}|^2 |D^{\frac{1}{2}}_{\lambda_\Lambda,\frac{1}{2}}|^2 + |E_{-\frac{1}{2}}|^2 |D^{\frac{1}{2}}_{\lambda_\Lambda,-\frac{1}{2}}|^2 \right] \left[ \rho_{++} |D^{\frac{1}{2}}_{\frac{1}{2},\lambda}|^2 + \rho_{--} |D^{\frac{1}{2}}_{-\frac{1}{2},\lambda}|^2 \right] \\ &= |C_{\frac{1}{2}}|^2 \left[ |E_{\frac{1}{2}}|^2 |d^{\frac{1}{2}}_{-\frac{1}{2},\frac{1}{2}}(\theta_p)|^2 + |E_{-\frac{1}{2}}|^2 |d^{\frac{1}{2}}_{-\frac{1}{2},-\frac{1}{2}}(\theta_p)|^2 \right] \left[ \rho_{++} |d^{\frac{1}{2}}_{\frac{1}{2},\frac{1}{2}}(\theta_\Lambda)|^2 + \rho_{--} |d^{\frac{1}{2}}_{-\frac{1}{2},\frac{1}{2}}(\theta_\Lambda)|^2 \right] \\ &\quad + |C_{-\frac{1}{2}}|^2 \left[ |E_{\frac{1}{2}}|^2 |d^{\frac{1}{2}}_{\frac{1}{2},\frac{1}{2}}(\theta_p)|^2 + |E_{-\frac{1}{2}}|^2 |d^{\frac{1}{2}}_{\frac{1}{2},-\frac{1}{2}}(\theta_p)|^2 \right] \left[ \rho_{++} |d^{\frac{1}{2}}_{\frac{1}{2},-\frac{1}{2}}(\theta_\Lambda)|^2 + \rho_{--} |d^{\frac{1}{2}}_{-\frac{1}{2},-\frac{1}{2}}(\theta_\Lambda)|^2 \right] \end{aligned}$$

where we used the fact that:

$$D^j_{m,m'}(\alpha,\beta,\gamma) = e^{i\alpha m'} d^j_{m,m'}(\beta) e^{-i\gamma m} \tag{5.21}$$

Using:

$$d^J_{M',M}(\theta) = (-1)^{M-M'} d^J_{M,M'}(\theta) = d^J_{-M,-M'}(\theta)$$

and

$$d^{\frac{1}{2}}_{\frac{1}{2},\frac{1}{2}}(\theta) = d^{\frac{1}{2}}_{-\frac{1}{2},-\frac{1}{2}}(\theta) = \cos\frac{\theta}{2}$$

$$d^{\frac{1}{2}}_{\frac{1}{2},-\frac{1}{2}}(\theta) = d^{\frac{1}{2}}_{-\frac{1}{2},\frac{1}{2}}(\theta) = -\sin\frac{\theta}{2}$$

we can further simplify:

$$\begin{aligned} w_{\frac{1}{2}} &= |C_{\frac{1}{2}}|^2 \left( \rho_{++} \cos^2\frac{\theta_\Lambda}{2} + \rho_{--} \sin^2\frac{\theta_\Lambda}{2} \right) \left( |E_{\frac{1}{2}}|^2 \sin^2\frac{\theta_p}{2} + |E_{-\frac{1}{2}}|^2 \cos^2\frac{\theta_p}{2} \right) \\ &\quad + |C_{-\frac{1}{2}}|^2 \left( \rho_{++} \sin^2\frac{\theta_\Lambda}{2} + \rho_{--} \cos^2\frac{\theta_\Lambda}{2} \right) \left( |E_{\frac{1}{2}}|^2 \cos^2\frac{\theta_p}{2} + |E_{-\frac{1}{2}}|^2 \sin^2\frac{\theta_p}{2} \right) \end{aligned}$$

We now remark that the expression:

$$A\cos^2\frac{\theta}{2} + B\sin^2\frac{\theta}{2} = A\frac{1+\cos\theta}{2} + B\frac{1-\cos\theta}{2} \propto \frac{1}{2}\left(1 + \frac{A-B}{A+B}\cos\theta\right)$$

then the transition probability becomes:

$$\begin{aligned} w_{\frac{1}{2}} &\propto |C_{\frac{1}{2}}|^2 \left( 1 + \frac{\rho_{++}-\rho_{--}}{\rho_{++}+\rho_{--}} \cos\theta_\Lambda \right) \left( 1 - \frac{|E_{\frac{1}{2}}|^2 - |E_{-\frac{1}{2}}|^2}{|E_{\frac{1}{2}}|^2 + |E_{-\frac{1}{2}}|^2} \cos\theta_p \right) \\ &\quad + |C_{-\frac{1}{2}}|^2 \left( 1 - \frac{\rho_{++}-\rho_{--}}{\rho_{++}+\rho_{--}} \cos\theta_\Lambda \right) \left( 1 + \frac{|E_{\frac{1}{2}}|^2 - |E_{-\frac{1}{2}}|^2}{|E_{\frac{1}{2}}|^2 + |E_{-\frac{1}{2}}|^2} \cos\theta_p \right) \end{aligned} \tag{5.22}$$

We can now define the following quantities, which depend on the helicity amplitudes:

$$\text{Photon asymmetry:} \quad \alpha_{\gamma,1/2} = \frac{|C_{\frac{1}{2}}|^2 - |C_{-\frac{1}{2}}|^2}{|C_{\frac{1}{2}}|^2 + |C_{-\frac{1}{2}}|^2}$$

$$\text{Proton asymmetry:} \quad \alpha_{p,1/2} = \frac{|E_{\frac{1}{2}}|^2 - |E_{-\frac{1}{2}}|^2}{|E_{\frac{1}{2}}|^2 + |E_{-\frac{1}{2}}|^2}$$

We remark that $\alpha_{\gamma,1/2}$ represents the photon polarization which we defined as:

$$\alpha_\gamma = \frac{P(\gamma_L) - P(\gamma_R)}{P(\gamma_L) + P(\gamma_R)} = \alpha_{\gamma,1/2}$$

In case of parity conservation in the decay $\Lambda(X) \to p\ K$, $\alpha_{p,1/2} = 0$.

Inserting the asymmetries defined above, and the $\Lambda_b$ polarization (5.6), into the transition probability, one finally obtains:

$$\begin{aligned} w_{\frac{1}{2}} &\propto |C_{\frac{1}{2}}|^2 (1 + P_{\Lambda_b} \cos\theta_\Lambda) \left(1 - \alpha_{p,1/2} \cos\theta_p\right) + |C_{-\frac{1}{2}}|^2 (1 - P_{\Lambda_b} \cos\theta_\Lambda) \left(1 + \alpha_{p,1/2} \cos\theta_p\right) \\ &\propto (1 - \alpha_{p,1/2} P_{\Lambda_b} \cos\theta_p \cos\theta_\Lambda)(|C_{\frac{1}{2}}|^2 + |C_{-\frac{1}{2}}|^2) \\ &\quad + (P_{\Lambda_b} \cos\theta_\Lambda - \alpha_{p,1/2} \cos\theta_p)(|C_{\frac{1}{2}}|^2 - |C_{-\frac{1}{2}}|^2) \\ &\propto 1 - \alpha_{p,1/2} P_{\Lambda_b} \cos\theta_p \cos\theta_\Lambda - \alpha_\gamma(\alpha_{p,1/2} \cos\theta_p - P_{\Lambda_b} \cos\theta_\Lambda) \end{aligned} \tag{5.23}$$

### 5.A.2 The case $J_\Lambda = \frac{3}{2}$

Increasing the spin of the $\Lambda(X)$ baryon means increasing the number of possible helicity combinations. For $J_\Lambda = 3/2$, the $\Lambda(X)$ helicity can assume the values $\pm 1/2, \pm 3/2$. The allowed helicity combinations become:

| $\lambda_\Lambda$ | $\lambda_\gamma$ | $\lambda_\Lambda - \lambda_\gamma$ |
|---|---|---|
| $+3/2$ | $+1$ | $+1/2$ |
| $+1/2$ | $+1$ | $-1/2$ |
| $-1/2$ | $-1$ | $+1/2$ |
| $-3/2$ | $-1$ | $-1/2$ |

The helicity amplitudes are given by the following $4 \times 2$ matrix:

$$C_{\lambda_\Lambda,\lambda_\gamma} = \begin{pmatrix} C_{\frac{3}{2},1} & 0 \\ C_{\frac{1}{2},1} & 0 \\ 0 & C_{-\frac{1}{2},-1} \\ 0 & C_{-\frac{3}{2},-1} \end{pmatrix}$$

The decay amplitude (5.5) becomes:

$$A = \sum_{\lambda_\Lambda} D^{\frac{3}{2}*}_{\lambda_\Lambda,\lambda_p}(\phi_p, \theta_p, -\phi_p) D^{\frac{1}{2}*}_{M,\lambda_\Lambda-\lambda_\gamma}(\phi_\Lambda, \theta_\Lambda, -\phi_\Lambda) C_{\lambda_\Lambda,\lambda_\gamma} E_{\lambda_p} \tag{5.24}$$

The squared amplitude is then:

$$\begin{aligned} |A|^2 &= \sum_{\lambda_\Lambda} \sum_{\lambda'_\Lambda} D^{\frac{3}{2}*}_{\lambda_\Lambda,\lambda_p} D^{\frac{3}{2}}_{\lambda'_\Lambda,\lambda_p} D^{\frac{1}{2}*}_{M,\lambda_\Lambda-\lambda_\gamma} D^{\frac{1}{2}}_{M,\lambda'_\Lambda-\lambda_\gamma} C_{\lambda_\Lambda,\lambda_\gamma} C^*_{\lambda'_\Lambda,\lambda_\gamma} |E_{\lambda_p}|^2 \\ &= \sum_{\lambda_\Lambda,\lambda'_\Lambda} d^{\frac{3}{2}}_{\lambda_\Lambda,\lambda_p}(\theta_p) d^{\frac{3}{2}}_{\lambda'_\Lambda,\lambda_p}(\theta_p) d^{\frac{1}{2}}_{M,\lambda_\Lambda-\lambda_\gamma}(\theta_\Lambda) d^{\frac{1}{2}}_{M,\lambda'_\Lambda-\lambda_\gamma}(\theta_\Lambda) e^{i(\phi_\Lambda+\phi_p)(\lambda'_\Lambda-\lambda_\Lambda)} C_{\lambda_\Lambda,\lambda_\gamma} C^*_{\lambda'_\Lambda,\lambda_\gamma} \end{aligned}$$

where (5.21) has been used. The factor $|E_{\lambda_p}|^2$ has been dropped because of parity conservation ($|E_{-\frac{1}{2}}| = |E_{\frac{1}{2}}|$).
With the helicity matrix above we can evaluate the following product separately for $\lambda_\Lambda, \lambda_\gamma > 0$:

$$\begin{aligned}\sum_{\lambda_\Lambda,\lambda'_\Lambda} C_{\lambda_\Lambda,\lambda_\gamma} e^{-i\alpha\lambda_\Lambda} C^*_{\lambda'_\Lambda,\lambda_\gamma} e^{i\alpha\lambda'_\Lambda} &= (C_{\frac{3}{2},1} e^{-i\frac{3}{2}\alpha} + C_{\frac{1}{2},1} e^{-i\frac{1}{2}\alpha})(C^*_{\frac{3}{2},1} e^{i\frac{3}{2}\alpha} + C^*_{\frac{1}{2},1} e^{i\frac{1}{2}\alpha}) \\ &= |C_{\frac{3}{2},1}|^2 + |C_{\frac{1}{2},1}|^2 + 2\,\mathrm{Re}\{C^*_{\frac{3}{2},1} C_{\frac{1}{2},1} e^{i\alpha}\}\end{aligned}$$

For symmetry reasons, if $\lambda_\Lambda, \lambda_\gamma < 0$, we have:

$$\sum_{\lambda_\Lambda,\lambda'_\Lambda} C_{\lambda_\Lambda,\lambda_\gamma} e^{-i\alpha\lambda_\Lambda} C^*_{\lambda'_\Lambda,\lambda_\gamma} e^{i\alpha\lambda'_\Lambda} = |C_{-\frac{3}{2},-1}|^2 + |C_{-\frac{1}{2},-1}|^2 + 2\,\mathrm{Re}\{C^*_{-\frac{3}{2},-1} C_{-\frac{1}{2},-1} e^{-i\alpha}\}$$

These results can be used to evaluate the squared amplitude:

$$\begin{aligned}|A|^2 \;\propto\; &\underbrace{|C_{\frac{3}{2},1}|^2 |d^{\frac{3}{2}}_{\frac{3}{2},\lambda_p}(\theta_p) d^{\frac{1}{2}}_{M,\frac{1}{2}}(\theta_\Lambda)|^2}_{|A_1|^2} + \underbrace{|C_{-\frac{3}{2},-1}|^2 |d^{\frac{3}{2}}_{-\frac{3}{2},\lambda_p}(\theta_p) d^{\frac{1}{2}}_{M,-\frac{1}{2}}(\theta_\Lambda)|^2}_{|A_2|^2} \\ &+ \underbrace{|C_{\frac{1}{2},1}|^2 |d^{\frac{3}{2}}_{\frac{1}{2},\lambda_p}(\theta_p) d^{\frac{1}{2}}_{M,-\frac{1}{2}}(\theta_\Lambda)|^2}_{|A_3|^2} + \underbrace{|C_{-\frac{1}{2},-1}|^2 |d^{\frac{3}{2}}_{-\frac{1}{2},\lambda_p}(\theta_p) d^{\frac{1}{2}}_{M,\frac{1}{2}}(\theta_\Lambda)|^2}_{|A_4|^2} \\ &+ \underbrace{2\,\mathrm{Re}\{C^*_{\frac{3}{2},1} C_{\frac{1}{2},1} e^{i(\phi_\Lambda+\phi_p)}\} d^{\frac{3}{2}}_{\frac{3}{2},\lambda_p}(\theta_p) d^{\frac{1}{2}}_{M,\frac{1}{2}}(\theta_\Lambda) d^{\frac{3}{2}}_{\frac{1}{2},\lambda_p}(\theta_p) d^{\frac{1}{2}}_{M,-\frac{1}{2}}(\theta_\Lambda)}_{|A_5|^2} \\ &+ \underbrace{2\,\mathrm{Re}\{C^*_{-\frac{3}{2},-1} C_{-\frac{1}{2},-1} e^{-i(\phi_\Lambda+\phi_p)}\} d^{\frac{3}{2}}_{-\frac{3}{2},\lambda_p}(\theta_p) d^{\frac{1}{2}}_{M,-\frac{1}{2}}(\theta_\Lambda) d^{\frac{3}{2}}_{-\frac{1}{2},\lambda_p}(\theta_p) d^{\frac{1}{2}}_{M,\frac{1}{2}}(\theta_\Lambda)}_{|A_6|^2}\end{aligned}$$

The decay probability (5.7) can be written as:

$$w_{\frac{3}{2}} = \sum_{i=1}^{6} w_i = \sum_{i=1}^{6} \sum_{M,\lambda_\Lambda,\lambda_p} \rho_{MM} |A_i|^2 \tag{5.25}$$

We will need the following $d$-functions:

$$\begin{aligned}d^{\frac{3}{2}}_{\frac{3}{2},\frac{1}{2}}(\theta) &= -\sqrt{3}\,\frac{1+\cos\theta}{2}\sin\frac{\theta}{2} = -\sqrt{3}\,\cos^2\frac{\theta}{2}\sin\frac{\theta}{2} \\ d^{\frac{3}{2}}_{\frac{3}{2},-\frac{1}{2}}(\theta) &= \sqrt{3}\,\frac{1-\cos\theta}{2}\cos\frac{\theta}{2} = \sqrt{3}\,\sin^2\frac{\theta}{2}\cos\frac{\theta}{2} \\ d^{\frac{3}{2}}_{-\frac{3}{2},-\frac{1}{2}}(\theta) &= d^{\frac{3}{2}}_{\frac{1}{2},\frac{3}{2}}(\theta) = d^{\frac{3}{2}}_{\frac{3}{2},\frac{1}{2}}(-\theta) = \sqrt{3}\,\cos^2\frac{\theta}{2}\sin\frac{\theta}{2} \\ d^{\frac{3}{2}}_{-\frac{3}{2},\frac{1}{2}}(\theta) &= d^{\frac{3}{2}}_{-\frac{1}{2},\frac{3}{2}}(\theta) = d^{\frac{3}{2}}_{\frac{3}{2},-\frac{1}{2}}(-\theta) = -\sqrt{3}\,\sin^2\frac{\theta}{2}\cos\frac{\theta}{2} \\ d^{\frac{3}{2}}_{\frac{1}{2},\frac{1}{2}}(\theta) &= d^{\frac{3}{2}}_{-\frac{1}{2},-\frac{1}{2}}(\theta) = \frac{3\cos\theta-1}{2}\cos\frac{\theta}{2} \\ d^{\frac{3}{2}}_{\frac{1}{2},-\frac{1}{2}}(\theta) &= d^{\frac{3}{2}}_{-\frac{1}{2},\frac{1}{2}}(\theta) = -\frac{3\cos\theta+1}{2}\sin\frac{\theta}{2}\end{aligned}$$

where we used the fact that

$$d^j_{mm'}(\theta) = d^j_{m'm}(-\theta)$$

Let us now calculate each contribution to the decay probability (5.25) separately:

$$\begin{aligned} w_1 &= \sum_{M,\lambda_p} \rho_{MM}|A_1|^2 = \sum_M \rho_{MM}|C_{\frac{3}{2},1}|^2 \left[|d^{\frac{3}{2}}_{\frac{3}{2},\frac{1}{2}}(\theta_p)|^2 + |d^{\frac{3}{2}}_{\frac{3}{2},-\frac{1}{2}}(\theta_p)|^2\right] |d^{\frac{1}{2}}_{M,\frac{1}{2}}(\theta_\Lambda)|^2 \\ &= 3\,|C_{\frac{3}{2},1}|^2 \cos^2\frac{\theta_p}{2}\sin^2\frac{\theta_p}{2}\sum_M \rho_{MM}|d^{\frac{1}{2}}_{M,\frac{1}{2}}(\theta_\Lambda)|^2 \\ &= 3\,|C_{\frac{3}{2},1}|^2 \cos^2\frac{\theta_p}{2}\sin^2\frac{\theta_p}{2}\left[\rho_{++}\cos^2\frac{\theta_\Lambda}{2} + \rho_{--}\sin^2\frac{\theta_\Lambda}{2}\right] \\ &= \frac{3}{8}\,\mathrm{det}\rho\,|C_{\frac{3}{2},1}|^2 \sin^2\theta_p\,(1 + P_{\Lambda_b}\cos\theta_\Lambda) \end{aligned}$$

where $\mathrm{det}\rho = \rho_{++} + \rho_{--} = 1$.

Similarly we have:

$$\begin{aligned} w_2 &= \sum_{M,\lambda_p} \rho_{MM}|A_2|^2 = \sum_M \rho_{MM}|C_{-\frac{3}{2},-1}|^2 \left[|d^{\frac{3}{2}}_{-\frac{3}{2},\frac{1}{2}}(\theta_p)|^2 + |d^{\frac{3}{2}}_{-\frac{3}{2},-\frac{1}{2}}(\theta_p)|^2\right] |d^{\frac{1}{2}}_{M,-\frac{1}{2}}(\theta_\Lambda)|^2 \\ &= 3\,|C_{-\frac{3}{2},-1}|^2 \cos^2\frac{\theta_p}{2}\sin^2\frac{\theta_p}{2}\left[\rho_{++}\sin^2\frac{\theta_\Lambda}{2} + \rho_{--}\cos^2\frac{\theta_\Lambda}{2}\right] \\ &= \frac{3}{8}\,|C_{-\frac{3}{2},-1}|^2 \sin^2\theta_p\,(1 - P_{\Lambda_b}\cos\theta_\Lambda) \end{aligned}$$

The third and fourth term become:

$$\begin{aligned} w_3 &= \sum_{M,\lambda_p} \rho_{MM}|A_3|^2 = \sum_M \rho_{MM}|C_{\frac{1}{2},1}|^2 \left[|d^{\frac{3}{2}}_{\frac{1}{2},\frac{1}{2}}(\theta_p)|^2 + |d^{\frac{3}{2}}_{\frac{1}{2},-\frac{1}{2}}(\theta_p)|^2\right] |d^{\frac{1}{2}}_{M,-\frac{1}{2}}(\theta_\Lambda)|^2 \\ &= \frac{1}{2}\,|C_{\frac{1}{2},1}|^2 \left[|d^{\frac{3}{2}}_{\frac{1}{2},\frac{1}{2}}(\theta_p)|^2 + |d^{\frac{3}{2}}_{\frac{1}{2},-\frac{1}{2}}(\theta_p)|^2\right] (1 - P_{\Lambda_b}\cos\theta_\Lambda) \end{aligned}$$

and

$$\begin{aligned} w_4 &= \sum_{M,\lambda_p} \rho_{MM}|A_4|^2 = \sum_M \rho_{MM}|C_{-\frac{1}{2},-1}|^2 \left[|d^{\frac{3}{2}}_{-\frac{1}{2},\frac{1}{2}}(\theta_p)|^2 + |d^{\frac{3}{2}}_{-\frac{1}{2},-\frac{1}{2}}(\theta_p)|^2\right] |d^{\frac{1}{2}}_{M,\frac{1}{2}}(\theta_\Lambda)|^2 \\ &= \frac{1}{2}\,|C_{-\frac{1}{2},-1}|^2 \left[|d^{\frac{3}{2}}_{-\frac{1}{2},-\frac{1}{2}}(\theta_p)|^2 + |d^{\frac{3}{2}}_{-\frac{1}{2},\frac{1}{2}}(\theta_p)|^2\right] (1 + P_{\Lambda_b}\cos\theta_\Lambda) \end{aligned}$$

where

$$|d^{\frac{3}{2}}_{\frac{1}{2},\frac{1}{2}}(\theta_p)|^2 + |d^{\frac{3}{2}}_{\frac{1}{2},-\frac{1}{2}}(\theta_p)|^2 = \frac{1}{4}\left[\cos^2\frac{\theta_p}{2}(3\cos\theta_p - 1)^2 + \sin^2\frac{\theta_p}{2}(3\cos\theta_p + 1)^2\right] = \frac{1}{4}\,(3\cos^2\theta_p + 1)$$

For the interference terms:

$$\begin{aligned} w_5 &= 2\,\mathrm{Re}\{C^*_{\frac{3}{2},1}C_{\frac{1}{2},1}e^{i(\phi_\Lambda+\phi_p)}\}\sum_{M,\lambda_p}\rho_{MM}d^{\frac{3}{2}}_{\frac{3}{2},\lambda_p}(\theta_p)d^{\frac{1}{2}}_{M,\frac{1}{2}}(\theta_\Lambda)d^{\frac{3}{2}}_{\frac{1}{2},\lambda_p}(\theta_p)d^{\frac{1}{2}}_{M,-\frac{1}{2}}(\theta_\Lambda) \\ w_6 &= 2\,\mathrm{Re}\{C^*_{-\frac{3}{2},1}C_{-\frac{1}{2},1}e^{-i(\phi_\Lambda+\phi_p)}\}\sum_{M,\lambda_p}\rho_{MM}d^{\frac{3}{2}}_{-\frac{3}{2},\lambda_p}(\theta_p)d^{\frac{1}{2}}_{M,-\frac{1}{2}}(\theta_\Lambda)d^{\frac{3}{2}}_{-\frac{1}{2},\lambda_p}(\theta_p)d^{\frac{1}{2}}_{M,\frac{1}{2}}(\theta_\Lambda) \end{aligned}$$

But

$$d^{\frac{1}{2}}_{M,\frac{1}{2}}(\theta)d^{\frac{1}{2}}_{M,-\frac{1}{2}}(\theta) = -\cos\frac{\theta}{2}\sin\frac{\theta}{2} = -\frac{1}{2}\sin\theta, \quad \text{for } M = \pm\frac{1}{2}$$

$$d^{\frac{3}{2}}_{\frac{3}{2},\lambda_p}(\theta)d^{\frac{3}{2}}_{\frac{1}{2},\lambda_p}(\theta) = d^{\frac{3}{2}}_{-\frac{3}{2},\lambda_p}(\theta)d^{\frac{3}{2}}_{-\frac{1}{2},\lambda_p}(\theta) = -\frac{\sqrt{3}}{8}\sin\theta\,(3\cos\theta \mp 1)\,(1 \pm \cos\theta), \quad \text{for } \lambda_p = \pm\frac{1}{2}$$

Therefore

$$\begin{aligned} w_5 &= \text{Re}\{C^*_{\frac{3}{2},1}C_{\frac{1}{2},1}e^{i(\phi_\Lambda+\phi_p)}\}\,\frac{\sqrt{3}}{2}\,\cos\theta_p\,\sin\theta_p\,\sin\theta_\Lambda \\ w_6 &= \text{Re}\{C^*_{-\frac{3}{2},1}C_{-\frac{1}{2},1}e^{-i(\phi_\Lambda+\phi_p)}\}\,\frac{\sqrt{3}}{2}\,\cos\theta_p\,\sin\theta_p\,\sin\theta_\Lambda \end{aligned}$$

We can now factorize the various contributions to the decay probability (5.25) as follows:

$$w_{\frac{3}{2}} = \sum_{i=1}^{6} w_i = \sum_{i=1}^{6} C_i(\phi_\Lambda, \phi_p)\cdot f_i(\theta_p)\cdot g_i(\theta_\Lambda, P_{\Lambda_b}) \tag{5.26}$$

where:

$C_i(\phi_\Lambda, \phi_p)$ are functions of the relevant helicity amplitudes and the azimuthal angles $\phi_\Lambda$ and $\phi_p$;

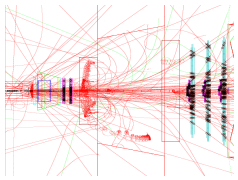
$f_i(\theta_p)$ are functions of the proton polar angle $\theta_p$;

$g_i(\theta_\Lambda, P_{\Lambda_b})$ are functions depending on the $\Lambda$ polar angle $\theta_\Lambda$ and the $\Lambda_b$ polarization $P_{\Lambda_b}$.

The $C_i$, $f_i$ and $g_i$ are reported in table 5.2.

Chapter 6

# The decays $\Lambda_b \to \Lambda(X)\gamma$ at LHCb



*Polarized radiative $\Lambda_b$ decays are studied in the LHCb environment. In particular, events generation, simulation and selection are covered in this chapter.*

## 6.1 Introduction

As we have seen in the previous chapter, interesting tests of the Standard Model can be made by measuring the final states angular distributions of decays of the type $\Lambda_b \to \Lambda(X)\gamma$.

As an example of radiative $\Lambda_b$ decays, we present the reconstruction of the decays:

$$\Lambda_b \to (\Lambda(1115) \to p\ \pi)\gamma \tag{6.1}$$

$$\Lambda_b \to (\Lambda(1670) \to p\ K)\gamma \tag{6.2}$$

at LHCb, based on a full Monte Carlo (MC) simulation. The results obtained for channel (6.2) can be extended to any $\Lambda(X)$ resonance which decays strongly in $pK$, while channel (6.1) needs a separate treatment. Its reconstruction is in fact more delicate, due to the fact that the $\Lambda(1115)$ ($c\tau$= 7.89 cm) traverses a large fraction of the LHCb tracking system before decaying to $p\pi$.

Since LHC is not yet running, to measure a detector performance on a particular channel we can only use Monte Carlo (MC) generated events (see section 3.4 for a short introduction to the LHCb software). We summarize here the steps the analysts normally follows, and indicate in which section one can find the specific strategy followed for the reconstruction of the decays (6.1) and (6.2):

**Event generation** The decay chain of interest is generated. It is up to the analyst to insert the most realistic parameters, such as branching ratios, angular distributions, etc. for that particular channel. See section 6.2.

**Event simulation and reconstruction** Based on the generated decay chain, LHCb simulation software takes care of simulating the response of the detector. The reconstruction algorithm attempts then to find tracks and vertices in the simulated detector data. Event reconstruction is addressed in section 6.3. Detector and reconstruction efficiencies are discussed in section 6.4.

**Selection algorithms** The analyst tries to select the events of interest, by exploiting the specific features that distinguish them from the background. The selection algorithm and its performances are reported in section 6.5.

**Evaluation of the performances** The analyst evaluates whether a search for that particular channel is possible in LHCb, given the event yield and the ratio of selected signal events over background events. Section 6.6 contains the expected event yields for the decays of interest and the feasibility of Branching Ratio (BR) studies.

**Sensitivity measurements** If a search is possible, it is then interesting to know what could be the LHCb physics reach for that particular channel, i.e. whether precision measurements of interesting observables can be made. The feasibility of the photon polarization measurement is discussed in chapter 7.

## 6.2 Event generation

The event generation is accomplished by PYTHIA [106], which generates minimum bias $pp$ interactions at $\sqrt{s} = 14$ TeV. The $b\bar{b}$ cross section is poorly known, and a value of 500 $\mu$b is the working assumption for LHCb. The hadronization fractions of the $b$ quark used in PYTHIA are the following: 40% $B^0$, 40% $B^{\pm}$, 12% $B_s$, and 8% $\Lambda_b$. Signal events are then obtained by selecting the appropriate $b\bar{b}$ events from the minimum bias sample. To reduce the number of reconstructed events where not all the decay products are in the detector acceptance, a cut of 400 mrad on the true polar angle of the signal $b$-hadron is imposed at generator level.

EvtGen [68] is then used to decay all the particles. Various decay models are available to generate the correct angular distributions of the final states. For this analysis we used the HELAMP model, which takes as input the helicity amplitudes of the involved decays. For simplicity's sake, we generated decays involving $\Lambda(X)$ baryons of spin 1/2. The results can be easily extended to $\Lambda(X)$ baryons of spin 3/2.

To maximize the effect of the asymmetries, the following settings have been chosen for the $\Lambda_b$ and the $\gamma$ polarization:

- $P_{\Lambda_b} = 1$, for polarized decays,
- $\alpha_\gamma = 1$, for the decay $\Lambda_b \to \Lambda(X)\gamma$.

The proton polarization parameter has been set to:

- $\alpha_{p,1/2} = 0.642$, for the decay $\Lambda(1115) \to p\,\pi$,
- $\alpha_{p,1/2} = 0$, for the decay $\Lambda(X) \to p\,K$.

The possibility of generating polarized $\Lambda_b$ baryons had to be included in the generation software. Since it was the first time that polarized $\Lambda_b$ decays were simulated within LHCb, we checked the generation of the correct angular distributions. For this purpose, small

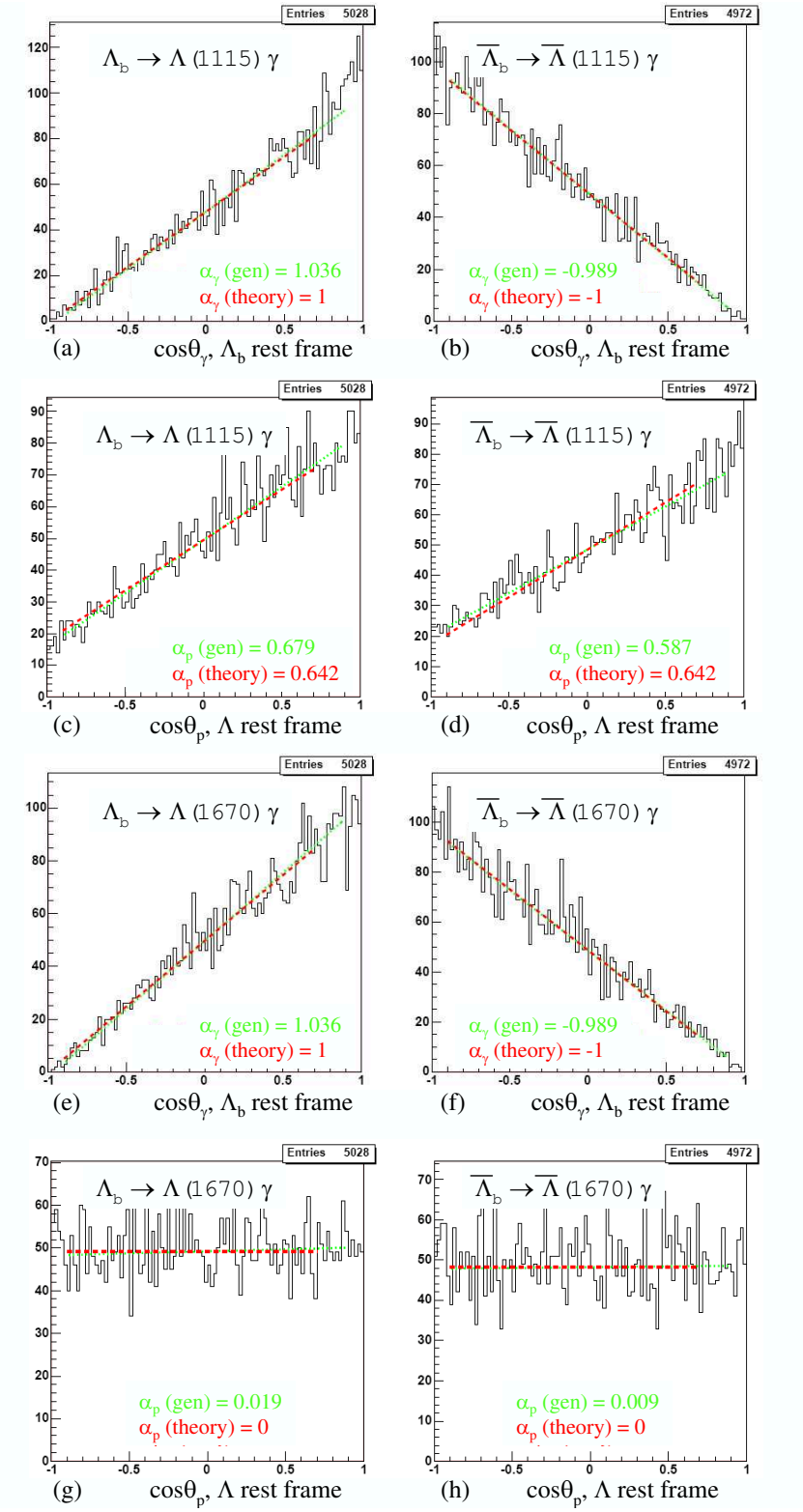



Figure 6.1: *Photon (a, b, e, f) and proton (c, d, g, h) angular distributions for decays of type of type* $\Lambda_b \to \Lambda(1115)\gamma$ *(a, b, c, d) and* $\Lambda_b \to \Lambda(1670)\gamma$ *(e, f, g, h) from EvtGen (HELAMP model, transversal* $\Lambda_b$ *polarization). The left plots show* $\Lambda_b$ *decays and the right ones* $\overline{\Lambda}_b$ *decays. The theoretical distribution (dashed red) and a linear fit of the generated data (dotted green) are also shown.*

Table 6.1: $\Lambda_b \to \Lambda(X)\gamma$ *events used to check the correct generation by EvtGen. The last two columns contain the parameters of the generation.*

| Type | Decay | $\Lambda_b$ polarization | EvtGen model |
|---|---|---|---|
| I | $\Lambda_b \to \Lambda(1115)\gamma$ | no | phase space |
| II | $\Lambda_b \to \Lambda(1115)\gamma$ | longitudinal | HELAMP |
| III | $\Lambda_b \to \Lambda(1115)\gamma$ | transversal | HELAMP |
| IV | $\Lambda_b \to \Lambda(1520)\gamma$ | no | phase space |
| V | $\Lambda_b \to \Lambda(1600)\gamma$ | no | phase space |
| VI | $\Lambda_b \to \Lambda(1600)\gamma$ | longitudinal | HELAMP |
| VII | $\Lambda_b \to \Lambda(1600)\gamma$ | transversal | HELAMP |
| VIII | $\Lambda_b \to \Lambda(1670)\gamma$ | no | phase space |
| IX | $\Lambda_b \to \Lambda(1670)\gamma$ | longitudinal | HELAMP |
| X | $\Lambda_b \to \Lambda(1670)\gamma$ | transversal | HELAMP |

samples of various radiative decays (10k events of each type) have been generated, for both $\Lambda_b$ and $\overline{\Lambda}_b$ events (see table 6.1 for a list of the generated decays).

The results of event generation are shown in fig. 6.1 for the decays III and X (with reference to table 6.1), where one can check the goodness of the generation comparing the theoretical and generated angular distributions.

## 6.3 Event simulation and reconstruction

The generated particles are tracked through the detector material and the surrounding environment. The response of the detector is simulated using the GEANT4 package [107]. The reconstruction algorithms, which take as input the detector signals and search for tracks and vertices, are described elsewhere [46], and are run inside the BRUNEL [71] software package.

We will now introduce the principles of track reconstruction in LHCb, underlining the relevant aspects for our analysis.

### 6.3.1 Charged track reconstruction

The tracking algorithms search for hits in the LHCb tracking system (VELO, TT, IT and OT) and combine them to form particle trajectories. According to the reconstructed trajectory, several classes of tracks can be defined in LHCb [46] (see also fig. 6.2):

**Long (L) tracks** have been reconstructed using hits through all the LHCb tracking devices, from the VELO to the T (Tracking) stations. They have in general good momentum and impact parameter resolution and are therefore the most useful (and used) for physics analysis.

**Upstream (U) tracks** traverse only the VELO and TT (Trigger Tracker) stations. They are typically low momentum tracks that do not traverse the magnet.

**Downstream (D) tracks** have hits only in the TT and T stations. They may come from the decay of a $K^0_S$ or a $\Lambda(1115)$, in case they decay after the VELO.

**VELO tracks** are measured only in the VELO. These are typically backward or large angle tracks that are used for primary vertex reconstruction.

**T tracks** have hits only in the T stations, and are mainly produced in secondary interactions. However they are still useful for the global pattern recognition in the RICH detector.

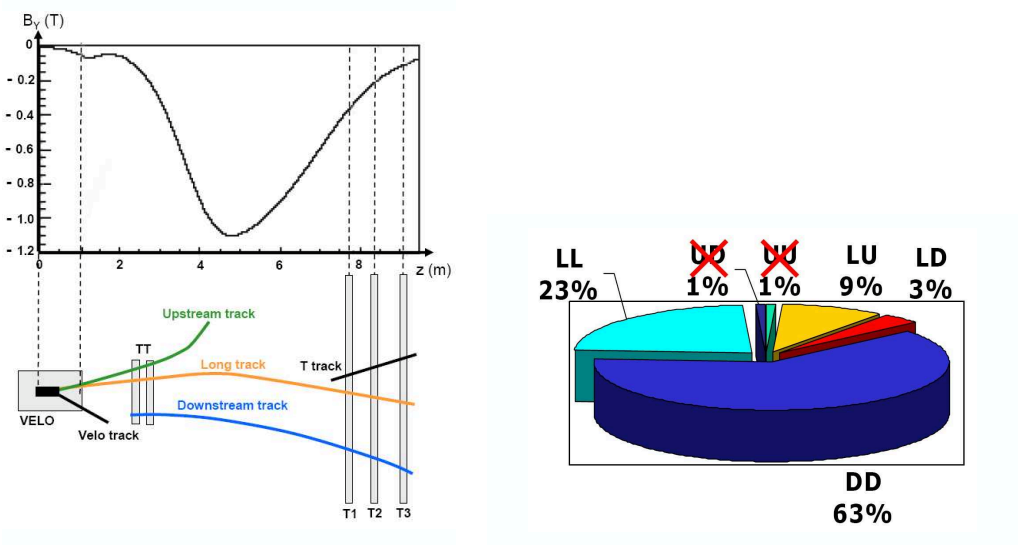



Figure 6.2: *Left: a scheme that illustrates the various LHCb track types, according to the subdetectors they traverse. For reference the main $B$ field component ($B_y$) is plotted above as a function of the $z$ coordinate. Picture from [46]. Right: track composition of the $\Lambda(1115)$ candidates, in events where all true signal tracks have been associated to reconstructed tracks.*

Normally only long tracks are used in physics analysis. We will follow this convention for the reconstruction of the $\Lambda(1670)$. However, this turns out to be insufficient for the $\Lambda(1115)$ reconstruction. An average momentum $\Lambda$ (40 GeV/$c$) travels about 3 m before decaying. It may therefore decay outside the VErtex LOcator (VELO), or even after the tracking stations. We find that 14% of $\Lambda(1115)$ generated within LHCb acceptance are lost for reconstruction since they interact with the detector material before decaying (see section 6.4.1). In order to increase the efficiency we will therefore use also tracks that are not normally used for physics analysis, i.e. upstream and downstream tracks. One can therefore classify reconstructed $\Lambda(1115)$ according to their track composition. We will consider the following categories: LL, DD, LU and LD. In fig. 6.2 the distribution of the origin of the $\Lambda(1115)$ candidates, in events where all true signal tracks have been associated to reconstructed tracks, is shown. The contribution of UU and UD combinations is not significant and they will not be used in the following.

### 6.3.2 Photon reconstruction

Photons are reconstructed and identified as ECAL clusters that are not associated to a charged track (they are therefore defined as neutral). For each photon candidate, an evaluation of its energy and position is given. Several effects are taken into account,

including the energy loss in the material before and between the ECAL modules, and the shape of the electromagnetic shower [108].

As neutral particles do not leave hits in the tracking system, it is impossible to reconstruct their direction. Each photon origin is therefore set to a point that is considered the origin of the detector, and is located in the middle of the VELO. The origin can be changed by the analysis algorithm according to specific needs, as we will see in section 6.5.5.

## 6.4 Detector and reconstruction performances

According to the number of hits left in each detector one can define whether a track is *reconstructible* by the LHCb software:

- **VELO** tracks must have at least 3 $r$ and 3 $\phi$ hits;
- **T** tracks must have at least 1 $x$ and 1 stereo hit in each station T1-T3;
- a **long** track must be reconstructible as a VELO and T track;
- an **upstream** track must be reconstructible as a VELO track and have at least 3 hits in TT;
- a **downstream** track must be reconstructible as a T track and have at least 3 hits in TT.

Moreover, a VELO or TT track is considered *reconstructed* if at least 70% of its associated hits come from the same generated MC particle, while an upstream or downstream track must have in addition a correct TT hit assigned. For long tracks, both VELO and T segments must be successfully reconstructed.

To evaluate the detector performances, one can use two indicators: the detector and reconstruction efficiencies. Let us define [109]:

$N_{\rm gen}$ : number of generated MC signal events.

$N_{\rm DoI}$ : number of events where the Decay of Interest (DoI) has been found, i.e. *all* particles in the decay chain can be retrieved in the MC truth for that particular event. In general $N_{\rm gen} = N_{\rm DoI}$. However long-lived particles such as the $\Lambda(1115)$ may interact with the detector material before decaying, hence $N_{\rm gen} > N_{\rm DoI}$.

$N_{\prime\rm ble}$ : number of reconstructible events. A DoI is reconstructible if one of the following is true for each final state MC particle:

- if the MC particle comes from a $K^0_S$, it must be reconstructible as a long or downstream track;
- if the MC particle does not come from a $K^0_S$, it must be reconstructible as long if it is charged, or as neutral if it is neutral.

$N_{\prime\rm ed}$ : number of reconstructed events. A DoI is reconstructed if one of the following is true for each final state MC particle:

- if the MC particle comes from a $K^0_S$, it must be reconstructed as a long or downstream track;

Table 6.2: *A list of the data samples chosen for full simulation in the LHCb software (see text for explanation). The detector and simulation efficiencies are given for each channel.*

| Decay | $N_{\rm gen}$ | $N_{\rm DoI}$ | $N_{\prime\rm ble}$ | $N_{\prime\rm ed}$ | $N_{\prime\rm ble\&\prime ed}$ | $\epsilon_{\rm det}$ | $\epsilon_{\rm rec/det}$ |
|---|---|---|---|---|---|---|---|
| $\Lambda_b \to \Lambda(1115)\gamma$, long. | 305500 | 262464 | 5313 | 6359 | 4170 | 0.01 | 0.78 |
| $\Lambda_b \to \Lambda(1670)\gamma$, long. | 279500 | 279500 | 61807 | 72989 | 53966 | 0.10 | 0.87 |
| $\Lambda_b \to \Lambda(1670)\gamma$, trans. | 178500 | 178500 | 39167 | 46129 | 34066 | 0.10 | 0.87 |
| $\Lambda_b \to \Lambda(1670)\gamma$, ph. sp. | 280000 | 280000 | 61891 | 72596 | 53828 | 0.10 | 0.87 |

  - if the MC particle does not come from a $K^0_S$, it must be reconstructed as long if it is charged, or as neutral if it is neutral.

$N_{\prime\rm ble\&\prime ed}$ : number of reconstructible and reconstructed events;

The detection efficiency is given by [46]:

$$\epsilon_{\rm det} = \epsilon^{\theta}_{\rm sig} \frac{N_{\prime\rm ble} \cdot N_{\prime\rm ed}}{N_{\rm gen} \cdot N_{\prime\rm ble\&\prime ed}}$$

where the factor $\epsilon^{\theta}_{\rm sig} = 37.1\%$ takes into account the 400 mrad cut on the true polar angle of the signal $b$-hadron imposed at generator level (see section 6.2).

### 6.4.1 Data samples

In order to assess LHCb performances on polarized radiative $\Lambda_b$ decays, large event samples need to be generated and simulated through the entire LHCb software chain. Since the full generation, tracking and reconstruction takes a fair amount of resources, one has to choose the most promising decay modes, and focus on those. We will therefore study decays of the type:

- $\Lambda_b \to \Lambda(1115)\gamma$, for branching ratio measurements. We have generated about 300k events of this type, with full longitudinal polarization of the $\Lambda_b$[1].
- $\Lambda_b \to \Lambda(1670)\gamma$, for angular asymmetries measurements. We have generated events with: unpolarized (phase space), full longitudinally and full transversally polarized $\Lambda_b$.

A list of the generated events, and of reconstruction performances, is reported in table 6.2. As one can see, the reconstruction and detector efficiencies do not depend on the initial $\Lambda_b$ polarization. The difference between $N_{\rm gen}$ and $N_{\rm DoI}$ for $\Lambda_b \to \Lambda(1115)\gamma$ events gives the fraction ($\sim$ 14%) of $\Lambda(1115)$ which have interacted with the surrounding material before decaying.

For background studies, a sample of 39M $b\bar{b}$ inclusive events has been used. The generation of the generic $b\bar{b}$ sample follows the same steps described in section 6.2 for the generation of the signal sample. Of course in this case all $b\bar{b}$ events are selected from the minimum bias sample.

[1]Unfortunately, when this event sample was generated, the $\Lambda_b$ polarization was still hard-coded in the generation software, and could only be set to longitudinal.

## 6.5 Selection of radiative $\Lambda_b$ decays

Reconstructing radiative $\Lambda_b$ decays is quite challenging since the rates of exclusive radiative penguin decays are of the order of $10^{-5}$–$10^{-6}$ and the background is significantly high. The most critical background source is given by $b\bar{b}$ events, since they are characterized by high charged and neutral multiplicities, and they are obviously favored at trigger level. Particularly dangerous for the reconstruction of $\Lambda_b \to \Lambda(1115)\gamma$ decays are events where a prompt $\Lambda(1115)$ has been formed, or created in a secondary interaction. Also the background from minimum bias interactions can be significant, but we assume here that this can be controlled at trigger level.

We will now discuss in details the selection strategy for radiative $\Lambda_b$ decays. Since the reconstruction procedures for the decays (6.1) and (6.2) is quite similar, we will describe the selection criteria for both channels in parallel, and will state the differences when needed. We also remark that no particular procedure is applied to optimize the various selection criteria, whose values have been chosen to suppress $b\bar{b}$ background events while keeping the highest possible efficiency on signal events.

The list of all selection criteria that will be described in the following paragraphs can be found for reference in tables 6.3 and 6.4 for $\Lambda_b \to \Lambda(1115)\gamma$ and $\Lambda_b \to \Lambda(1670)\gamma$ decays, respectively. To (hopefully) improve the readability of this section, only the most relevant distributions are shown here. The remaining plots can be found in appendix 6.A at the end of this chapter.

### 6.5.1 Charged particle identification

The first step of a selection is normally to assign a particle identification (PID) to the reconstructed tracks. The LHCb subsystems involved in particle identification are the Calorimeters (which identify hadrons, electrons and photons, and also $\pi^0$, using the decay $\pi^0 \to \gamma\gamma$), the RICH detector (for charged tracks) and the muon system (evidently, for muons). For each track, a probability to belong to a certain particle ($e$, $\mu$, proton, pion or kaon) is given, based on the information from the relevant subsystem(s) [46]. A Delta Log-Likelihood (DLL) function is used then to compare different hypotheses and allows one to discriminate the wrong from the correct PID assignment:

$$\Delta \ln \mathcal{L}_{AB} = \ln \mathcal{L}_A - \ln \mathcal{L}_B$$

where $\mathcal{L}_A$, or $\mathcal{L}_B$ are the likelihood functions describing the probability that the track has been left by particle $A$, or $B$. The selection of tracks is non-exclusive, i.e. tracks can be assigned more than one particle type. The DLL function tends to be positive for correctly identified tracks.

In this analysis the final states can be pions, protons, or kaons. All charged tracks are considered as possible pion candidates. Proton and kaon candidates are required to have the appropriate DLLs greater than certain values:

- $\Lambda(1115) \to p\pi$ reconstruction. A charged track is considered a proton if:
  - $\text{DLL}_{p\pi} > 6$ and $\text{DLL}_{pK} > 4$, for long tracks;
  - $\text{DLL}_{p\pi} > 10$ and $\text{DLL}_{pK} > 8$, for downstream tracks;
  - $\text{DLL}_{p\pi} > 6$ and $\text{DLL}_{pK} > 0$, for upstream tracks.
- $\Lambda(1670) \to pK$ reconstruction. A charged track is considered:

- a proton, if $\mathrm{DLL}_{p\pi} > 5$ and $\mathrm{DLL}_{pK} > 0$;
- a kaon, if $\mathrm{DLL}_{K\pi} > 5$ and $\mathrm{DLL}_{Kp} > 0$.

The relevant DLLs distributions are shown in figs. 6.11 and 6.17 (app. 6.A) respectively for $\Lambda_b \to \Lambda(1115)\gamma$ and $\Lambda_b \to \Lambda(1670)\gamma$ decays.

### 6.5.2 Charged tracks selection

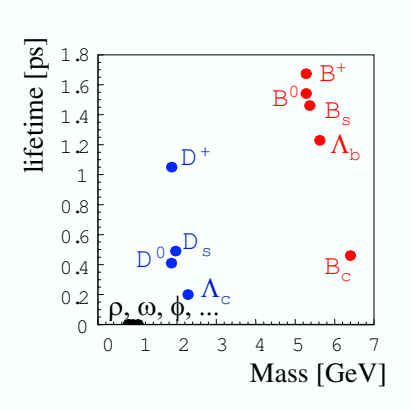



Figure 6.3: *Classification of common hadrons according to their mass and lifetime.*

$b$ hadrons are rather heavy and long-lived, if compared to other lighter flavor states (see fig. 6.3). Typical signatures of $b$-hadrons decay products are the large transverse momentum ($p_T$) and impact parameter (IP). The impact parameter of a given track is defined as the distance between the Primary Vertex (PV) and the point of closest approach of the track to the PV. It can be shown that the mean impact parameter of a decay is proportional to the lifetime of the decaying particle. As a selection criterion, we prefer to use the impact parameter significance (IPS), which is defined as $\mathrm{IPS} = \mathrm{IP}/\sigma_{\mathrm{IP}}$, therefore taking also into account the error $\sigma_{\mathrm{IP}}$ on the measurement of IP. If the event contains more than one reconstructed PV, we will consider the smallest IP.

The charged tracks selection is therefore completed by requiring:

- $\Lambda(1115) \to p\pi$ reconstruction.
  Proton candidates must have:
  - $p_T > 1600$ MeV/$c$ and IPS $> 4$, for long tracks;
  - $p_T > 2500$ MeV/$c$ and IPS $> 3$, for downstream tracks;
  - $p_T > 500$ MeV/$c$ and IPS $> 4$, for upstream tracks.

  Pion candidates must have:
  - $p_T > 300$ MeV/$c$ and IPS $> 4$, for long tracks;
  - $p_T > 350$ MeV/$c$ and IPS $> 3$, for downstream tracks;
  - $p_T > 250$ MeV/$c$ and IPS $> 4$, for upstream tracks.
- $\Lambda(1670) \to pK$ reconstruction. Charged tracks are required to have $p_T > 600$ MeV/$c$ and IPS $> 3$.

The distributions of the charged tracks transverse momentum can be found in app. 6.A, fig. 6.12 ($\Lambda(1115)$) and 6.18 ($\Lambda(1670)$), and the impact parameter significance distributions in app. 6.A, fig. 6.13 ($\Lambda(1115)$) and 6.19 ($\Lambda(1670)$).

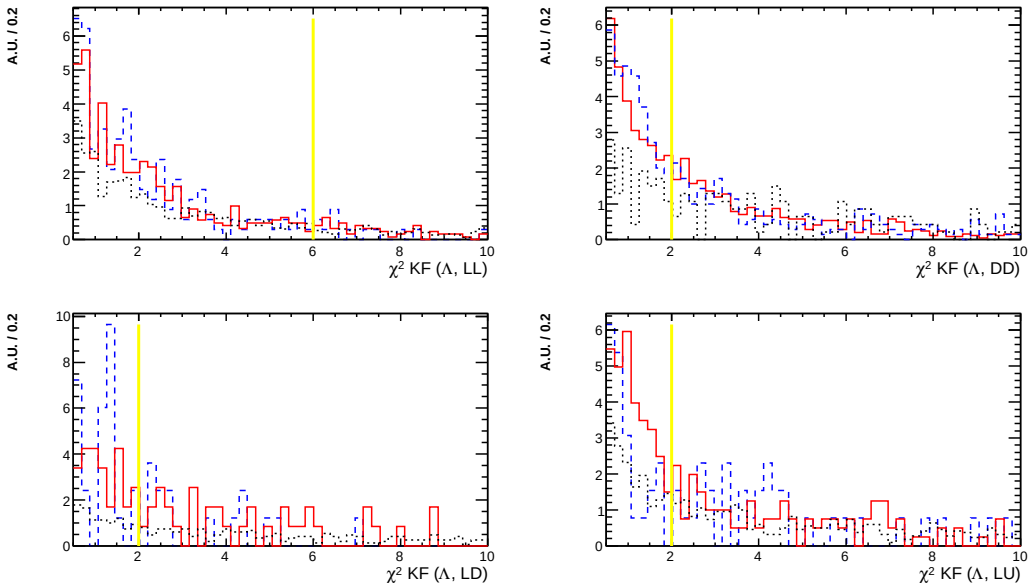



Figure 6.4: *Distribution of the $\chi^2$ of $\Lambda(1115)$ candidates for various track combinations (LL, DD, LD and UL). The red (solid) histogram contains signal events, the blue (dashed) histogram $b\bar{b}$ events where the reconstructed candidate has been associated to a true $\Lambda(1115)$, and the black (dotted) histogram $b\bar{b}$ events with a fake reconstructed $\Lambda(1115)$ candidate. The yellow lines represent the cut values used in the $\Lambda(1115)$ reconstruction described in section 6.5.3.*

### 6.5.3 The $\Lambda$ reconstruction

To reconstruct the $\Lambda$ candidate, all pairs formed by a proton and a pion/kaon candidate (that have survived the previous steps) are combined. Tracks are required to come from a common vertex by discriminating on the $\chi^2$ of a vertex fit. No mass constraint is applied on the $\Lambda$ mass. The $\chi^2$ from the vertex fit can be effectively used to discriminate true from fake $\Lambda(1115)$, as can be seen in fig. 6.4.

The $\Lambda$ candidates are then selected by requiring that the reconstructed invariant mass be within a mass window $\Delta m$ around the nominal mass. Additional requirements to refine the selection are applied on the transverse momentum and impact parameter significance of the reconstructed $\Lambda$ candidate. The relevant distributions can be found in app. 6.A, fig. 6.14 and 6.15 for $\Lambda(1115)$ candidates, and fig. 6.18, 6.19, and 6.20 for $\Lambda(1670)$ candidates.

To summarize, we require:

- $\Lambda(1115) \to p\pi$ reconstruction.
  - $\chi^2 < 6$, $p_T > 500$ MeV/$c$, IPS $> 4$ and $\Delta m < 6$ MeV/$c^2$ for $\Lambda(1115)$ candidates from LL combinations;
  - $\chi^2 < 2$, $p_T > 2000$ MeV/$c$, IPS $> 3$ and $\Delta m < 11$ MeV/$c^2$ for $\Lambda(1115)$ candidates from DD combinations;

  - $\chi^2 < 2$, $p_T > 1500$ MeV/$c$, and $\Delta m < 6$ MeV/$c^2$ for $\Lambda(1115)$ candidates from LD combinations;
  - $\chi^2 < 2$, $p_T > 500$ MeV/$c$, IPS $> 4$ and $\Delta m < 27$ MeV/$c^2$ for $\Lambda(1115)$ candidates from UL combinations.

- $\Lambda(1670) \to pK$ reconstruction: $\chi^2 < 6$, $p_T > 1500$ MeV/$c$, IPS $> 4$ and $\Delta m < 100$ MeV/$c^2$.

The invariant mass distribution of the $\Lambda$ candidates after the previously defined selection is shown in fig. 6.5 and 6.6. In $\Lambda_b \to \Lambda(1115)\gamma$ decays the most significant contribution to the background in $b\bar{b}$ events is given by real $\Lambda(1115)$, whereas in $\Lambda_b \to \Lambda(1670)\gamma$ decays the contribution of random combinations from proton-kaon pairs dominates.

### 6.5.4 Photon selection

We have seen that photon candidates are defined as clusters in the electromagnetic calorimeter that have not been associated to a charged track. To effectively suppress low energy $\gamma$ and $\pi^0$, photons are required to have a large transverse momentum. In particular we require

- $\Lambda_b \to \Lambda(1115)\gamma$ reconstruction.
  - $p_T > 3200$ MeV/$c$, for photon candidates in events where a $\Lambda(1115)$ candidate from LL combinations has been found;
  - $p_T > 3400$ MeV/$c$, for photons associated to a $\Lambda(1115)$ DD-candidate;
  - $p_T > 3800$ MeV/$c$, for photons associated to a $\Lambda(1115)$ LD-candidate;
  - $p_T > 3400$ MeV/$c$, for photons associated to a $\Lambda(1115)$ UL-candidate.
- $\Lambda_b \to \Lambda(1670)\gamma$ reconstruction: photon candidates must have $p_T > 2600$ MeV/$c$.

The photon transverse momentum distribution can be found in figs. 6.16 and 6.20 (in app. 6.A) respectively for $\Lambda_b \to \Lambda(1115)\gamma$ and $\Lambda_b \to \Lambda(1670)\gamma$ decays.

### 6.5.5 The $\Lambda_b$ reconstruction

In LHCb photons can only be reconstructed from clusters in the electromagnetic calorimeter, which give a measurement of their energy and position, but are insufficient to define their direction. Therefore we cannot combine the reconstructed $\Lambda$ and photon candidates to form the $\Lambda_b$ vertex as we have done for the $\Lambda$ vertex.

For $\Lambda_b \to \Lambda(1670)\gamma$ decays we can simply assume that the production and decay vertex of the $\Lambda(1670)$ coincide. The photon origin will therefore be considered the $\Lambda(1670)$ vertex. The $\Lambda_b$ production vertex is chosen as the primary vertex with minimum $\Lambda_b$ impact parameter. Therefore the angle $\theta_B$ between the momentum and the flight direction of the reconstructed $\Lambda_b$ should be very small. Such a requirement is very effective in suppressing $b\bar{b}$ background (see fig. 6.20 in app. 6.A). $\Lambda_b$ candidates are also required to have a large flight distance significance (FS).

To treat $\Lambda_b$ decays into a long-lived particle as the $\Lambda(1115)$ and a photon, we developed a special algorithm, which takes as input the reconstructed $\Lambda(1115)$ direction and a primary vertex. An unconstrained vertex fit is then performed, for all reconstructed primary

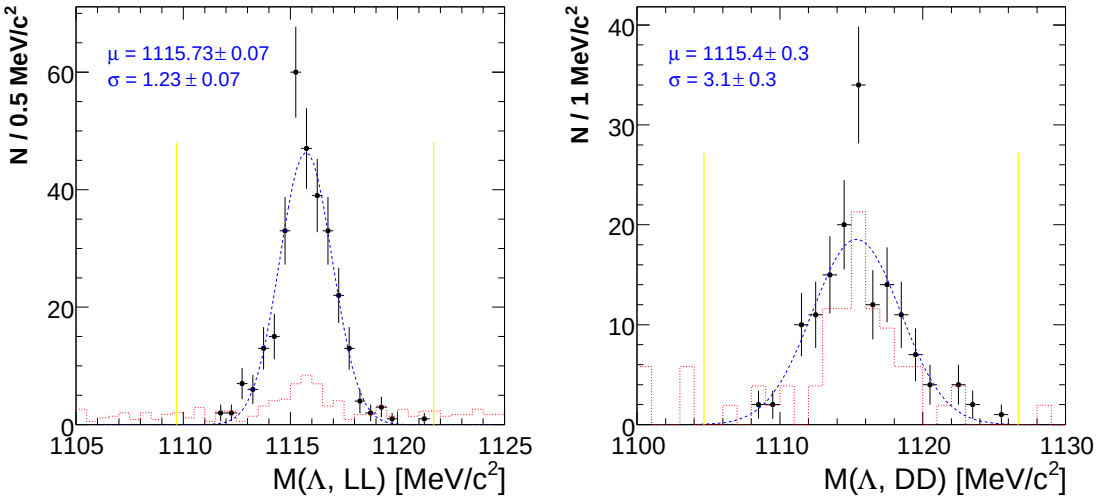



Figure 6.5: *Mass distributions of selected $\Lambda(1115)$ candidates (points with error bars), from LL (left) and DD (right) combinations). The blue dashed curve is a gaussian fit of the signal mass distribution for $\Lambda(1115)$ reconstructed decays. The red dotted histogram contains selected $b\bar{b}$ events (normalized to the total number of selected signal events). The yellow vertical lines represent the mass window cut.*

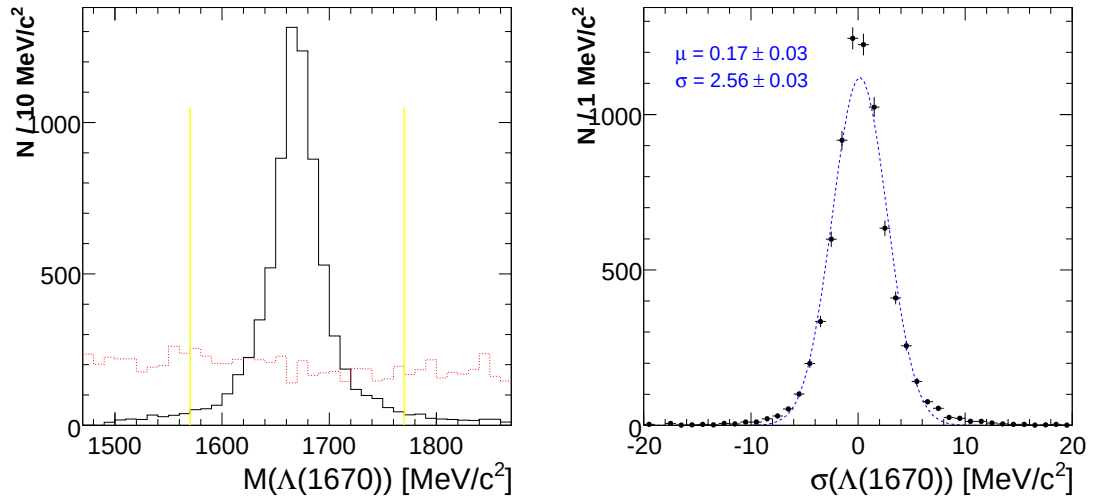



Figure 6.6: *Left: Mass distributions of selected $\Lambda(1670)$ candidates (black solid histogram). The red dotted histogram contains selected $b\bar{b}$ events (normalized to the total number of selected signal events). The yellow vertical lines represent the mass window cut. Right: $\Lambda(1670)$ mass resolution (difference between the reconstructed and generated mass). See section 6.5.6 for details.*

vertices, to find the vertex that is pointed to by the $\Lambda(1115)$ direction. The primary vertex which gives the minimum $\chi^2$ from the fit is chosen as the $\Lambda(1115)$ production vertex. As can be seen in fig. 6.7, the $\chi^2$ can be effectively used to discriminate the signal primary vertex (associated to the true $\Lambda_b$) from fakes. Requiring a minimum $\chi^2$ can also be used as a selection requirement for background rejection, especially for LL and UL combinations. The flight distance of the $\Lambda_b$ ($\sim$ 5 mm for average momentum $\Lambda_b$) is considered to be negligible if compared to the $\Lambda(1115)$ decay length (about 3 m for average momentum $\Lambda(1115)$). The $\Lambda$ flight distance (FD) and its significance are also used as a selection criterion.

Other selection requirements are the $\Lambda_b$ mass window $\Delta m$ and the transverse momentum. Also the projection of the photon momentum on the $\Lambda_b$ candidate flight direction is found to be very useful in suppressing $b\bar{b}$ background (see app. 6.A, figs. 6.16 and 6.20).

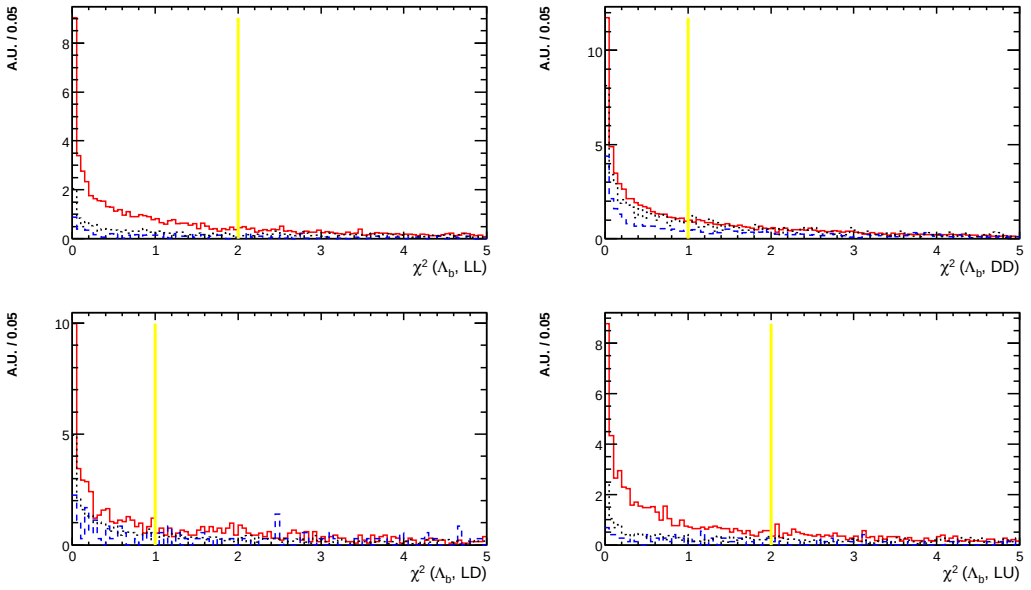



Figure 6.7: $\chi^2$ *(from the $\Lambda_b$ vertex fit for $\Lambda_b \to \Lambda(1115)\gamma$ decays) distribution for various combinations (LL, DD, LD and UL) of $\Lambda(1115)$ candidates. The red (solid) histogram shows the $\chi^2$ from fits where the signal primary vertex (associated to the true $\Lambda_b$) has been used, the blue (dashed) histogram contains the $\chi^2$ distribution from the other vertices. The black (dotted) histogram contains the minimum $\chi^2$ distribution from $b\bar{b}$ events. The yellow lines represent the cut values used in the $\Lambda(1115)$ reconstruction described in section 6.5.5.*

To summarize, we require:

- $\Lambda_b \to \Lambda(1115)\gamma$ reconstruction.
  - $\Lambda(1115)$ candidates from LL combinations: FS $> 4$;
    photon candidates: $p_T$ (in $\Lambda_b$ direction)$\in$ [2250,3000] MeV/$c$;
    $\Lambda_b$ candidates: $\chi^2 < 2$, $p_T > 2500$ MeV/$c$, $\theta_B < 0.15$ and $\Delta m < 300$ MeV/$c^2$;
  - $\Lambda(1115)$ candidates from DD combinations: FD$> 300$ cm;

photon candidates: $p_T$ (in $\Lambda_b$ direction)$\in$ [2250,3000] MeV/$c$;
$\Lambda_b$ candidates: $\chi^2 < 1$, $p_T >$ 2000 MeV/$c$, $\theta_B <$ 0.15 and $\Delta m <$ 300 MeV/$c^2$;

- $\Lambda(1115)$ candidates from LD combinations: no FS or FD requirement;
  photon candidates: $p_T$ (in $\Lambda_b$ direction)$\in$ [2250,3000] MeV/$c$;
  $\Lambda_b$ candidates: $\chi^2 < 1$, $p_T >$ 1000 MeV/$c$, $\theta_B <$ 0.15 and $\Delta m <$ 300 MeV/$c^2$;
- $\Lambda(1115)$ candidates from UL combinations: FS $>$ 4;
  photon candidates: $p_T$ (in $\Lambda_b$ direction)$\in$ [2250,3000] MeV/$c$;
  $\Lambda_b$ candidates: $\chi^2 < 1$, $p_T >$ 500 MeV/$c$, $\theta_B <$ 0.15 and $\Delta m <$ 300 MeV/$c^2$;

- $\Lambda_b \to \Lambda(1670)\gamma$ reconstruction:
  photon candidates: $p_T$ (in $\Lambda_b$ direction)$\in$ [1600,2800] MeV/$c$;
  $\Lambda_b$ candidates: $p_T >$1500 MeV/$c$, $\theta_B <$ 0.01, FS $>$ 2 and $\Delta m <$ 200 MeV/$c^2$.

The most effective selection criteria for background rejection are the requirements on particle identification, transverse momentum and impact parameter significance of the final states (as one can easily convince oneself by looking at the relevant distributions), as well as the mass window requirements. For $\Lambda_b \to \Lambda(1670)\gamma$ decays, the requirement on small angles between the $\Lambda_b$ momentum and flight direction is also very powerful. The $\chi^2$ cuts are useful to discriminate events where a true $\Lambda_b$ or $\Lambda$ have been reconstructed (and therefore to enhance signal purity).

### 6.5.6 Mass resolutions

The mass distributions of the selected $\Lambda_b$ candidates are shown in fig. 6.8. The central value $\mu$ and standard deviation $\sigma$ of the reconstructed $\Lambda_b$ are found to be:

| Decay | $\mu_{\Lambda_b}$ [MeV/$c^2$] | $\sigma_{\Lambda_b}$ [MeV/$c^2$] |
|---|---|---|
| $\Lambda_b \to \Lambda(1115)\gamma$ (LL) | 5615.9 $\pm$ 3.9 | 62.2 $\pm$ 3.5 |
| $\Lambda_b \to \Lambda(1670)\gamma$ | 5611.3 $\pm$ 1.3 | 74.9 $\pm$ 1.2 |

The $\Lambda_b$ mass resolution is similar to those of other $B$ radiative decays (64 and 65 MeV/$c^2$ respectively for $B^0 \to K^{*0}\gamma$ and $B_s^0 \to \phi\gamma$ decays [110]). The small offset (about 10 MeV/$c^2$) in the reconstructed $\Lambda_b$ mass with respect to the true $\Lambda_b$ mass (5624 MeV/$c^2$) is due to the photon calibration energy in the electromagnetic calorimeter. This will be fixed when real data become available.

The mass resolution of the $\Lambda(1115)$ can be read off fig. 6.5. For the $\Lambda(1670)$ mass resolution one has to separate the contributions of the intrinsic width of the resonance, and the detector resolution. To get the latter, we apply a gaussian fit to the difference between the reconstructed and generated mass (see fig. 6.6), and obtain $\sigma$ = 2.56 $\pm$ 0.03 MeV/$c^2$. An equivalent method would be to fit the $\Lambda(1670)$ mass distribution with the convolution of a gaussian (for the detector resolution) and a Breit-Wigner distribution (for the intrinsic width).

To summarize, we obtain the following results for the reconstruction of the $\Lambda(X)$ baryon:

| Decay | $\mu_{\Lambda(X)}$ [MeV/$c^2$] | $\sigma_{\Lambda(X)}$ [MeV/$c^2$] |
|---|---|---|
| $\Lambda_b \to \Lambda(1115)\gamma$ (LL) | 1115.73 $\pm$ 0.07 | 1.23 $\pm$ 0.07 |
| $\Lambda_b \to \Lambda(1115)\gamma$ (DD) | 1115.4 $\pm$ 0.3 | 3.1 $\pm$ 0.3 |
| $\Lambda_b \to \Lambda(1670)\gamma$ | 1670.17 $\pm$ 0.03 | 2.56 $\pm$ 0.03 |

Table 6.3: *List of the selection criteria employed in the reconstruction of* $\Lambda_b \to \Lambda(1115)\gamma$ *decays.*

| **Proton** | | **L** | **D** | **U** |
|---|---|---|---|---|
| $\text{DLL}_{p\pi}$ | $>$ | 6 | 10 | 6 |
| $\text{DLL}_{pK}$ | $>$ | 4 | 8 | 0 |
| $p_T$ [MeV/$c$] | $>$ | 1600 | 2500 | 500 |
| IPS | $>$ | 4 | 3 | 4 |
| **Pion** | | **L** | **D** | **U** |
| $p_T$ [MeV/$c$] | $>$ | 300 | 350 | 250 |
| IPS | $>$ | 4 | 3 | 4 |

| **$\Lambda(1115)$** | | **LL** | **DD** | **LD** | **LU** |
|---|---|---|---|---|---|
| $\Delta m$ [MeV/$c^2$] | $<$ | 6 | 11 | 6 | 27 |
| $\chi^2$ | $<$ | 6 | 2 | 2 | 2 |
| $p_T$ [MeV/$c$] | $>$ | 500 | 2000 | 1500 | 500 |
| IPS | $>$ | 4 | 3 | - | 4 |
| FS (FD) | $>$ | 4 | 300 (FD) | - | 5 |

| **Photon** | | **LL** | **DD** | **LD** | **LU** |
|---|---|---|---|---|---|
| $p_T$ (in $\Lambda_b$ dir.) [MeV/$c$] | $\in$ | [2250,3000] | [2250,3000] | [2250,3000] | [2250,3000] |
| $p_T$ [MeV/$c$] | $>$ | 3200 | 3400 | 3800 | 3400 |

| **$\Lambda_b$** | | **LL** | **DD** | **LD** | **LU** |
|---|---|---|---|---|---|
| $\Delta m$ [MeV/$c^2$] | $<$ | 300 | 300 | 300 | 300 |
| $\chi^2$ | $<$ | 2 | 1 | 1 | 2 |
| $p_T$ [MeV/$c$] | $>$ | 2500 | 2000 | 1000 | 500 |
| $\theta_B$ | $<$ | 0.15 | 0.15 | 0.15 | 0.15 |

Table 6.4: *List of the selection criteria for* $\Lambda_b \to \Lambda(1670)\gamma$ *decays.*

| **Kaon** | | | **Proton** | | | **$\Lambda(1670)$** | | |
|---|---|---|---|---|---|---|---|---|
| $\text{DLL}_{K\pi}$ | $>$ | 5 | $\text{DLL}_{p\pi}$ | $>$ | 5 | $\Delta m$ [MeV/$c^2$] | $<$ | 100 |
| $\text{DLL}_{Kp}$ | $>$ | 0 | $\text{DLL}_{pK}$ | $>$ | 0 | $\chi^2$ | $<$ | 6 |
| $p_T$ [MeV/$c$] | $>$ | 600 | $p_T$ [MeV/$c$] | $>$ | 600 | $p_T$ [MeV/$c$] | $>$ | 1500 |
| IPS | $>$ | 3 | IPS | $>$ | 3 | IPS | $>$ | 4 |

| **Photon** | | | **$\Lambda_b$** | | |
|---|---|---|---|---|---|
| $p_T$ (in $\Lambda_b$ dir.) [MeV/$c$] | $\in$ | [1600,2800] | $\Delta m$ [MeV/$c^2$] | $<$ | 200 |
| | | | $\theta_B$ | $<$ | 0.01 |
| $p_T$ [MeV/$c$] | $>$ | 2600 | $p_T$ [MeV/$c$] | $>$ | 2000 |
| | | | FS | $>$ | 2 |

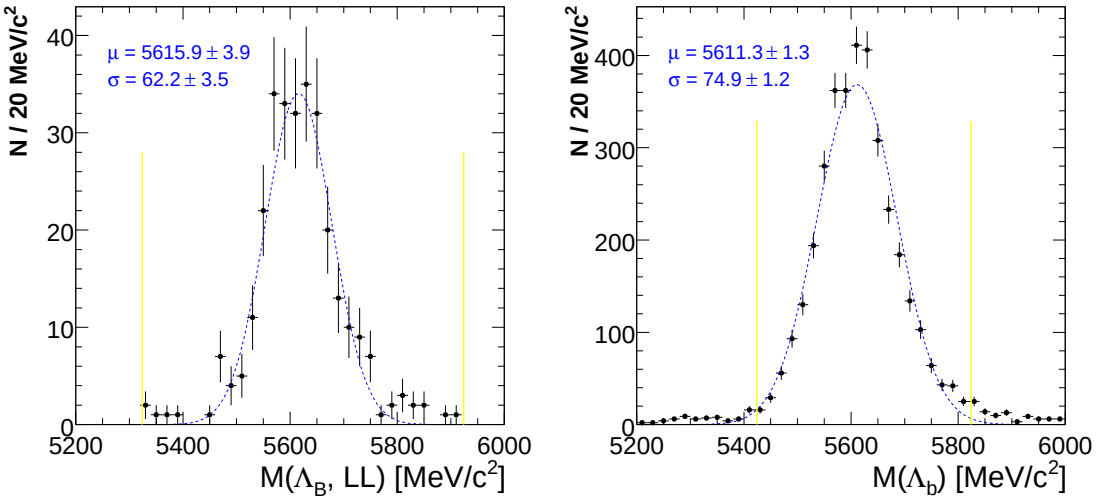



Figure 6.8: *Mass distributions of selected $\Lambda_b$ candidates from the decays $\Lambda_b \to \Lambda(1115)\gamma$ (left, from LL combinations) and $\Lambda_b \to \Lambda(1670)\gamma$ (right). The blue dashed curve is a gaussian fit of the signal mass distribution. The yellow vertical lines represent the mass window cut.*

### 6.5.7 Selection algorithm performances

To assess the performances of the described selection algorithms from radiative $\Lambda_b$ decays we still need to add some more definitions:

$N_{\rm sel}$ : number of offline selected events;

$N_{\rm L0}$ : number of selected events passing the L0 trigger;

$N_{\rm L1}$ : number of selected events passing the L0 and L1 trigger;

$N_{\rm HLT}$ : number of selected events passing the L0, L1 and HLT Generic trigger;

The total signal efficiency can be written as [46]:

$$\epsilon_{\rm tot} = \epsilon_{\rm det} \times \epsilon_{\rm rec/det} \times \epsilon_{\rm sel/rec} \times \epsilon_{\rm trg/sel} \tag{6.3}$$

where:

- $\epsilon_{\rm sel/rec} = N_{\rm sel}/N_{\rm red}$ is the offline selection efficiency on reconstructed events;
- $\epsilon_{\rm trg/sel} = N_{\rm HLT}/N_{\rm sel}$ is the trigger efficiency on selected events. For a complete description of the LHCb trigger system, see [55]. For completeness, we also give the various contributions to the trigger efficiency in table 6.5, where:
  - $\epsilon_{\rm L0/sel} = N_{\rm L0}/N_{\rm sel}$ is the L0 trigger efficiency on offline selected events;
  - $\epsilon_{\rm L1/L0} = N_{\rm L1}/N_{\rm L0}$ is the L1 trigger efficiency on offline selected events passing the L1 trigger;
  - $\epsilon_{\rm HLT/L1} = N_{\rm HLT}/N_{\rm L1}$ is the HLT Generic trigger efficiency on offline selected events passing the L0 and L1 trigger.

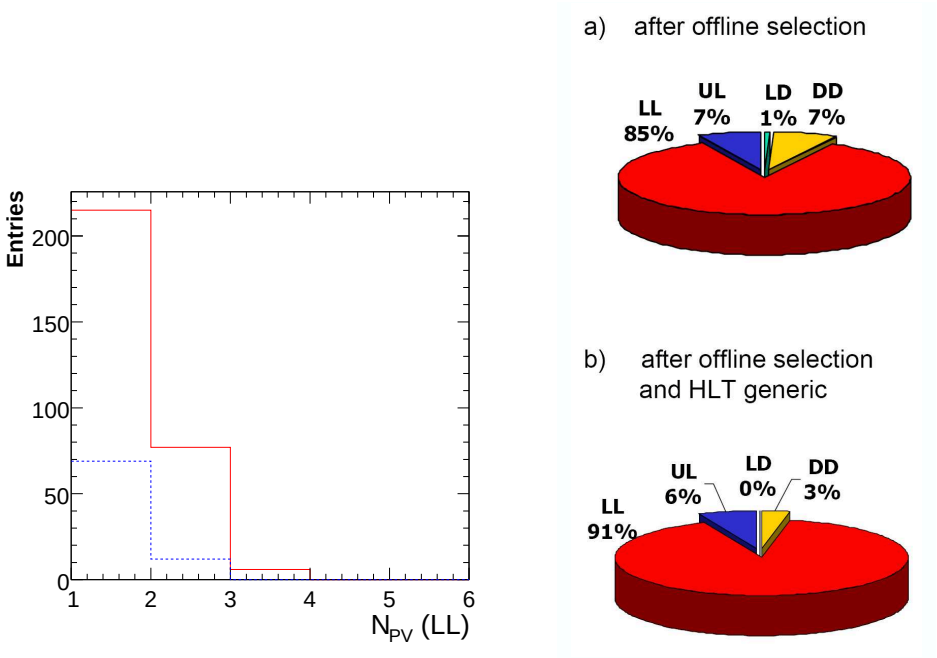



Figure 6.9: *Left: Number of reconstructed primary vertices in selected $\Lambda_b \to \Lambda(1115)\gamma$ events (from LL combinations) before (red solid) and after (blue dashed) the trigger. Right: track composition of $\Lambda(1115)$ candidates, after the offline selection (a), and after trigger and offline selection (b).*

The number of reconstructed primary vertices in selected $\Lambda_b \to \Lambda(1115)\gamma$ events before and after the trigger (L0, L1 and HLT Generic) is shown in fig. 6.9, where the effect of the Pile-Up veto can be seen. The track composition of selected $\Lambda(1115)$ candidates before and after the trigger can also be found in fig. 6.9. As expected (the trigger only reconstructs long tracks), the LL combination dominates (91%). Unfortunately, no exclusive HLT selection exists yet for radiative $\Lambda_b$ decays.

The efficiencies breakdown for radiative $\Lambda_b$ decays can be found in table 6.6.

To set a limit on the expected background level we will now calculate the background to signal ratio for the channels of interest. The expression for the $B/S$ ratio after selection

Table 6.5: *Trigger efficiency breakdown. For explanation, see text.*

| **Decay** | $N_{\text{sel}}$ | $N_{\text{L0}}$ | $N_{\text{L1}}$ | $N_{\text{HLT}}$ | $\epsilon_{\text{L0/sel}}$ | $\epsilon_{\text{L1/L0}}$ | $\epsilon_{\text{HLT/L1}}$ |
|---|---|---|---|---|---|---|---|
| $\Lambda_b \to \Lambda(1115)\gamma$, long. | 416 | 291 | 148 | 95 | 0.70 | 0.51 | 0.64 |
| $\Lambda_b \to \Lambda(1670)\gamma$, long. | 5311 | 3838 | 2534 | 1916 | 0.72 | 0.66 | 0.76 |
| $\Lambda_b \to \Lambda(1670)\gamma$, trans. | 3496 | 2469 | 1530 | 1209 | 0.71 | 0.62 | 0.79 |
| $\Lambda_b \to \Lambda(1670)\gamma$, ph. sp. | 5353 | 3812 | 2415 | 1874 | 0.71 | 0.63 | 0.78 |

Table 6.6: *Reconstruction and selection efficiency summary.*

| **Decay** | $\epsilon_{\rm det}$ | $\epsilon_{\rm rec/det}$ | $\epsilon_{\rm sel/rec}$ | $\epsilon_{\rm trg/sel}$ | $\epsilon_{\rm tot}$ (%) |
|---|---|---|---|---|---|
| $\Lambda_b \to \Lambda(1115)\gamma$, long. | 0.01 | 0.78 | 0.068 | 0.228 | 0.011 |
| $\Lambda_b \to \Lambda(1670)\gamma$, long. | 0.10 | 0.87 | 0.073 | 0.361 | 0.228 |
| $\Lambda_b \to \Lambda(1670)\gamma$, trans. | 0.10 | 0.87 | 0.076 | 0.345 | 0.228 |
| $\Lambda_b \to \Lambda(1670)\gamma$, ph. sp. | 0.10 | 0.87 | 0.074 | 0.350 | 0.225 |

and before any trigger is given by:

$$B/S = \frac{\epsilon^{\theta}_{\rm sig}}{\epsilon^{\theta}_{b\bar{b}}} \cdot \frac{1}{2 f_{\Lambda_b} \mathcal{BR}_{\rm vis}} \cdot \frac{N^{b\bar{b}}_{\rm sel}/N^{b\bar{b}}_{\rm gen}}{N^{\rm sig}_{\rm sel}/N^{\rm sig}_{\rm gen}}$$

where

- $\epsilon^{\theta}_{b\bar{b}}$ = 0.43 is the 400 mrad requirement acceptance for the $b\bar{b}$ sample;
- $f_{\Lambda_b} = 8\%$ is the $b \to \Lambda_b$ production fraction;
- $\mathcal{BR}_{\rm vis}$ is the visible BR for the relevant decay channel.

No event from the 39M $b\bar{b}$ inclusive sample passes the selection requirements for either $\Lambda_b$ decay mode[2]. We will assume a Poissonian distribution for background events which allows us to estimate $N^{b\bar{b}}_{\rm sel} \leq 1.22$ at 90% confidence level. We find $B/S$ ratios less than 42 and 18 at 90% confidence level respectively for $\Lambda_b \to \Lambda(1115)\gamma$ and $\Lambda_b \to \Lambda(1670)\gamma$ decays.

### 6.5.8 Inclusive $b\bar{b}$ background

To get a better understanding of the possible background sources for the decays under study, we analyzed the 39M $b\bar{b}$ inclusive sample with the selection criteria described in tables 6.3 and 6.4, but with a looser requirement on the $\Lambda_b$ mass window $\Delta m_{\rm loose}$ = 500 MeV/$c^2$.

4 events pass the $\Lambda_b \to \Lambda(1115)\gamma$ selection, 3 from DD combinations and 1 from LD combinations. Only one of them passes the L0 trigger:

- $B^+ \to (D^{*0} \to (D^0 \to K^0\pi^+\pi^-\pi^0\pi^0)\pi^0)np$. The reconstructed proton comes from the $B^+$. The pion is a ghost. $\Lambda(1115)$ from LD combinations.
- The reconstructed $\bar{p}$ and $\pi^+$ come from a true $\overline{\Lambda}(1115)$ from a prompt $\Sigma$. The full decay is: $\overline{\Sigma}^0 \to \overline{\Lambda}(1115)\gamma$. This decay evidently has topological and kinematical characteristics similar to decay (6.1). $\Lambda(1115)$ from DD combinations. For completeness, we report also the true $B$ decays in the event:

  $B^- \to (D^{*0} \to (D^0 \to \eta'\pi^0)\gamma)e^-\bar{\nu}$;
  $B^0 \to (D^- \to (\eta \to \pi^0\pi^0\pi^0)\pi^-)(D_s^+ \to (\phi \to K^0_L K^0_S)e^+\nu)$.

[2]The selection requirements have however been tuned using the same 39M $b\bar{b}$ sample, therefore a significant bias might have been introduced.

- Again, the reconstructed $\bar{p}$ and $\pi^+$ come from a true $\Lambda(1115)$ from a prompt $\Xi$. The full decay is $\overline{\Xi}^0 \to \overline{\Lambda}(1115)\pi^0$. From DD combinations. The true $B$ decays in the event are:

$$B^0 \to (D^{*-} \to (\overline{D}^0 \to K^+\pi^-\pi^0)\pi^-)e^+\nu_e;$$
$$\overline{B}^0 \to (D^{*0} \to D^0\pi^0)\pi^+\tau^-\bar{\nu}_\tau.$$

- $B^0 \to (\Sigma_c^0 \to (\Lambda_c^- \to \Lambda(1115)\eta'\pi^+)\pi^-)\overline{\Delta}^0\rho(770)^0$. From DD combinations. The reconstructed $p$ and $\pi^-$ come from the true $\Lambda(1115)$ from the $\Lambda_c$ decay. Passes L0.

No background events have been selected from LL combinations. The $B^+$ event selection (from LD combinations) is due to a reconstruction problem (the reconstructed pion is a ghost), while the remaining 3 events contain a true $\Lambda(1115)$. This last event typology is, as expected, the most dangerous background source for decay (6.1). The L0 accepted event is the only one to contain a true reconstructed $\Lambda(1115)$ from a $B$ decay.

2 events pass the $\Lambda_b \to \Lambda(1670)\gamma$ selection, however none of them passes the L0 trigger:

- $B^- \to (D^{*0} \to (D^0 \to K^-\pi^+\pi^0)\gamma)e^-\bar{\nu}$. The kaon and a pion misidentified as a proton from the $D^0$ decay form the $\Lambda(1670)$.

- $\Lambda_b \to (\Lambda_c^- \to (K^*(892)^+ \to K\pi^0)\bar{p}\,\pi^-)\pi^0\pi^0\rho(770)^+$. The reconstructed kaon comes from the $K^*$ decay, whereas the antiproton comes from the $\Lambda_c^-$ decay.

As expected, the dominant contribution comes from combinatorial background. For both decays we see that a possible source of background is given by $b$-hadron decays with detached secondary vertices (involving for instance $D$ mesons).

## 6.6 BR measurement

For a given decay channel, the annual event yield is given by [46]:

$$S_{\text{year}} = N_{\Lambda_b} \times \mathcal{BR}_{\text{vis}} \times \epsilon_{\text{tot}} \tag{6.4}$$

where:

$N_{\Lambda_b} = L^y_{\text{int}} \times \sigma_{b\bar{b}} \times 2 \times f_{\Lambda_b} = 8 \cdot 10^{10}$ is the number of expected $\Lambda_b$ per year, at an annual nominal integrated luminosity $L^y_{\text{int}} = 2$ fb$^{-1}$ and with an assumed $b\bar{b}$ production cross section of $\sigma_{b\bar{b}}$=500 $\mu$b. The factor 2 takes into account the production of both $\Lambda_b$ and $\bar{\Lambda}_b$ baryons.

$\mathcal{BR}_{\text{vis}}$ is the visible BR for the relevant decay channel. The BRs for the channels of interest can be found in chapter 5, and are of the order of $10^{-5}$–$10^{-6}$.

$\epsilon_{\text{tot}}$ is the total efficiency of detection, reconstruction and selection of signal events, see sections 6.4 and 6.5.7 for details. We will also take into account here a further reduction factor due to a yet to be written HLT exclusive selection. We will assume an efficiency of 90%, as for the HLT exclusive selection of $B_s^0 \to \phi\gamma$ events [111].

We therefore obtain the following event yields for decays involving the first five $\Lambda$ baryons above the $NK$ threshold:

$$S_{\rm year}(\Lambda_b \to (\Lambda(1115) \to p\pi)\gamma) \sim 675$$
$$S_{\rm year}(\Lambda_b \to (\Lambda(1520) \to pK)\gamma) \sim 4270$$
$$S_{\rm year}(\Lambda_b \to (\Lambda(1600) \to pK)\gamma) \sim 2120$$
$$S_{\rm year}(\Lambda_b \to (\Lambda(1670) \to pK)\gamma) \sim 2250$$
$$S_{\rm year}(\Lambda_b \to (\Lambda(1690) \to pK)\gamma) \sim 2250$$

The significance of a BR measurement can be written as:

$$\sigma = \frac{S_{\rm year}}{\sqrt{S_{\rm year} + B_{\rm year}}}$$

where $B_{\rm year}$ is the annual yield of background events. The sensitivity of LHCb to BR measurements after 1 year of data taking can be read off fig. 6.10. If the SM prediction for $\mathcal{BR}(\Lambda_b \to \Lambda(1115)\gamma)$ is correct, LHCb can measure it with at least $4\sigma$ significance. If the $\Lambda(1670)$ and the $\Lambda(1690)$ resonances can be disentangled, the $\mathcal{BR}(\Lambda_b \to \Lambda(1670)\gamma)$ can be measured very precisely ($> 10\sigma$ significance). Similar results can be extrapolated for the other $\Lambda$ resonances which are given above.

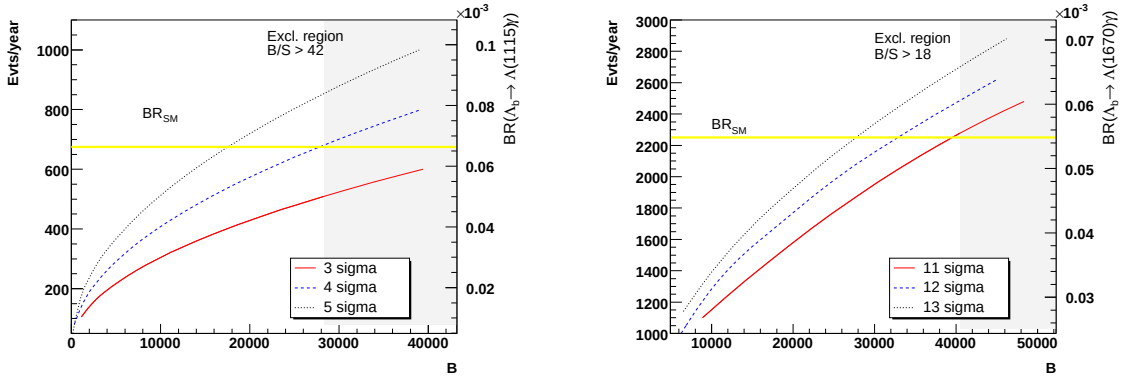



Figure 6.10: *LHCb sensitivity to the measurement of the BR of $\Lambda_b \to \Lambda(1115)\gamma$ (left) and $\Lambda_b \to \Lambda(1670)\gamma$ (right) decays after one year of data taking. The curves show the values of the BR that can be probed at various sigma significance as a function of the background level (B). The grey region is excluded by the estimated $B/S$ ratio. The yellow vertical line is the expected SM BR.*

## 6.7 Conclusions

We have studied the polarized decays $\Lambda_b \to \Lambda(1115)\gamma$ and $\Lambda_b \to \Lambda(1670)\gamma$ in the LHCb environment. The annual signal yield is expected to be 750 (2500) reconstructed events

(after HLT Generic) with background to signal ratio $< 42$ (18) at 90% confidence level for decay 6.1 (6.2). We find that the dominant background contribution is given by events containing a true $\Lambda(1115)$ for decay (6.1), and by combinatorial background for decay (6.2). The reconstruction performances are similar to those of other benchmark channels. BR measurements should be feasible already after 1 year of data taking.

In the next chapter we will use these results to assess LHCb sensitivity to the measurement of the photon polarization in $\Lambda_b \to \Lambda(X)\gamma$ decays.

# Appendix to Chapter 6

## 6.A Distributions

This appendix contains all plots relevant to the event selection of the decays $\Lambda_b \to \Lambda(1115)\gamma$ and $\Lambda_b \to \Lambda(1670)\gamma$, as described in section 6.5. We will use the following convention: all histograms (including the underflow and overflow bins) are normalized to 100. Therefore by integrating over a certain range on the $x$-axis one obtains the percentage of events contained in that interval.

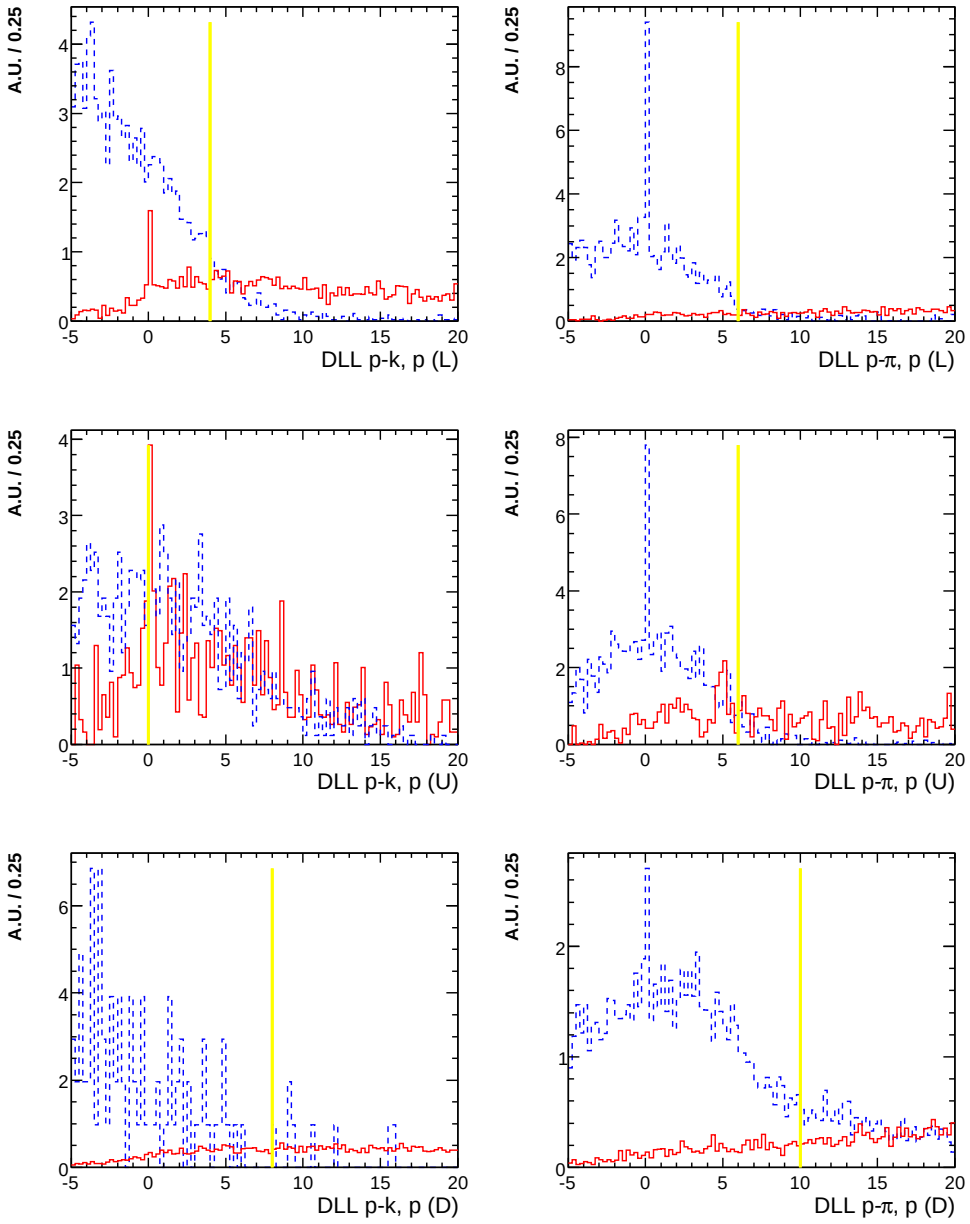



Figure 6.11: *Difference in log-likelihood probability (DLL) between various particle hypothesis for proton candidates in $\Lambda_b \to \Lambda(1115)\gamma$ decays. The red solid histogram corresponds to signal events where the proton has been correctly identified, whereas the blue dashed histogram corresponds to events where a kaon (left) or a pion (right) has been wrongly identified as a proton, in the $b\bar{b}$ inclusive sample (left), and in signal events (right). The vertical yellow lines represent the cut values.*

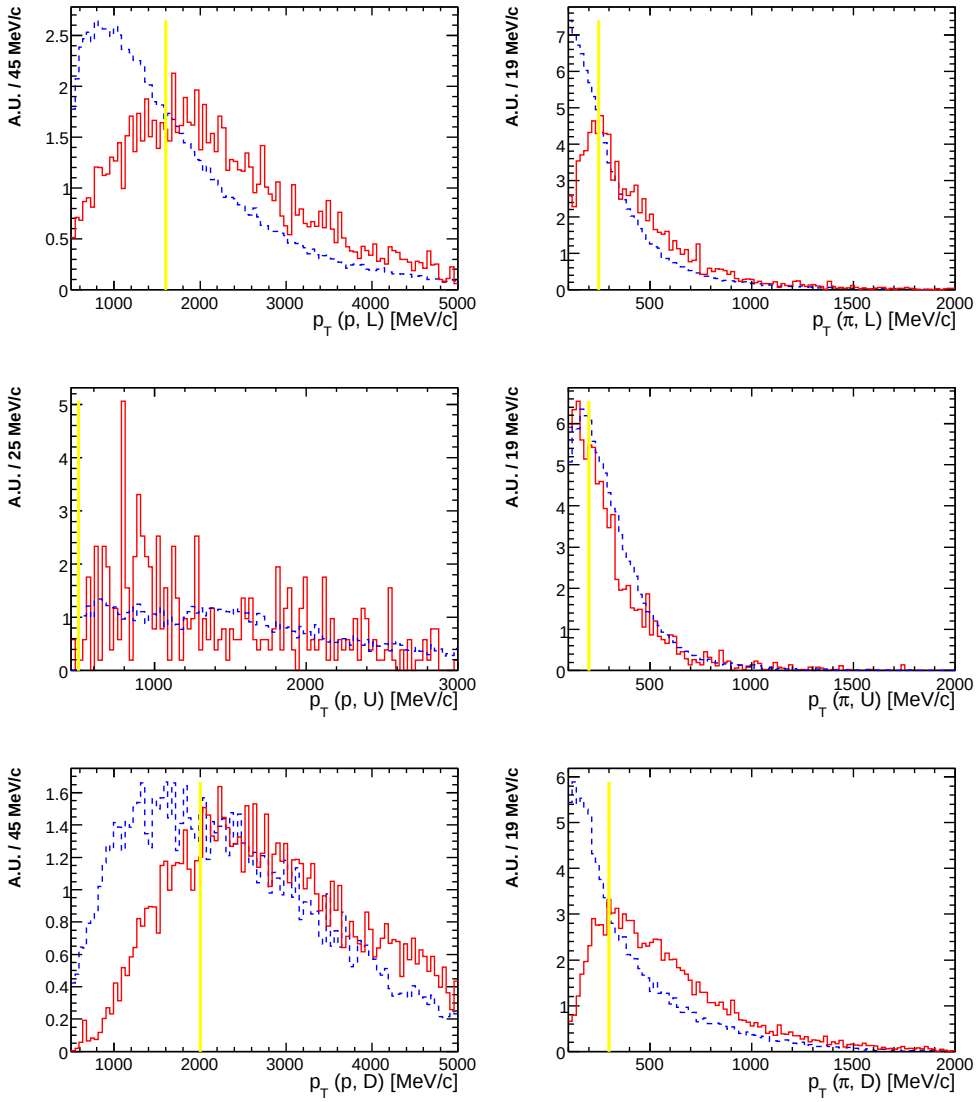



Figure 6.12: *Transverse momentum distribution for reconstructed proton and pion candidates in* $\Lambda_b \to \Lambda(1115)\gamma$ *decays. The red solid histogram corresponds to signal events where all reconstructed tracks have been associated to the true signal particles, while the blue dashed histogram to events from the* $b\bar{b}$ *inclusive sample. The vertical yellow lines represent the cut values.*

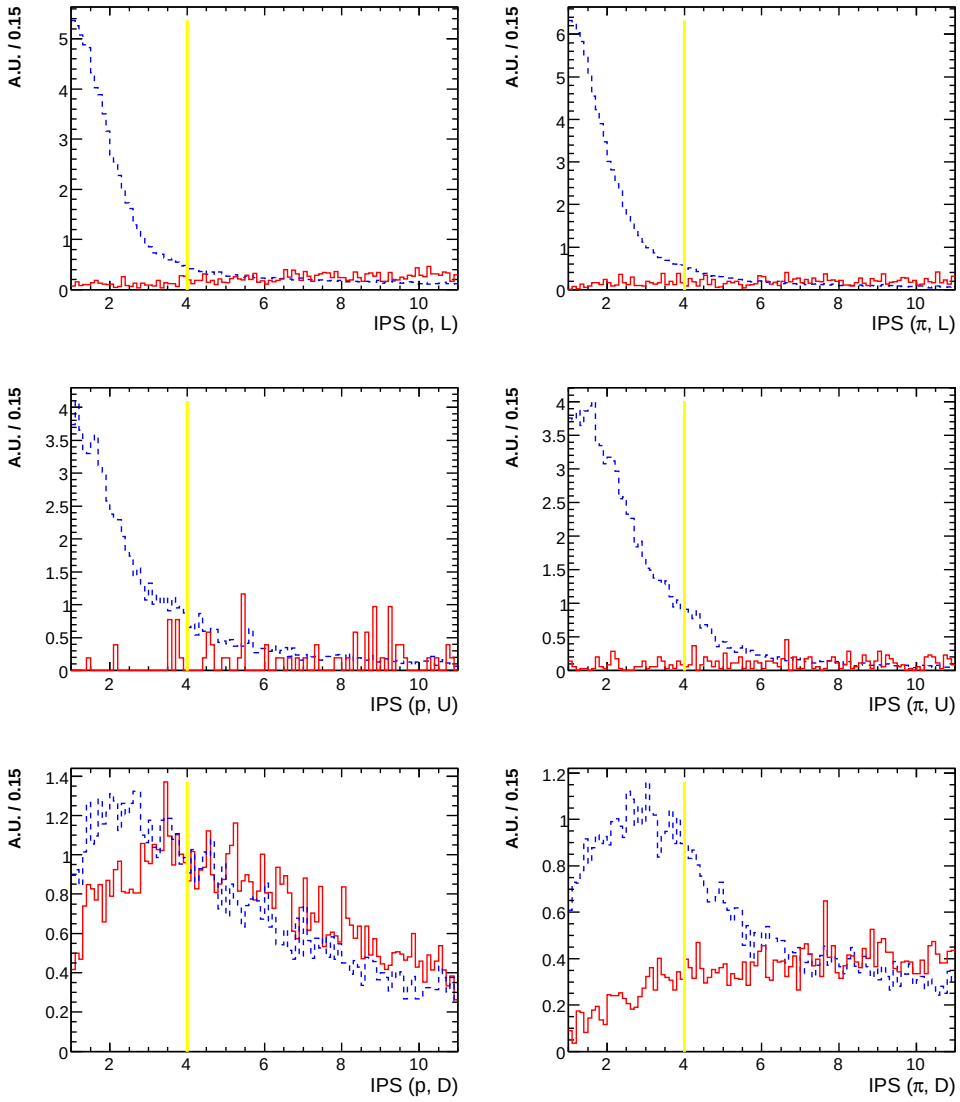



Figure 6.13: *Impact parameter significance (IPS) for reconstructed proton and pion candidates in* $\Lambda_b \to \Lambda(1115)\gamma$ *decays. The red solid histogram corresponds to signal events where all reconstructed tracks have been associated to the true signal particles, while the blue dashed histogram to events from the* $b\bar{b}$ *inclusive sample. The vertical yellow lines represent the cut values.*

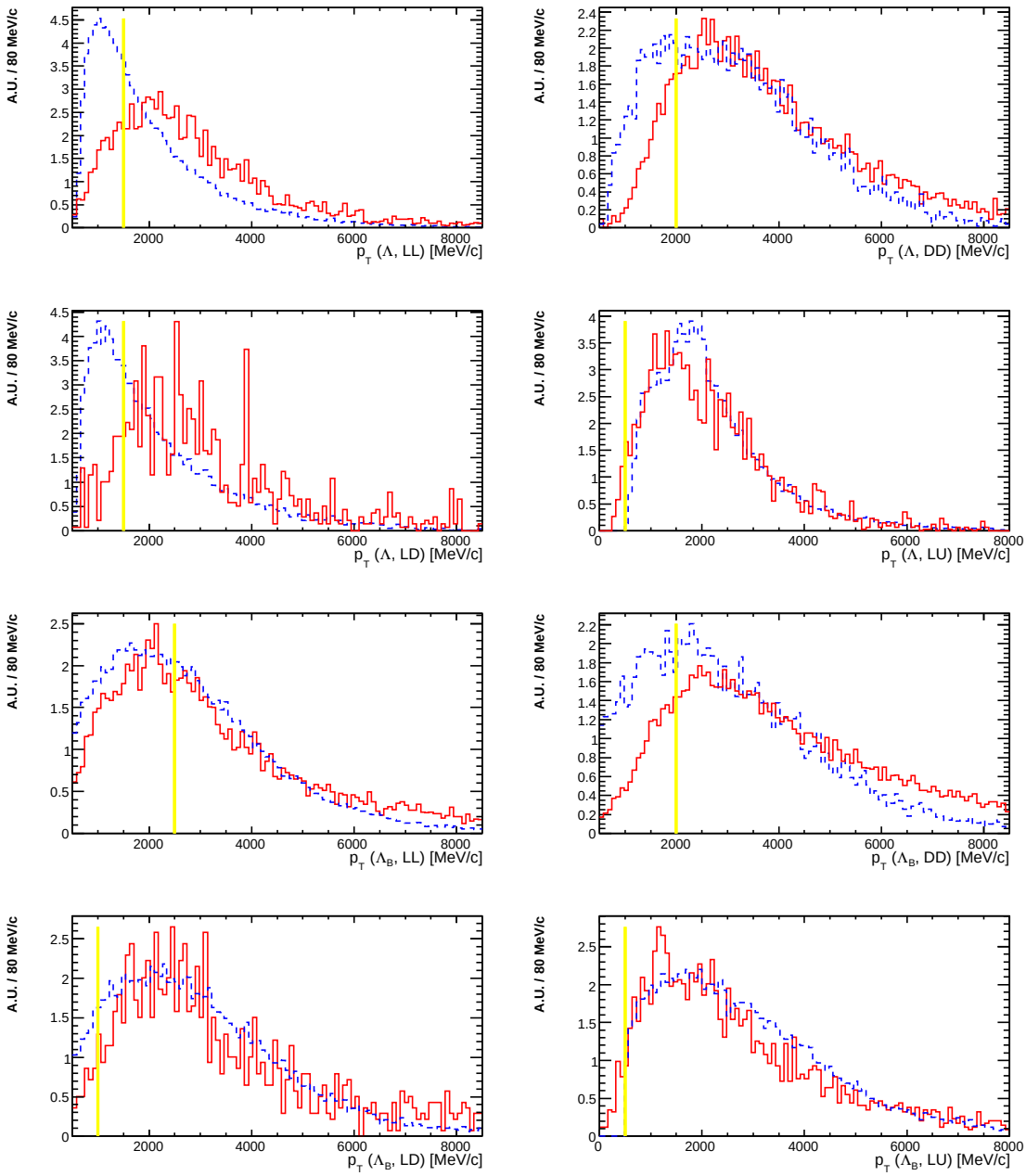



Figure 6.14: *Transverse momentum distribution for reconstructed* $\Lambda$ *and* $\Lambda_b$ *candidates in* $\Lambda_b \to \Lambda(1115)\gamma$ *decays. The red solid histogram corresponds to signal events where all reconstructed tracks have been associated to the true signal particles, while the blue dashed histogram to events from the* $b\bar{b}$ *inclusive sample. The vertical yellow lines represent the cut values.*

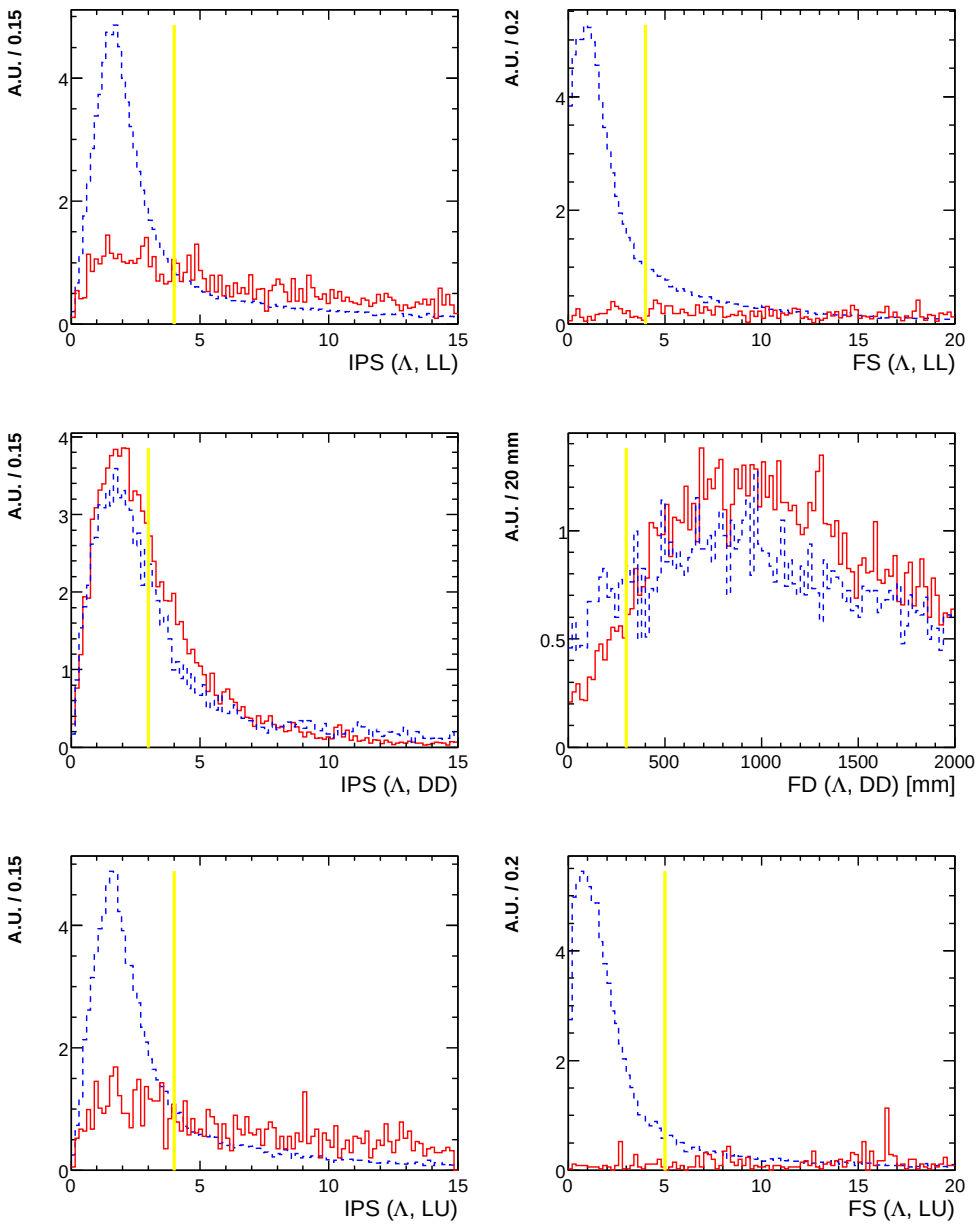



Figure 6.15: *Impact parameter significance (IPS), flight distance (FD) and flight distance significance (FS) distributions for* $\Lambda$ *candidates in* $\Lambda_b \to \Lambda(1115)\gamma$ *decays. The red solid histogram corresponds to signal events where all reconstructed tracks have been associated to the true signal particles, while the blue dashed histogram to events from the* $b\bar{b}$ *inclusive sample. The vertical yellow lines represent the cut values.*

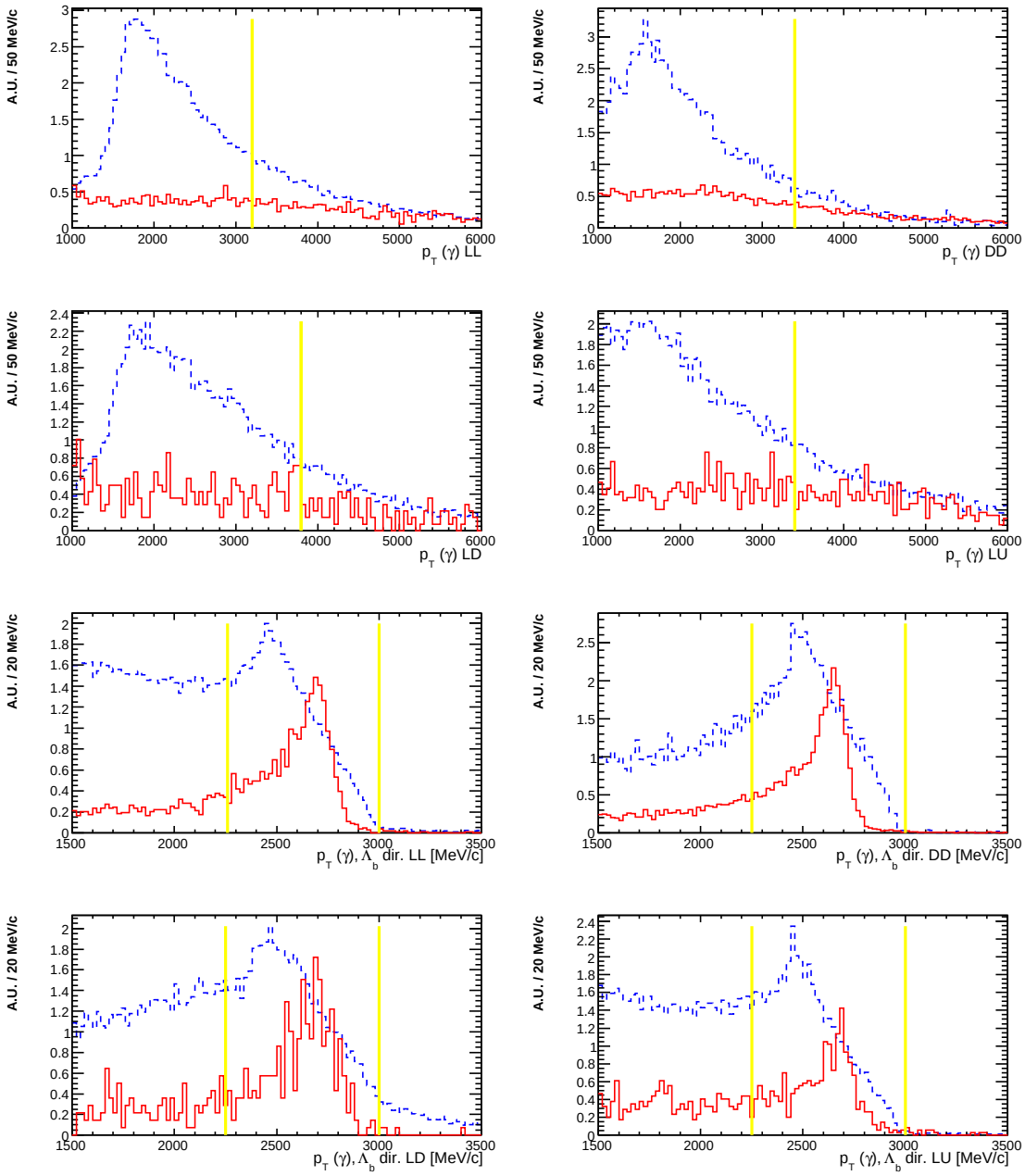



Figure 6.16: *Transverse momentum (four top plots) and transverse momentum with respect to the reconstructed $\Lambda_b$ flight direction (four bottom plots) for photon candidates in $\Lambda_b \to \Lambda(1115)\gamma$ decays. The red solid histogram corresponds to signal events where all reconstructed tracks have been associated to the true signal particles, while the blue dashed histogram to events from the $b\bar{b}$ inclusive sample. The vertical yellow lines represent the cut values.*

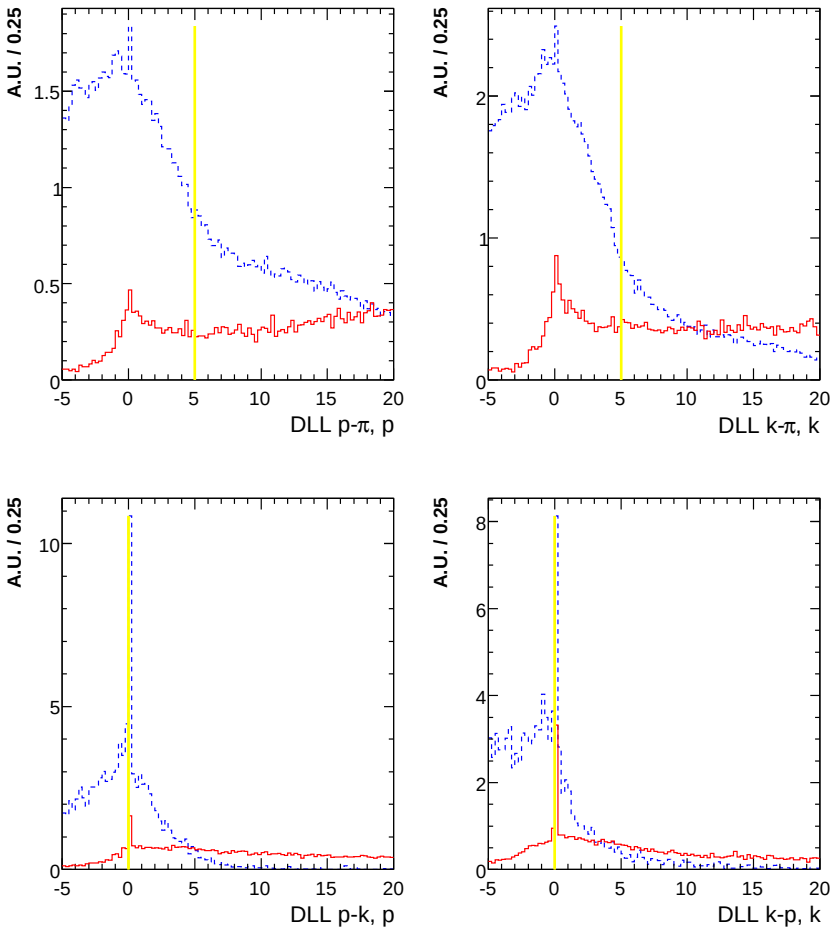



Figure 6.17: *Difference in log-likelihood probability (DLL) between various particle hypothesis for proton (left) and kaon (right) candidates in* $\Lambda_b \to \Lambda(1670)\gamma$ *decays. The red solid histogram contains signal events where the charged particle has been correctly identified, whereas the blue dashed histogram corresponds to events where the charged particle has been misidentified, in the* $b\bar{b}$ *inclusive sample (top), and in signal events (bottom). The vertical yellow lines represent the cut values.*

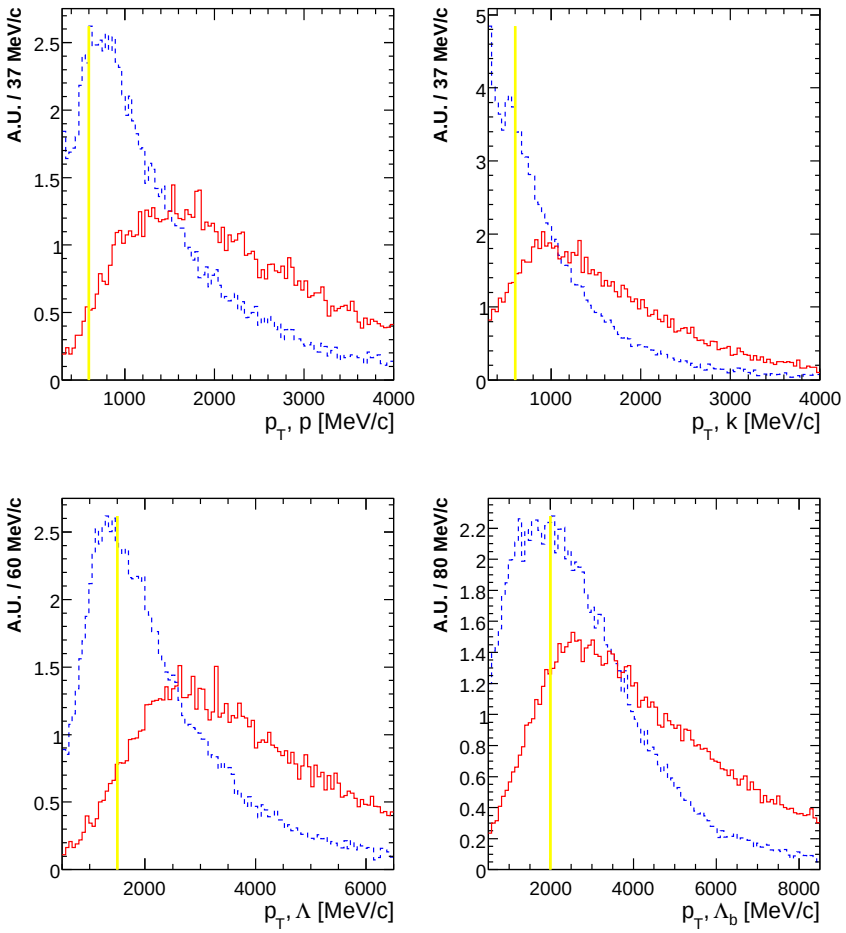



Figure 6.18: *Transverse momentum distribution for reconstructed proton, kaon, $\Lambda$ and $\Lambda_b$ candidates in $\Lambda_b \to \Lambda(1670)\gamma$ decays. The red solid histogram corresponds to signal events where all reconstructed tracks have been associated to the true signal particles, while the blue dashed histogram to events from the $b\bar{b}$ inclusive sample. The vertical yellow lines represent the cut values.*

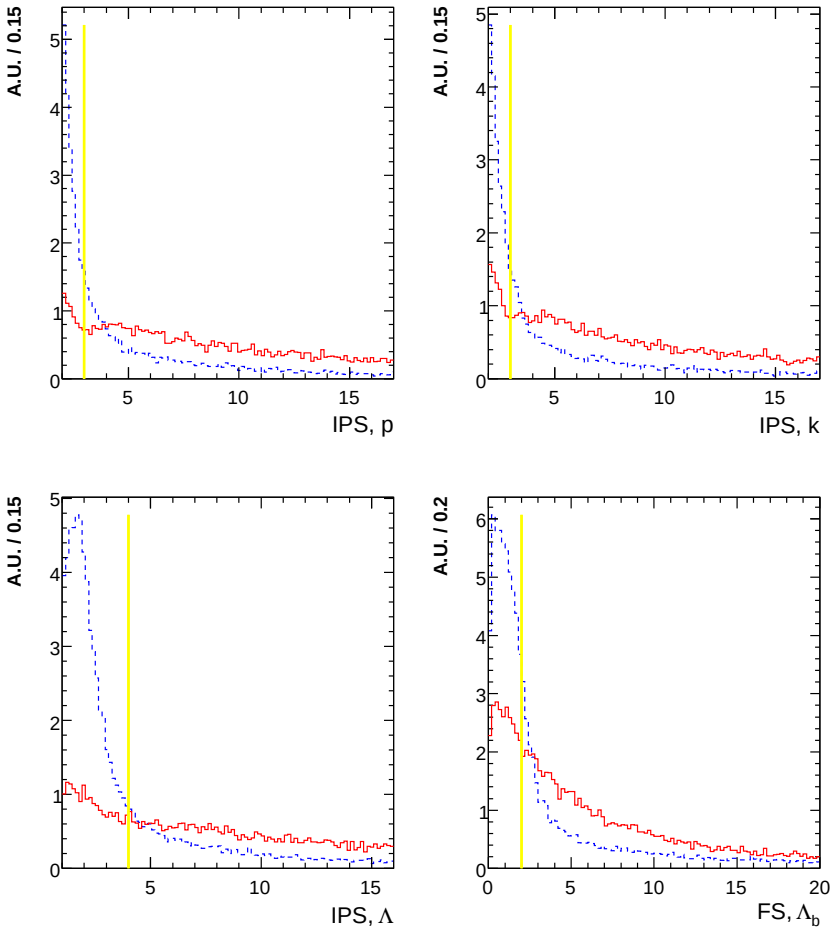



Figure 6.19: *Impact parameter significance (IPS) and flight distance significance (FS) distribution for reconstructed proton, kaon, $\Lambda$ and $\Lambda_b$ candidates in $\Lambda_b \to \Lambda(1670)\gamma$ decays. The red solid histogram corresponds to signal events where all reconstructed tracks have been associated to the true signal particles, while the blue dashed histogram to events from the $b\bar{b}$ inclusive sample. The vertical yellow lines represent the cut values.*

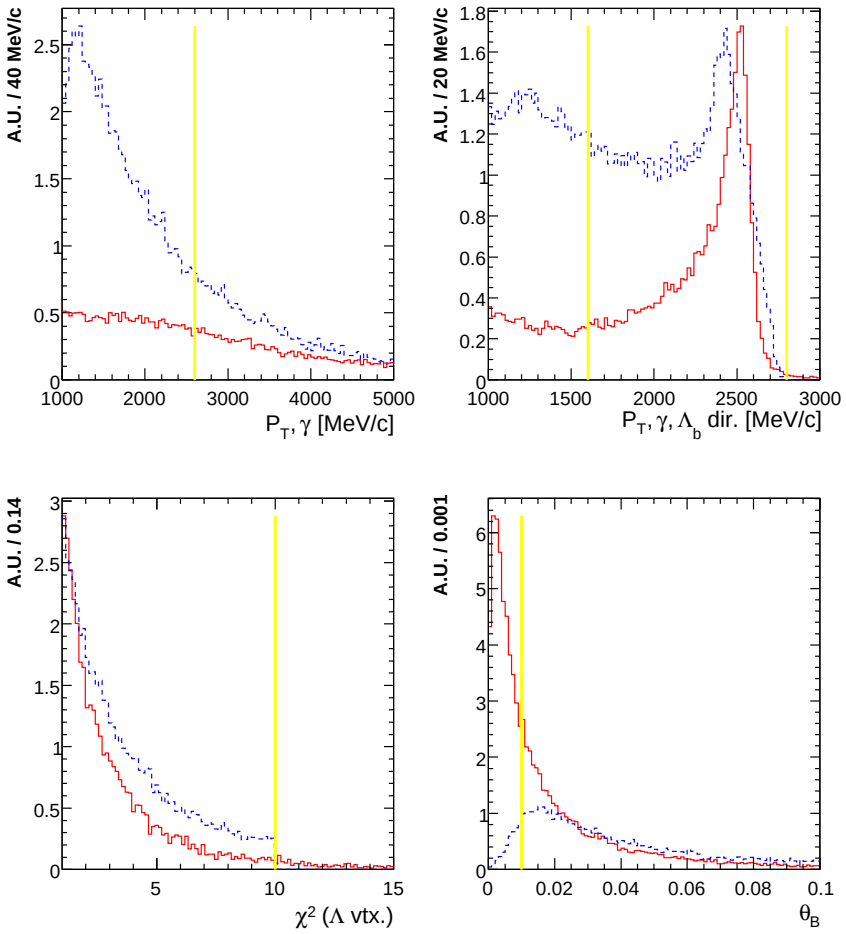



Figure 6.20: *Transverse momentum and transverse momentum with respect to the reconstructed $\Lambda_b$ flight direction for photon candidates in $\Lambda_b \rightarrow \Lambda(1670)\gamma$ decays (top plots). Distribution of $\Lambda$ vertex $\chi^2$ and the angle $\theta_b$ between the reconstructed $\Lambda_b$ momentum and flight direction (bottom plots). The red solid histogram corresponds to signal events where all reconstructed tracks have been associated to the true signal particles, while the blue dashed histogram to events from the $b\bar{b}$ inclusive sample. The vertical yellow lines represent the cut values.*

Chapter 7

# Sensitivity to the photon polarization measurement in $\Lambda_b \to \Lambda(X)\gamma$ decays at LHCb

*This chapter concludes our study of radiative decays of $\Lambda_b$ hadrons. Using the results of the previous chapters, we assess LHCb sensitivity to the measurement of the photon polarization in this type of decays.*

## 7.1 Introduction

In chapter 5 we studied polarized $\Lambda_b \to \Lambda(X)\gamma$ decays with the intent of measuring the polarization of the photon emitted in $b \to s$ transitions. We remind here that the photon polarization $\alpha_\gamma$ is defined as (cf. eq. 5.11):

$$\alpha_\gamma = \frac{1-|r|^2}{1+|r|^2} \tag{7.1}$$

The ratio $r$ is defined as the ratio of the Wilson coefficients $C_7'/C_7$, and therefore it takes into account the relative strength of the opposite chirality dipole operators which enter the effective $b \to s\gamma$ Hamiltonian.

The photon polarization can be extracted by the measurement of the angular distributions of the final states from polarized radiative $\Lambda_b$ decays. Such distributions depend on the spin of the intermediate $\Lambda(X)$ baryon.

For baryons of spin 1/2, the angular distributions of the photon and the proton take the form (see chapter 5):

$$\frac{d\Gamma}{d\cos\theta_\gamma} \propto 1 - \alpha_\gamma P_{\Lambda_b} \cos\theta_\gamma \tag{7.2}$$

$$\frac{d\Gamma}{d\cos\theta_p} \propto 1 - \alpha_\gamma \alpha_{p,1/2} \cos\theta_p \tag{7.3}$$

where $P_{\Lambda_b}$ is the $\Lambda_b$ polarization and $\alpha_{p,1/2}$ is the polarization parameter describing the $\Lambda(X)$ decay. An independent measurement of the $\Lambda_b$ polarization is therefore needed

to extract the value of $\alpha_\gamma$ from the photon angular distributions. In section 7.2 we will describe the $\Lambda_b$ production at the LHC, and give the expectations for $P_{\Lambda_b}$.

For $\Lambda(X)$ baryons of spin 3/2, the above angular distributions can be written as:

$$\frac{d\Gamma}{d\cos\theta_\gamma} \propto 1 - \alpha_{\gamma,3/2} P_{\Lambda_b} \cos\theta_\gamma \tag{7.4}$$

$$\frac{d\Gamma}{d\cos\theta_p} \propto 1 - \alpha_{p,3/2} \cos^2\theta_p \tag{7.5}$$

where $\alpha_{\gamma,3/2}$ is the $\Lambda_b$ asymmetry parameter defined in section 5.4.3. We have shown that the photon polarization can be probed in spin-3/2 baryon decays combining the measurements of $\alpha_{\gamma,3/2}$ and $\alpha_{p,3/2}$:

$$\alpha_\gamma = \frac{1}{2}\,\alpha_{\gamma,3/2}\left(1 - \frac{3}{\alpha_{p,3/2}}\right) \tag{7.6}$$

We finally identified as most promising the decays involving a $\Lambda(1115)$, $\Lambda(1520)$, $\Lambda(1670)$ or $\Lambda(1690)$ baryon. In chapter 6 we studied these decays in the LHCb environment, and, as a result of a full Monte Carlo simulation, we found the following annual event yields:

$$S_{\text{year}}(\Lambda_b \to (\Lambda(1115) \to p\pi)\gamma) \sim 675$$
$$S_{\text{year}}(\Lambda_b \to (\Lambda(1520) \to pK)\gamma) \sim 4270$$
$$S_{\text{year}}(\Lambda_b \to (\Lambda(1670) \to pK)\gamma) \sim 2250$$
$$S_{\text{year}}(\Lambda_b \to (\Lambda(1690) \to pK)\gamma) \sim 2250$$

In this chapter we study the possible sources of errors in the measurement of the photon polarization (see section 7.3), and finally use the previous results to estimate the LHCb sensitivity to such a measurement (in section 7.4).

## 7.2 $\Lambda_b$ production at the LHC

At the LHC, $\Lambda_b$ baryons will be produced in proton-proton collisions at a center-of-mass energy of $\sqrt{s} = 14$ TeV. The $\Lambda_b$ production rate is expected to be 5 times lower than the $B^0$ mesons production rate ($8\%$ vs. almost $40\%$), and is therefore comparable to the $B_s^0$ production rate ($10.5\%$) [101]. At LHCb we expect to have $10^{12}$ $b$-$\bar{b}$ pairs per year [46], which gives an annual yield of $1.6 \cdot 10^{11}$ $\Lambda_b$ (or $\overline{\Lambda}_b$) baryons.

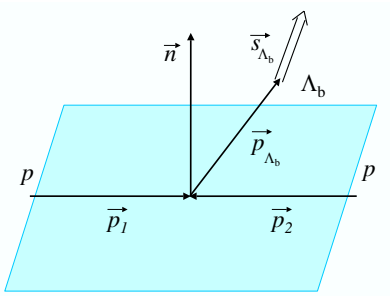



Figure 7.1: *The $\Lambda_b$ polarization in $pp$ collisions.*

The $\Lambda_b$ produced in the reaction $pp \to \Lambda_b X$ is expected to be polarized in a similar way to that of ordinary hyperons (the quark composition is the same if one replaces $b \to s$) [112]. If parity is conserved in strong interactions, the longitudinal polarization is indeed suppressed and the $\Lambda_b$ are transversally polarized with respect to their production plane because of a QCD mechanism at the parton level.

Let $\vec{n}$ be the vector normal to the production plane of the $\Lambda_b$ in its rest frame:

$$\vec{n} = \frac{\vec{p_1} \times \vec{p}_{\Lambda_b}}{|\vec{p_1} \times \vec{p}_{\Lambda_b}|}$$

where $\vec{p}_1$ and $\vec{p}_{\Lambda_b}$ are the vector-momenta of one incident proton beam and the $\Lambda_b$, respectively (see fig. 7.1). Then, the initial $\Lambda_b$ polarization is given by:

$$P_{\Lambda_b} =< \vec{s}_{\Lambda_b} \cdot \vec{n} >$$

where $s_{\Lambda_b}$ is the spin of the $\Lambda_b$.

The $\Lambda_b$ polarization is expected to be greater than 20% at the LHC [113]. The ATLAS experiment plans to measure it with a statistical precision of 1% [114] in the decay $\Lambda_b \rightarrow \Lambda(1115)J/\Psi$. This decay is also under study at LHCb [115].

In the following, we fix the polarization of the $\Lambda_b$ to a conservative estimation, $P_{\Lambda_b} = 0.20 \pm 0.01$, unless stated otherwise.

## 7.3 Error sources in the photon polarization measurement

To estimate the LHCb statistical sensitivity to the ratio $|r|$ we need to consider the various contributions to its measurement. In section 7.3.1 we describe the procedure applied to estimate the statistical errors. Detector resolution effects are dealt with in section 7.3.2, and found to be negligible.

### 7.3.1 Statistical errors

The ratio $|r|$ depends on the photon polarization $\alpha_\gamma$:

$$|r| = \sqrt{\frac{1-\alpha_\gamma}{1+\alpha_\gamma}}$$

and its relative statistical error is given by:

$$\frac{\sigma_{|r|}}{|r|} = \frac{1}{|r|^2}\frac{\sigma_{\alpha_\gamma}}{(1+\alpha_\gamma)^2}$$

The photon helicity parameter $\alpha_\gamma$ can be extracted from a linear fit of the measured angular distributions (7.2), (7.3) and (7.4). To estimate the statistical error on the measurement of the slope we use a fast toy Monte Carlo (RooFit [116]). We generate 1000 experiments of 1000 events each using as p.d.f. a linear distribution of the type $1 - s_\gamma \cos\theta$ for various values of the slope $s_\gamma$ in the interval [0,1]. The results are shown in fig. 7.2 (left plot), where the error on the slope is shown as a function of $s_\gamma$. We can therefore parameterize the error on the measurement of $s_\gamma$ from a linear fit (for $N$ events)as:

$$\sigma_{s_\gamma} = 0.0554 \cdot \sqrt{1 - 0.71 \cdot s_\gamma^2}\sqrt{1000/N} \tag{7.7}$$

For $\Lambda(X)$ baryons of spin 1/2, the photon polarization is then given by:

$$\alpha_\gamma = \frac{s_\gamma}{a}$$

where $a$ is either the $\Lambda_b$ polarization $P_{\Lambda_b}$ or the weak decay parameter $\alpha_{p,1/2}$. The (absolute) statistical error on the photon polarization is therefore:

$$\sigma_{\alpha_\gamma} = \frac{1}{a}\sqrt{\alpha_\gamma^2\sigma_a^2 + \sigma_{s_\gamma}^2}$$

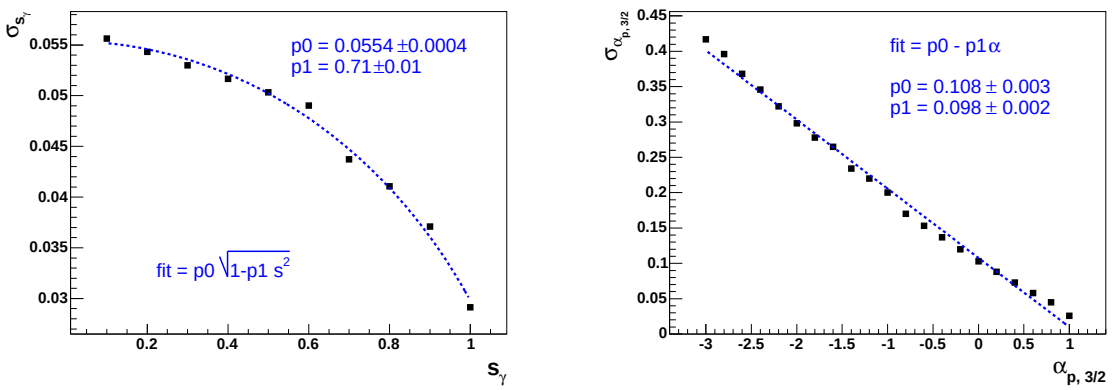



Figure 7.2: *Fast toy MC studies: statistical error in the measurement of the slope $s_\gamma$ (left) and the proton parameter $\alpha_p$ from decays involving a spin-3/2 $\Lambda$ resonance (right). The dashed lines represent a fit of the statistical error distributions.*

For $\Lambda(X)$ baryons of spin 3/2, the photon polarization is extracted from the measurement of the slope $s_\gamma$ and the proton parameter $\alpha_{p,3/2}$:

$$\alpha_\gamma = \frac{s_\gamma}{2P_{\Lambda_b}}\left(1 - \frac{3}{\alpha_{p,3/2}}\right)$$

and its statistical error:

$$\sigma_{\alpha_\gamma} = \sqrt{\alpha_\gamma^2\left(\frac{\sigma_{s_\gamma}^2}{s_\gamma^2} + \frac{\sigma_{P_{\Lambda_b}}^2}{P_{\Lambda_b}^2}\right) + \frac{9}{4}\frac{s_\gamma^2}{P_{\Lambda_b}^2}\frac{\sigma_{\alpha_{p,3/2}}^2}{\alpha_{p,3/2}^4}}$$

The proton asymmetry parameter $\alpha_{p,3/2}$ can be extracted from a fit of the angular distribution (7.5). To estimate its statistical error we generate with a fast toy Monte Carlo 1000 experiments of 1000 events each (using as p.d.f. the distribution (7.5)). The results are shown in fig. 7.2 (right plot), where $\sigma_{\alpha_{p,3/2}}$ is shown for the range of $\alpha_{p,3/2}$ of interest. We assume a linear dependance of the type (for $N$ events):

$$\sigma_{\alpha_{p,3/2}} = (0.11 - 0.10 \cdot \alpha_{p,3/2})\sqrt{1000/N} \tag{7.8}$$

We therefore have all ingredients to estimate the statistical error contribution to the measurement of the photon polarization. The above formulas will be used in assessing the LHCb sensitivity to the measurement of $r$ (see section 7.4).

### 7.3.2 Detector resolution

To study the effect of detector resolution on the measurement of the photon polarization, we consider the photon angular distribution from events generated and reconstructed in the LHCb environment. In fig. 7.3 one can find such a distribution from $\Lambda_b \to \Lambda(1670)\gamma$ events which pass all selection criteria defined in section 6.5.

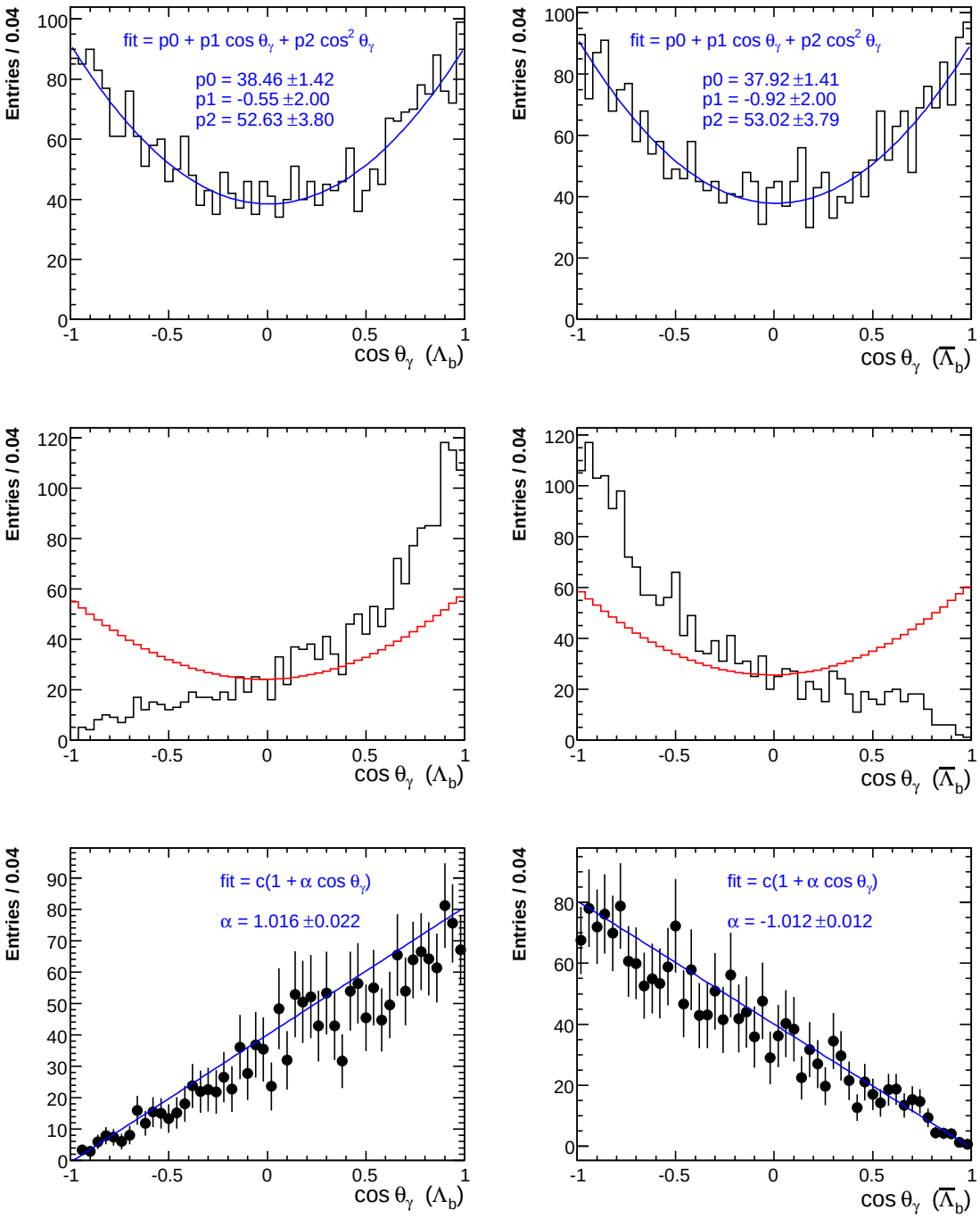



Figure 7.3: *Top: photon angular distribution of selected* $\Lambda_b \to \Lambda(1670)\gamma$ *events from the unpolarized sample. The blue curve is the fit to a parabolic distribution. Middle: photon angular distribution from the transversally polarized event sample. In red the efficiency curve is shown. Bottom: photon angular distribution from the transversally polarized sample, after the efficiency correction. In blue, the linear fit is shown. The left plots contain* $\Lambda_b$ *events, whereas the right ones contain* $\overline{\Lambda}_b$ *events.*

If the selection efficiency is constant in $\theta_\gamma$, events from the unpolarized sample[1] are expected to have a flat distribution. However we find that a parabolic fit is in good agreement with the measured angular distribution (top plots). The effect is due to the selection criteria, in particular the requirement on the photon transverse momentum in the $\Lambda_b$ direction.

We can use the fitted angular distribution from unpolarized decays to correct the angular distribution of selected events from the transversally polarized event sample for the non-uniform selection efficiency (middle plots). The result is shown in fig. 7.3 (bottom plots). From real data, the efficiency dependence in $\theta_\gamma$ can be extracted from reconstructed $B_d \to K^*\gamma$ decays, which have a very similar topology but no intrinsic photon asymmetry.

Finally, we fit the efficiency corrected photon angular distribution with eq. (7.2).

The fit gives the following results for the photon polarization:

- $\alpha_\gamma$ = 1.02 $\pm$ 0.02 (1755 reconstructed $\Lambda_b$ decays);
- $\alpha_\gamma$ = 1.01 $\pm$ 0.01 (1863 reconstructed $\overline{\Lambda}_b$ decays).

We remind here that all events have been generated with full $\Lambda_b$ ($P_{\Lambda_b} = 1$) and photon ($\alpha_\gamma = 1$) polarization.

The statistical error on the measurement of the slope from a linear fit can be estimated using eq. (7.7). For 1755 events, and a measured $\alpha_\gamma$ = 1.02 we expect $\sigma_{\alpha_\gamma}$ = 0.02, which indeed is compatible with the error on $\alpha_\gamma$ given by the linear fit. The detector resolution contribution to the measurement of $\alpha_\gamma$ can therefore be neglected.

Since probing the photon polarization can be seen as a forward-backward asymmetry measurement[2], systematic errors are expected to be small relative to statistical ones, and therefore will be neglected in the following. A quantitative study of systematic errors will be performed as soon as LHCb starts taking data.

## 7.4 LHCb sensitivity to the measurement of $|r|$

We can now study the experimental prospects for a measurement of the photon polarization in $\Lambda_b \to \Lambda(X)\gamma$ decays at LHCb. We have seen that the photon is predicted to be mainly left-handed in the Standard Model. Right-handed components are given by the ratio $|r|$.

In fig. 7.4 we show the expected experimental reach for $|r|$ from single (left plots) and combined (right) measurements after 1 (top) and 5 (middle and bottom) years of running at LHCb. The $\Lambda_b$ polarization has been fixed to a conservative value of (20 $\pm$ 1)% for the top and middle plots, and to the best-case[3] value of (100 $\pm$ 5)% in the bottom plots. We have used the event yields given above, and furthermore assumed no CP violation, therefore the same amount of $\Lambda_b$ and $\overline{\Lambda}_b$ decays.

The significance on the measurement of $|r|$ can be defined as $|r|/\sigma_{|r|}$, where $\sigma_{|r|}$ is the statistical error calculated using the procedure described in section 7.3.1. The various curves show the range of $|r|$ that can be probed at 3 sigma significance. This range is given as a function of the proton parameter parameter $\alpha_{p,3/2}$ for spin-3/2 $\Lambda(X)$ decays.

[1] We remind that several samples of $\Lambda_b \to \Lambda(1670)\gamma$ events have been generated for angular asymmetries studies. In particular we generated events with: unpolarized (phase space), full longitudinally and full transversally polarized $\Lambda_b$. See section 6.4.1.

[2] In a simplified view, it is essentially a counting experiment, where one measures the difference of the numbers of photons produced in two opposite direction (parallel or antiparallel to the $\Lambda_b$ polarization vector).

[3] Fully polarized $\Lambda_b$ decays result in the largest asymmetries. See eq. (7.2).

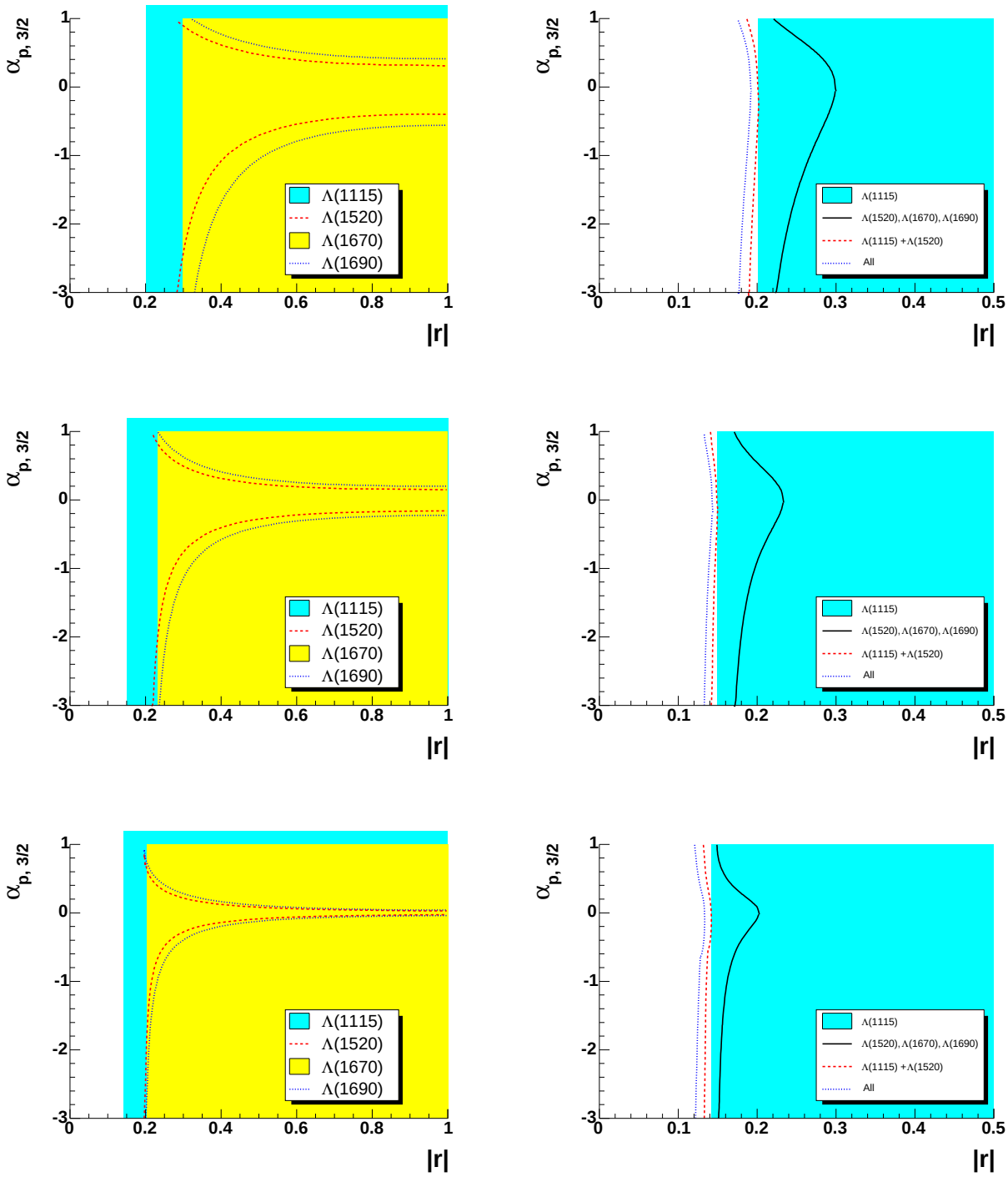



Figure 7.4: *Experimental reach for $|r|$ (as a function of $\alpha_{p,3/2}$ for decays involving a 3/2 spin $\Lambda(X)$), obtained by averaging $|r|$ over CP conjugate decays in the limit of no CP violation. The plots show the values of $|r|$ that can be probed at 3 sigma significance (ranges are to be read starting from the curves and ending at 1) in single (left) and combined (right) measurements of several decay modes. The sensitivities are calculated for 1 (top) and 5 (middle and bottom) years of data taking at LHCb. The $\Lambda_b$ polarization has been fixed to (20 $\pm$ 1)% for the top and middle plots, and to (100 $\pm$ 5)% in the bottom plots.*

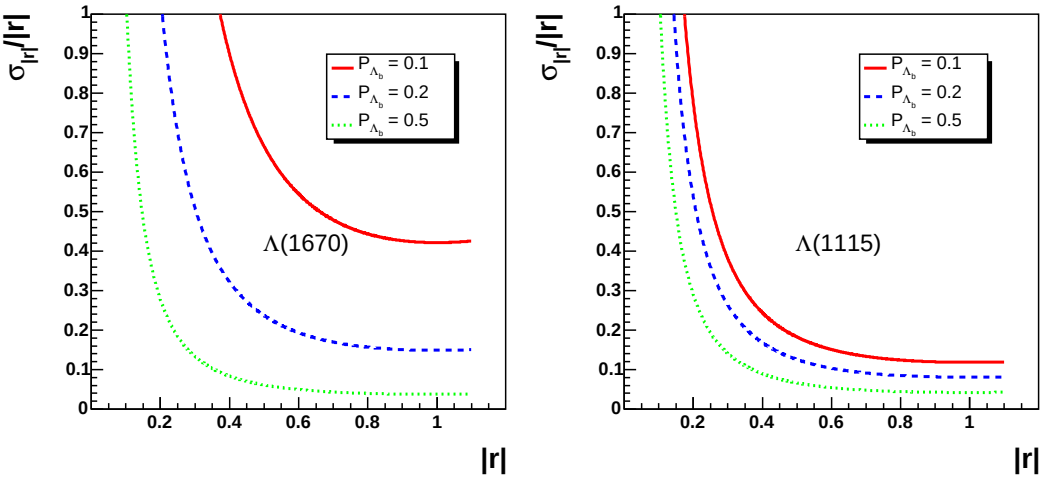



Figure 7.5: *Relative statistical error in $|r|$ as a function of $|r|$ obtained by averaging over CP conjugate decays in the limit of no CP violation, for different values of the $\Lambda_b$ polarization $P_{\Lambda_b}$: 0.1 (solid), 0.2 (dashed), 0.5 (dotted) for 1 year of data taking at LHCb for the decays $\Lambda_b \to \Lambda(1115)\gamma$ (right) and $\Lambda_b \to \Lambda(1670)\gamma$ (left).*

In $\Lambda_b \to \Lambda(1115)\gamma$ decays, $|r|$ can be measured independently from both the photon and the proton angular distribution. The values of $P_{\Lambda_b}$ and $\alpha_p$ and their errors being of the same order of magnitude, one can therefore largely compensate the lower annual yield combining the two measurements. As a result, this decay gives the best sensitivity for the $|r|$ measurement. The right-handed component of the photon polarization can be probed down to 20% at 3 sigma significance after 1 year of running. Increasing the statistics by a factor 5 gives an additional 5% improvement.

Decays involving the $\Lambda(X)$ resonances can become competitive if the proton asymmetry $\alpha_{p,3/2}$ is large enough to allow a clean measurement of the angular distribution of interest. Also increasing the statistics helps to sharpen the significance curves, as can be seen by comparing the two curves after 1 and 5 years of running. In this case the sensitivity to the $|r|$ measurement improves by 5–10 % (according to the resonance) after 5 years.

The possible scenarios obtained by combining[4] the various measurements are (see right plots in fig. 7.4):

- Only the decay $\Lambda_b \to \Lambda(1115)\gamma$ is measured. The range of $|r|$ that can be probed is given as a reference.
- Only decays involving a strong $\Lambda(X)$ resonances are measured. This is the worst case. With respect to the measurement of the $\Lambda(1115)$ alone, the range of $|r|$ that can be probed is worse by a few percent, depending on the value of $\alpha_{p,3/2}$.
- Decays involving the $\Lambda(1115)$ and $\Lambda(1520)$ are measured (disentangling the $\Lambda(1670)$

[4]We assume here that $\alpha_{p,3/2}$ has the same value for the $\Lambda(1520)$ and the $\Lambda(1690)$ resonances.

and $\Lambda(1690)$ not possible). The sensitivity on the $|r|$ measurement can be improved by 1% at the most.

- All decays are measured and disentangled. The improvement on the $|r|$ sensitivity is of the order of 2% at most.

### 7.4.1 Dependence on the $\Lambda_b$ polarization

As the amount of polarization of the $\Lambda_b$ at the LHC is not known with a fair degree of certainty, we study the dependence of the photon polarization measurement on $P_{\Lambda_b}$

The sensitivity of the measurement of $|r|$ to the value of the $\Lambda_b$ polarization is shown in fig. 7.5 for $\Lambda_b \to \Lambda(1115)\gamma$ and $\Lambda_b \to \Lambda(1670)\gamma$ decays. Combining the measurement of both the photon and the proton angular distributions, as in $\Lambda(1115)$ decays, one can reduce quite well the dependence on $P_{\Lambda_b}$, whereas if $\alpha_\gamma$ can only be extracted from the photon angular distribution, as in $\Lambda$ resonances decays, a polarization of at least 20% is needed to have a good sensitivity already after 1 year of data taking.

On the other hand a large value of the $\Lambda_b$ polarization (see bottom plots in fig. 7.4 where $P_{\Lambda_b} = 1.00 \pm 0.05$) can improve the range of $|r|$ which can be probed by at most a few percent, but reduces the dependence on $\alpha_{p,3/2}$.

## 7.5 Conclusions

The sensitivity of LHCb to the measurement of the photon polarization in decays of the type $\Lambda_b \to \Lambda(X)\gamma$ has been studied. The main conclusion is that, assuming a $\Lambda_b$ polarization of at least 20%, LHCb can measure the right-handed component of the photon polarization down to 15% at $3\sigma$ significance after 5 years of running from $\Lambda_b \to \Lambda(1115)\gamma$ decays. The additional contribution from the $\Lambda(X)$ resonances to the measurable range has been estimated to be 2% at most.

However if the decay involving the $\Lambda(1115)$ is not experimentally accessible (due for instance to failures of the tracking system or to trigger inefficiencies), the right-handed component of the photon polarization can still be measured from the decays involving the $\Lambda(1520)$, $\Lambda(1670)$, $\Lambda(1690)$ (assuming that the last two can actually be disentangled). In this case, the sensitivity is worse by 5% with respect to the measurement of the $\Lambda(1115)$ alone.

The dependence of the photon polarization sensitivity on the initial $\Lambda_b$ polarization (in the range $P_{\Lambda_b}$ = 20–100%) has been found to be of the order of a few percent.

Right-handed components up to 10–15% are predicted by the Standard Model (SM) for decays of the type $B \to X_s\gamma$. However explicit calculations for many exclusive channels (among those, $\Lambda_b$ radiative decays) do not exist at the moment. If a value of $|r|$ around 10–15% is measured, additional theoretical efforts will be required to understand whether this can still be accommodated in the SM. However if a larger value of $|r|$ is measured, it clearly would be a hint of new physics beyond the SM. At LHCb one can therefore expect to make a first measurement of the photon polarization, if $|r|$ is large enough, or set an interesting limit in case $|r|$ does not deviate from the SM expected value.

# Conclusion

The work presented in this thesis can be divided in two parts: the R&D for the development of a common "off detector" readout board (TELL1) for LHCb, and the study of polarized radiative $\Lambda_b$ decays. We summarize here the main results obtained with this thesis work.

As the LHCb detector was being designed, the requirements for the readout electronics were continuously adapted to better match the needs of the physics program. As a result, the TELL1 board prototypes evolved in time, following both the technology developments and the system design requirements. In this thesis we report on part of this exciting process for the period that covers the years 2001-2003. In particular we have presented a mixed DSP-FPGA architecture which employs SRAM memories for data buffering during the trigger latency. Despite the fact that this architecture satisfies the LHCb readout electronics requirements at the time of its design, we find that developing and supporting both the DSP and the FPGA technologies is too demanding for a project that aims at a final production of about 300 readout boards. As a result of the DSP-FPGA tests, an FPGA only approach was chosen for the final design, since they proved more versatile and flexible. This led to a higher system integration in the final TELL1 board, and made possible a painless migration from the three-level trigger to the 1 MHz readout scheme.

Polarized radiative $\Lambda_b$ decays represent an important sector to search for physics beyond the Standard Model. The LHC will present a fine opportunity for such a study, due to the large number of $b$ hadrons that will be produced in $pp$ collisions.

A phenomenological study of decays of the type $\Lambda_b \to \Lambda(X)\gamma$, where $\Lambda(X)$ is a $\Lambda$ baryon of mass $X$ and spin 1/2 or 3/2, has been presented. In particular we exploit the initial polarization of the $\Lambda_b$ baryon to probe the polarization of the photon emitted in $b \to s$ transitions. The final states angular distributions have been calculated taking advantage of the helicity formalism. We identify as most promising $\Lambda_b$ decays containing a $\Lambda(1115)$, $\Lambda(1520)$, $\Lambda(1670)$, or $\Lambda(1690)$ baryon.

The reconstruction of the decays $\Lambda_b \to \Lambda(1115)\gamma$ and $\Lambda_b \to \Lambda(1670)\gamma$ (as a representative of the various $\Lambda(X)$ resonances) has been studied in the LHCb environment. We find annual signal yields of about 750 events for the first and 2500 for the second channel. Assuming that the dominant background comes from $b\bar{b}$ events, we estimate the background to signal ratio $B/S$ to be respectively less than 42 and 18 at 90% confidence level. The observation of these decays and the measurement of the branching ratios are expected to be feasible already after 1 year of data taking. We also find that the detector resolution effects can be neglected in the measurement of the emitted photon polarization.

Finally the previously obtained results are gathered to assess the LHCb sensitivity to the photon polarization. Assuming a conservative estimate of the initial $\Lambda_b$ polarization

(20%), we find that values of $|r| \gtrsim 15\%$ can be probed at $3\sigma$ significance from $\Lambda_b \to \Lambda(1115)\gamma$ decays after 5 years of running at LHCb. The sensitivity improvement due to the measurement of the photon polarization from decays involving the $\Lambda$ resonances of interest has been estimated to be a few percent at most. However these decays can be competitive (total sensitivity worse by only 5%) if the decay involving the $\Lambda(1115)$ is not experimentally accessible (due for instance to failures of the tracking system or to trigger inefficiencies).

As current prospects of measuring the polarization of the photon emitted in $b \to s$ transitions at the $B$ factories are not very appealing due to the limited statistics, we can conclude that the LHCb experiment has good chances of probing the $\gamma$ polarization for the first time, or at least set a very interesting limit.

# Bibliography


[1] The Particle Data Group of Lawrence Berkeley National Laboratory, *The Particle Adventure*, http://particleadventure.org/.

[2] P. Koppenburg, *Contribution to the development of the LHCb Vertex Locator and study of rare semileptonic decays*, Ph.D. thesis, Université de Lausanne (2002).

[3] A. D. Sakharov, *Violation of CP invariance, C asymmetry, and baryon asymmetry of the universe*, JETP Lett. 5 (1967) 24–27.

[4] *CERN document server*, `http://weblib.cern.ch`.

[5] E. Leader, E. Predazzi, *An introduction to gauge theories and modern particle physics*, Vol. 3 and 4 of *Monographs on Particle Physics, Nuclear Physics and Cosmology*, Cambridge University Press, Cambridge, UK, 1996, ISBN 0 521 46840 X a,d ISBN 0 521 49951 8.

[6] A. Salam, R. Delbourgo, J. Strathdee, *Weak and Electromagnetic Interactions*, in: N. Svartholm (Ed.), Elementary Particle Theory, Proceedings Of The Nobel Symposium Held 1968 at Lerum, Sweden, Stockholm 1968, Almquist and Wiksells, Stockholm, 1968, pp. 367–377.

[7] S. Glashow, *Partial Symmetries of Weak Interactions*, Nucl. Phys. 22 (1961) 579–588.

[8] S. Weinberg, T. Lee, B. Zumino, *Algebra of Fields*, Phys. Lett. 18 (1967) 1029–1032.

[9] M. Peskin, *An introduction to Quantum Field Theory*, Harper-Collins Publishers, 1995, ISBN 0 201 50397 2.

[10] P. Higgs, *Broken symmetries and the masses of gauge bosons*, Phys. Rev. Lett. 13 (1964) 508.

[11] Y. Nir, *Flavor physics and CP violation*, hep-ph/9810520 (1998).

[12] N. Cabibbo, *Unitary Symmetry and Leptonic Decays*, Phys. Rev. Lett. 10 (1963) 531–532.

[13] M. Kobayashi, T. Maskawa, *CP violation in the renormalizable theory of weak interaction*, Prog. Theor. Phys. 49 (1973) 652.

[14] C. Jarlskog, *CP violation*, Vol. 3 of *Advanced series on Directions in High Energy Physics*, World Scientific Publishing, Teaneck, USA, 1989, ISBN 9971 50 561 4.

[15] S. Glashow, J. Iliopoulos, L. Maiani, *Weak Interactions with Lepton–Hadron Symmetry*, Phys. Rev. D 2 (1970) 1285–1292.

[16] G.L. Fogli et al., *Neutrino mass and mixing parameters: A short review*, hep-ph/0506307 (2005).

[17] A. Guglielmi, M. Mezzetto, P. Migliozzi, F. Terranova, *Measurement of three-family neutrino mixing and search for CP violation*, hep-ph/0508034 (2005).

[18] A. Buras, R. Fleischer, *Quark Mixing, CP Violation and Rare Decays After the Top Quark Discovery*, in: A. Buras, M. Lindner (Eds.), Heavy Flavours II, World Scientific, 1997.

[19] *PEP-II: Asymmetric B Factory*, http://www.slac.stanford.edu/grp/ad/ADPEPII/.

[20] *KEKB: An Asymmetric Electron-Positron Collider for $B$ Physics*, http://www-acc.kek.jp/KEKB/.

[21] E. Witten, *Short Distance Analysis of Weak Interactions*, Nucl. Phys. B 122 (1977) 109.

[22] K. Wilson, W. Zimmermann, *Operator Product Expansions and Composite Field Operators in the General Framework of Quantum Field Theory*, Comm. Math. Phys. 24 (1972) 87.

[23] A. Buras, *Flavour dynamics: CP violation and rare decays*, lecture given at the $38^{\rm th}$ Course of the Erice International School of Subnuclear Physics, Aug 27 – Sep 5 2000 (2001).

[24] H. Georgi, *An Effective Field Theory for Heavy Quarks at Low Energies*, Phys. Lett. B 240 (1990) 447–450.

[25] G. Buchalla, A. Buras, M. Lautenbacher, *Weak Decays Beyond Leading Logarithms*, Rev. Mod. Phys. 68 (1996) 1125–1144.

[26] F. Krüger, E. Lunghi, *Looking for novel CP violating effects in $B \to \ell^+\ell^- K^*$*, Phys. Rev. D 63 (2001) 014013.

[27] A. Ali, G. Hiller, *A theoretical reappraisal of branching ratios and CP asymmetries in the decays $B \to (X_{\bar{d}}, X_{\bar{s}})\ell^+\ell^-$ and determination of the CKM parameters*, Eur. Phys. J. C 8 (1999) 619–629.

[28] S. Chen et al. (CLEO collaboration), *Branching Fraction and Photon Energy Spectrum for $b \to s\gamma$*, Phys. Rev. Lett. 87 (2001) 251807.

[29] P. Koppenburg et al. (BELLE collaboration), *Inclusive measurement of the photon energy spectrum in $b \to s\gamma$ decays*, Phys. Rev. Lett. 93 (2004) 061803.

[30] T. Hurth, *Present status of inclusive rare $B$ decays*, Rev. Mod. Phys. 75 (2003) 1159.

[31] P. Gambino, M. Misiak, *Quark mass effects in $B \to X_s\gamma$*, Nucl. Phys. B 611 (2001) 338.

[32] *The Heavy Flavour Averaging Group web site*, `http://www.slac.stanford.edu/xorg/hfag/`.

[33] B. Grinstein, Y. Grossman, Z. Ligeti, D. Pirjol, *The photon polarization in $B \to X\gamma$ in the Standard Model*, Phys. Rev. D 71 (2005) 011504.

[34] D. Atwood, M. Gronau, A. Soni, *Mixing-induced CP asymmetries in radiative $B$ decays in and beyond the Standard Model*, Phys. Rev. Lett. 79 (1997) 185.

[35] Y. Grossman, D. Pirjol, *Extracting and using photon polarization information in radiative $B$ decays*, JHEP 06 (2000) 029.

[36] D. Melikhov, N. Nikitin, S. Simula, *New physics effects in $B \to K^{(*)}\nu\nu$ decays*, Phys. Lett. B 442 (1998) 381.

[37] M. Gronau, Y. Grossman, D. Pirjol, A. Ryd, *Measuring the photon polarization in $B \to K\pi\pi\gamma$*, Phys. Rev. Lett. 88 (2002) 051802.

[38] B. Aubert et al. (BABAR Collaboration), *Measurement of branching fractions and mass spectra of $B \to K\pi\pi\gamma$*, hep-ex/0507031 (2005).

[39] M. Knecht, T. Schietinger, *Probing photon helicity in radiative $B$ decays via charmonium resonance interference*, Phys. Lett. B 634 (2006) 403.

[40] *CERN public web pages*, `http://www.cern.ch`.

[41] *LHC machine public web pages*, `http://lhc-new.homepage.web.cern.ch/lhc-new-homepage/`.

[42] *Tevatron Luminosity web pages*, `http://www.fnal.gov/pub/now/tevlum.html`.

[43] *KEKB web pages*, `http://www-acc.kek.jp/kekb/`.

[44] T. Nakada, O. Schneider, *LHCb Trigger*, in: Proceedings of the 4th International Workshop on B physics and CP violation, February 19-23, 2001, Ise-Shima, Japan, IPHE, 2001.

[45] S. Amato et al. (LHCb collaboration), *LHCb Technical Proposal*, CERN, Genève, 1998, CERN-LHCC-98-4.

[46] R. Antunes Nobrega et al. (LHCb collaboration), *LHCb Reoptimized Detector (design and performance) Technical Design Report*, CERN, Genève, 2003, CERN/LHCC/2003-030.

[47] S. Amato et al. (LHCb collaboration), *LHCb RICH Technical Design Report*, CERN, Genève, 2000, CERN/LHCC/2000-0037.

[48] S. Amato et al. (LHCb collaboration), *LHCb Magnet Technical Design Report*, CERN, Genève, 1999, CERN/LHCC/2000-007.

[49] R. Antunes Nobrega et al. (LHCb collaboration), *LHCb Inner Tracker Technical Design Report*, CERN, Genève, 2002, CERN/LHCC/2002-029.

[50] S. Amato et al. (LHCb collaboration), *LHCb Calorimeters Technical Design Report*, CERN, Genève, 2000, CERN/LHCC/2000-0036.

[51] P.R. Barbosa Marinho et al. (LHCb collaboration), *LHCb Muon System Technical Design Report*, CERN, Genève, 2001, CERN/LHCC/2001-010.

[52] *CMS challenges*, http://cmsinfo.cern.ch/Welcome.html/CMSdocuments/CMSchallenges.

[53] *Timing, Trigger and Control web pages*, http://ttc.web.cern.ch/TTC/intro.html.

[54] *LHCb Experiment Control System web pages*, http://lhcb-comp.web.cern.ch/lhcb-comp/ECS/default.html.

[55] R. Antunes Nobrega et al. (LHCb collaboration), *LHCb Trigger System Technical Design Report*, CERN, Genève, 2003, CERN/LHCC/2003-031.

[56] L. Camilleri et al., *Review of the 1 MHz readout proposal*, LHCb 2005-063 (2005).

[57] F. Legger, T. Schietinger, *The LHCb trigger and readout*, LHCb TRIG 2005-070 (2005).

[58] R. Antunes Nobrega et al. (LHCb collaboration), *LHCb Computing System Technical Design Report*, CERN, Genève, 2005, CERN/LHCC/2005-019.

[59] R. Jacobsson, B. Jost, *Timing and Fast Control*, LHCb 2001-016 (2001).

[60] R. Jacobsson, *Requirements to the L0 Front End electronics*, LHCb ELEC 2001-014 (2001).

[61] R. Jacobsson, *Requirements to the L1 Front End electronics*, LHCb ELEC 2003-078 (2003).

[62] G. Haefeli, A. Bay, F. Legger, L. Locatelli, J. Christiansen, D. Wiedner, *TELL1 specification for a common readout board for LHCb*, LHCb ELEC 2003-007 (2003).

[63] Y. Ermoline, V. Lindenstruth, A. Walsch, *Vertex Detector Electronics - L1 Electronics Prototyping*, LHCb VELO 98-069 (2000).

[64] A. Bay et al., *Test on the L1-Electronics board prototype RB2*, LHCb VELO 2002-033 (2002).

[65] Y. Ermoline, *Vertex Detector Electronics — RB3 Specification*, LHCb VELO 2001-050 (2001).

[66] B. Jost et al., *The 1 MHz readout*, LHCb 2005-062 (2005).

[67] I. Belyaev, G. Corti, S. Easo, W. Pokorski, F. Rajnard, P. Robbe, *Gauss User Guide and Reference manual*, http://lhcb-comp.web.cern.ch/lhcb-comp/Simulation/Gauss.pdf.

[68] *EvtGen web site*, http://lhcb-comp.web.cern.ch/lhcb-comp/Simulation/evtgen.htm.

[69] *The Gaudi project*, http://proj-gaudi.web.cern.ch/proj-gaudi/.

[70] *Boole web site*, http://lhcb-comp.web.cern.ch/lhcb-comp/Digitization/.

[71] *Brunel web site*, http://lhcb-comp.web.cern.ch/lhcb-comp/Reconstruction/.

[72] *DaVinci web site*, http://lhcb-comp.web.cern.ch/lhcb-comp/Analysis/.

[73] F. Legger et al., *TELL1: a common readout board for LHCb*, in: Proceedings of the X Vienna Conference on Instrumentation (VCI), Elsevier, 2004.

[74] G. Haefeli, A. Bay, F. Legger, L. Locatelli, *A common data acquisition board for LHCb*, in: Proceedings of the 9th Workshop on Electronics for LHC experiments (LECC), 2003.

[75] N. van Bakel et al., *The Beetle Reference Manual*, Prentice Hall, 1993.

[76] G. Haefeli, *Contribution to the development of the acquisition electronics for the LHCb experiment*, Ph.D. thesis, Ecole polytechnique fédérale de Lausanne (2004).

[77] A. Bay, G. Haefeli, P. Koppenburg, *LHCb* VELO *Off Detector Electronics Preprocessor and Interface to the Level 1 Trigger*, LHCb VELO 2001-043, IPHE 2000-019 (2001).

[78] S. Saladino, *Study of Vertex silicon detector for LHC experiments*, Ph.D. thesis, Université de Lausanne (2002).

[79] Texas Instruments, *TI DSP web site*, `http://www.dspvillage.ti.com/`.

[80] Analog, *Analog DSP web site*, `http://www.analog.com/processors/`.

[81] Texas Instruments, *TMS320C6000 EMIF: Overview of Support of High Performance Memory Technology*, Application Report SPRA631.

[82] G. Haefeli, A. Gong, *LHCb VELO and ST clusterization on TELL1*, `http://edms.cern.ch/document/690585`.

[83] N. Tuning, *L1-type Clustering in the VELO on Test-beam data and simulation*, LHCb TRIG 2003-073 (2003).

[84] L. Locatelli, J. Borel, A. Bay, R. Frei, G. Haefeli, P. Jalocha, *Tests on the VELO analogue transmission line with the TELL1 prototype RB3*, LHCb 2004-086 (2004).

[85] DeVaSys, *The USB $I^2C$ IO*, `http://www.devasys.com/usbi2cio.htm`.

[86] R. Jacobsson, *How can I run my detector?*, LHCb 2001-140 (2001).

[87] O. Boyle, R. McLaren, E. der Bij, *S-Link interface Specification*, `http://www.cern.ch/HSI/s-link`.

[88] Texas Instruments, *TMS320 DSP/BIOS User Guide*, Reference Guide, SPRU423B.

[89] *DIM, a Distributed Information Management system*, `http://dim.web.cern.ch/dim/`.

[90] *PVSS introduction for Newcomers*, `http://lhcb-comp.web.cern.ch/lhcb-comp/ECS/PVSSIntro.htm`.

[91] Altera, *Techniques for implementing multipliers in Stratix, Stratix GX and Cyclone devices*, Application note AN306.

[92] Y. Ermoline, *Vertex Detector Electronics: Timing and Synchronization issues*, LHCb VELO 98-052 (1998).

[93] J. Christiansen, A. Marchioro, P. Moreira, A. Sancho, *Receiver Asic for Timing Trigger and Control Distribution in LHC Experiments*, IEEE Trans. Nucl. Sc. 43 (1996) 1773–1777.

[94] Philips Semiconductors, *The $I^2C$ bus specification*, `http://www.semiconductors.philips.com/acrobat/literature/9398/39340011.pdf`.

[95] G. Haefeli, *Various talks presented at LHCb weeks electronics meetings*, `http://agenda.cern.ch/`.

[96] Texas Instruments, *TMS320C6000 CPU and Instruction Set*, Reference Guide, SPRU189F.

[97] Texas Instruments, *TMS320C6000 Peripherals*, Reference Guide, SPRU190D.

[98] G. Hiller, A. Kagan, *Probing for new physics in polarized $\Lambda_b$ decays at the Z pole*, Phys. Rev. D 65 (2001) 074038.

[99] T. Mannel, S. Recksiegel, *Flavour changing neutral current decays of heavy baryons. The case $\Lambda_b \to \Lambda\gamma$*, Nucl. Part. Phys. 24 (1998) 979–990.

[100] T. Mannel, W. Roberts, Z. Ryza, *Baryons in the Heavy Quark Effective Theory*, Nucl. Phys. B 355 (1991) 38–53.

[101] S. Eidelman et al., *Review of Particle Physics*, Phys. Lett. B 592 (2004) 1.

[102] G. Hiller, private communication (2005).

[103] M. Jacob, G. Wick, *On the General Theory of Collisions for Particles with Spin*, Ann. Phys. 7 (1959) 404.

[104] J. Richman, *An experimenter's guide to the helicity formalism*, Unpublished CALT-68-1148.

[105] Y. Ueda, S.Okubo, *General theory of angular correlations of successively decaying particles*, Nucl. Phys. 49 (1963) 345.

[106] *Pythia web site*, `http://www.thep.lu.se/~torbjorn/Pythia.html`.

[107] *GEANT4 web site*, `http://wwwasd.web.cern.ch/wwwasd/geant4/geant4.html`.

[108] O. Deschamps et al., *Photon and neutral pion reconstruction*, LHCb COMP 03-091 (2003).

[109] C. Jacoby, P. Igo-Kemenes, *The new Efficiency algorithms*, LHCb COMP 04-080 (2004).

[110] G. Kostina, I. Belyaev, *Radiative $B$ decays with LHCb*, LHCb PHYS 03-090 (1997).

[111] L. Fernandez, P. Koppenburg, *Exclusive HLT Performance*, LHCb TRIG 05-047 (2005).

[112] E. Leader, *Spin in particle physics*, Cambridge University Press, Cambridge, UK, 2001.

[113] Z. Ajaltouni, E. Conte, O. Leitner, *$\Lambda_b$ decays into $\Lambda$ vector*, Phys. Lett. B 614 (2005) 165–173.

[114] J. Hrivnc, R. Lednicky, M. Smizanska, *Feasibility of Beauty Baryon Polarization Measurement in $\Lambda$ $J/\Psi$ decay channel by ATLAS-LHC*, J. Phys. G: Nucl. Part. Phys. 21 (1995) 629.

[115] Z. Ajaltouni, E. Conte, *Analysis of the channel $\Lambda_b \to \Lambda J/\Psi$*, LHCb PHYS 05-067 (2005).

[116] *The RooFit Toolkit for Data Modeling*, `http://roofit.sourceforge.net`.

# Curriculum Vitae

## Federica Legger


| | |
|---|---|
| Born: | November 16th, 1975 in Turin (Italy) |
| Living: | Av. De la Poste 18, 1020 Renens, Switzerland |
| Phone: | Home +41 21 6343984 |
| | Work +41 21 6930497 |
| Citizenship: | Italian |
| E-mail: | federica.legger@epfl.ch |


### Education

- **'Ph.D. in Physics'** at Ecole Polytechnique Federale de Lausanne (EPFL), Switzerland, in September 2006;
- **'Diploma (Laurea) in Physics'** at University of Turin, Italy, in July 2000, Full mark and honor;
- **'Diploma di maturità scientifica'** at 'Liceo Scientifico di Stato G. Segrè', in 1994, Full mark;
- **'High School Graduation'** at West Ouachita High School (LA, USA) ,in 1993.

### Additional courses

- **'Various Physics Post-graduate lectures (Troisieme Cycle de la Physique en Suisse Romande)'** at the EPFL (Switzerland) during Ph.D. studies 2001-2005:
- **'Second Physics Transalpin seminar – Astronomy and Cosmology'** in Dolomieu (France) in 2004;
- **'2002 European school of High-Energy Physics'** in Pylos (Greece) in 2002;
- **'TI DSP/BIOS 3.5 Days Design Workshop'** in Velizy (Paris) in 2002;
- **'TI DSP C6711 1 Day Workshop'** at the EPFL (Switzerland) in 2001;

### Working Experiences

- October 2001 - September 2006:
  I worked at **EPFL** (Ecole Polytecninque Federale de Lausanne) to prepare my Ph.d. thesis. I was involved in two projects:
  - Debugging, prototyping and code development for a readout board with DSP-FPGA mixed technology for the LHCb experiment at Cern.
  - Software development of L1 trigger algorithm for LHCb.
  - Physics analysis of polarized radiative $\Lambda_b$ decays at LHCb.

  During my stay, I also had teaching duties as an assistant with diploma students for several physics courses.
- October 2000 - September 2001:
  I worked at **CseIt – Telecom Italia Lab** (Telecom Research Center) as a researcher in It/Im division (Internet services and Multimedia). I was involved in two projects:
  - A portal for content sindycation, focused on the use of XML technologies, especially open-source projects such as Cocoon and Jetspeed.
  - Home networking appliances and services. In particular I developed an EPG to be used in a Video on Demand service.

  During my stay, I took classes in Networking, Signal analysis and processing and Information technology.
- May 1999 - July 2000:

I worked for **INFN** (National Institute for Nuclear Physics) on a particle physics experiment (**FNAL E835**) on charmonium spectroscopy, to prepare my diploma thesis;

- During 2000:
  I worked as Guest Scientist at **Fermilab National Accelerator Laboratory** (IL, USA), for E835 data taking.

## Languages

- **English** (fluent), **French** (fluent), **Italian** (mother tongue).

## Publications

- F. Legger, T. Schietinger, **'Photon helicity in $\Lambda_b \to pK\gamma$ decays',** hep-ph/0605245 (2006), submitted to Phys. Lett. B;
- F. Legger, T. Schietinger, **'The LHCb trigger and readout',** published in Proceedings of the 1st Hadron Collider Physics Symposium, Springer Proceedings in Physics, ISBN 3-540-32840-8 (2006);
- F. Legger et al., **'TELL1: development of a common readout board for LHCb',** VCI 2004 (Vienna Conference on Instrumentation) proceedings, published in NIM A 535 (2004) 497-499.

With others:

- G. Haefeli et al., **'TELL1: a common data acquisition board for LHCb'**, LECC 2003 (9th Workshop on Electronics for LHC Experiments) proceedings.

### LHCb notes:

- F. Legger, **'Reconstruction of the decays $\Lambda_b \to \Lambda(1115)\gamma$ and $\Lambda_b \to \Lambda(1670)\gamma$ at LHCb'**, LHCb Note 2006-012;
- F. Legger, T. Schietinger, **'Polarized radiative $\Lambda_b$ decays at LHCb'**, LHCb Note 2006-013;
- F. Legger, T. Schietinger, **'B-tracks in signal events rejected by the Level-1 Trigger'**, LHCb Note 2004-046;
- F. Legger et al., **'A L1 buffer implementation with DSP technology for LHCb readout board'**, LHCb Note 2003-109.

With others:

- G. Haefeli et al., **'TELL1: Specification for a common read-out board for LHCb'**, LHCb Note 2003-007.

## Conference participations

- **'Polarized radiative $\Lambda_b$ decays at LHCb'**, talk presented at the Swiss Physical Society meeting 2006 (February 2006, EPFL, Lausanne - Switzerland);
- **'The LHCb Trigger and Readout'**, poster presented at the Hadron Collider Physics symposium 2005 (July 2005, Les Diablerets - Switzerland);
- **'Design of the LHCb Silicon Tracker and the TELL1 Board'**, poster presented at Vienna Conference on Instrumentation 2004 (Wien - Austria).